The Pennsylvania State University

The Graduate School

College of Earth and Mineral Sciences

LASER DEPOSITION OF STAINLESS STEEL – TITANIUM CARBIDE COMPOSITES FOR REPAIR OF CRITICAL AEROSPACE COMPONENTS

A Thesis in

Materials Science and Engineering

by

Frederick Lia

© 2014 Frederick Lia

Submitted in Partial Fulfillment

of the Requirements

for the Degree of

Master of Science

August 2014

The thesis of Frederick Lia was reviewed and approved* by the following:

Richard P. Martukanitz
Senior Research Associate, Applied Research Laboratory
Thesis Co-Advisor

Gary L. Messing
Distinguished Professor of Ceramic Science and Engineering
Head of the Department of Materials Science and Engineering
Thesis Co-Advisor

Todd A. Palmer
Senior Research Associate, Applied Research Laboratory
Associate Professor of Materials Science and Engineering

Allison Beese
Assistant Professor of Materials Science and Engineering

Suzanne Mohney
Professor of Materials Science and Engineering
Chair, Intercollege Graduate Degree Program in Materials Science and Engineering

*Signatures are on file in the Graduate School.

ABSTRACT

This research project entailed the use of an experimental composite material for developing a laser deposition process that simulates carburized and chromium electroplated surfaces for bearing applications. Two gear component materials were chosen as substrates, carburized AISI 8620 steel (8620 steel) and Inconel 718® with a chromium electroplated surface. The experimental material included AISI stainless steel 431 (SS 431) as the matrix and titanium carbide (TiC) particle as the reinforcement material. The directed laser deposition process was used to deposit the composite material onto the substrate. Scanning electron microscopy (SEM), energy dispersive spectrometry (EDS), and a particle size analyzer were used to characterize selected powders used during the laser deposition experiment. Deposited materials were evaluated by microstructural analysis, Vickers micro hardness testing, and EDS-mapping for examining the dissolution reaction of the reinforcement particles within the SS 431 matrix. Performance testing of the laser deposited composite material was also conducted and included rolling contact fatigue testing and tribological analysis. Vickers hardness testing indicated that the hardness of the SS 431/20 wt% TiC deposited on the 8620 steel matched the hardness of the carburized 8620 steel. Micro hardness of the deposited materials was found to be 750 in the Vickers scale. SEM images showed that some of the TiC particles dissolved and the Ti and C were reprecipitated in the SS 431 matrix. The higher carbon within the matrix material enhanced the overall hardness of the laser deposit. Chemical analysis by EDS further supported this finding. The TiC particles were dissolved into small unstable dendrite around the surface of the TiC particle. The dissolved TiC phase that surrounded the original TiC particle formed a secondary phase in the matrix alloy by reprecipitation during cooling. Rolling contact fatigue tests indicated that the composite deposit exhibited slightly greater wear, due to hard particle expulsion, that resulted in lower rolling contact fatigue life when compared to the 8620 steel that had been carburized. The SS 431 – TiC composites were also attempted to replace the chromium electroplated surface on Inconel 718® substrate. However, the deposited composite materials were diluted by Inconel 718® substrate and significantly reduced the hardness of deposited materials which did not meet the requirement.

TABLE OF CONTENTS

LIST OF FIGURES vi

LIST OF TABLES x

ACKNOWLEDGEMENTS xi

Chapter 1. INTRODUCTION 1

1.1 Statement of the Problem 1

1.2 Research Plans 2

Chapter 2. LITERATURE REVIEW 4

2.1 Additive manufacturing and laser deposition. 4

2.2 Laser deposition with metal alloys, ceramics, or composite materials. 8

2.3 Recent research on the AISI 431 (SS 431) – TiC composite system 11

2.4 Target properties after deposition 15

Chapter 3. PROCEDURE AND CHARACTERIZATION 17

3.1 Powder characterization 17

3.1.1 SEM (ESEM) 17

3.1.2 EDS 17

3.1.3 Particle size analyzer 17

3.2 Material preparation and selection 17

3.3 Process development 18

3.4 Production of test dpecimens 20

3.5 Specimen characterization 24

3.5.1 Microstructural analysis 24

3.5.2 Vickers hardness test 25

3.5.3 EDS – mapping analysis 26

3.5.4 Rolling contact fatigue test 27

3.5.5 Tribology analysis 30

Chapter 4. CHARACTERIZATION RESULTS AND DISCUSSION 31

4.1 Materials characterization results 31

4.1.1 AISI 8620 steel 31

4.1.2 AISI stainless steel 431 32

4.1.3 Titanium carbide 36

4.1.4 Inconel 718® 40

4.2 Characterization of laser deposited materials 44

4.2.1 Microstructural analysis 44
4.2.1.1 Process development specimens 44
4.2.1.2 Test specimens 48
4.2.2 Vickers hardness test 56
4.2.2.1 Process development specimens 56
4.2.2.2 Test specimens 59
4.2.3 EDS – mapping analysis of laser deposited SS 431/20 TiC specimen 62
4.2.4 Rolling contact fatigue test 68
4.2.5 Tribology analysis 79

Chapter 5. CONCLUSIONS 91
REFERENCES 93
APPENDIX A – Laser deposition process parameters 96
APPENDIX B – Hardness conversion chart 98
APPENDIX C – Vickers hardness results 100
APPENDIX D – Optical profilometry data 107

LIST OF FIGURES

Figure 1 – Schematic of the machine for the powder bed fusion process. 5
Figure 2 – Schematic of powder bed fusion process. 6
Figure 3 – Schematic of directed laser deposition process. 7
Figure 4 – Schematic of the laser deposition technique. 7
Figure 5 – Enthalpy of formation, ΔH_f, of various hard phases. 13
Figure 6 – Dissolution of WC particle in iron and nickel. 13
Figure 7 – Thermodynamic stability diagram and solid volume fraction during cooling for a system represented by titanium or tungsten with carbon in SS 431. 14
Figure 8 – Thermodynamic calculations of MX stability as a function of carbon and nitrogen for a simple Fe-based and complex Fe-base alloy. 14
Figure 9 – Two-phase molar Gibbs energy diagram. 15
Figure 10 – Single track deposit of SS 431 at 1.0 cm^3/min powder flow rate and 2 kW laser power. 20
Figure 11 – Schematics of the specimen produced for RCF testing. 22
Figure 12 – Carburized 8620 steel specimen that had been laser deposited with SS 431/20 TiC. 22
Figure 13 – The final dimensions of the RCF test specimen. 23
Figure 14 – The RCF test specimen with laser deposited SS 431/20% TiC. 23
Figure 15 – Inconel power shaft showing laser deposition with selected materials. 24
Figure 16 – Laser deposited materials on Inconel 718® power shaft after roller grind machining. 24
Figure 17 – Demonstrating the staggered procedure for measuring micro hardness. 26
Figure 18 – Schematic of the rolling contact fatigue test. 27
Figure 19 – Photograph of the rolling contact fatigue test at the Drivetrain Technology Center of the Applied Research Laboratory 28
Figure 20 – SEM image of SS 431 particles of powder. 33
Figure 21 – SEM image of SS 431 particle with satellites around the dense spherical particle of powder. 34
Figure 22 – Particle size distribution of SS 431 powder. 35
Figure 23 – Results of EDS spectrum of SS 431 powder. 35

Figure 24 – SEM image of TiC particles of powder. 37
Figure 25 – SEM image of TiC particle with pores at the surface of powder. 38
Figure 26 – Particle size distribution of TiC powder. 39
Figure 27 – Results of EDS spectrum of TiC powder. 39
Figure 28 – SEM image of Inconel 718® spherical particles of powder. 41
Figure 29 – SEM image of dense spherical Inconel 718® particle of powder. 42
Figure 30 – Particle size distribution of Inconel 718® powder. 43
Figure 31 – EDS spectrum of Inconel 718® powder. 43
Figure 32 – Microstructural images of laser deposited SS 431 between single layer and multi-layers. 45
Figure 33 – Microstructural images of laser deposited SS 431/20% TiC between single layer and multi-layers. 45
Figure 34 – Microstructural images of laser deposited SS 431/40% TiC between single layer and multi-layers. 46
Figure 35 – Microstructural images of laser deposited SS 431/60% TiC between single layer and multi-layers. 46
Figure 36 – Microstructural cross-section of each sample. 47
Figure 37 – Boundary lines which appeared in each deposition sample. 48
Figure 38 – Microstructural images of RCF test specimen with laser deposited SS 431/20 wt% TiC representing transverse cross-section. 49
Figure 39 – Microstructural images of RCF test specimen with laser deposited SS 431/20 wt% TiC representing longitudinal cross-section. 50
Figure 40 – Microstructural images of Inconel 718® shaft. 51
Figure 41 – Microstructural images of Inconel 718® deposited on Inconel 718® shaft. 52
Figure 42 – Microstructural images of SS 431 deposited on Inconel 718® shaft. 53
Figure 43 – Microstructural images of SS 431/20 TiC deposited on Inconel 718® shaft. 54
Figure 44 – Microstructural images of SS 431/40 TiC deposited on Inconel 718® shaft. 55
Figure 45 – Microstructural images of Inconel 718® shaft with chrome electroplated surface. .. 56
Figure 46 – Hardness of deposits produced using increasing amount of TiC blended in SS 431 powder that had been deposited on low carbon steel. 57

Figure 47 – Hardness profile with four different mixtures of SS 431 and TiC on carburized 8620 steel. 58
Figure 48 – Hardness profile of SS 431/20 TiC laser deposited on 8620 carburized steel of transverse and longitudinal cross-sections. 60
Figure 49 – Hardness results of Inconel 718® shaft with deposited materials. 61
Figure 50 – SEM image of normalized 8620 steel used for substrate. 63
Figure 51 – SEM image of HAZ of substrate used for laser deposition experiment. 63
Figure 52 – SEM image of SS 431/20 TiC laser deposited material. 63
Figure 53 – Images generated by EDS mapping analyzer. Showing elements located from Figure 52. 64
Figure 54 – SEM image showing TiC particles along with precipitation of Ti C formed during cooling. 66
Figure 55 – SEM image showing Ti C precipitation. 67
Figure 56 – Scuffed surface on the SS 431/20 TiC after RCF testing. 71
Figure 57 – RCF test results showing scuffing surface on the carburized 8620 steel roller. 72
Figure 58 – RCF test results showing surface pitting on the SS 431/20 TiC specimen. 73
Figure 59 – Weibull plot of rolling contact fatigue life time for the carburized 8620 steel and laser deposited SS 431/20 TiC 74
Figure 60 – RCF testing results of the carburized 8620 steel specimen without scuffing surface. 75
Figure 61 – Tribology analysis results of carburized 8620 steel roller before RCF testing. 76
Figure 62 – Tribology analysis results of carburized 8620 steel roller after RCF testing. 77
Figure 63 – Tribology analysis results of SS 431/20 TiC deposit material after RCF testing. 78
Figure 64 – Optical profilometry results of the the baseline carburized 8620 steel specimen used in the RCF test. 81
Figure 65 – Optical profilometry results of the SS 431/20 TiC RCF test specimen at the surface without defects. 82
Figure 66 – Optical profilometry results of the SS 431/20 TiC RCF test specimen at the surface with defects. 83
Figure 67 – Microstructural image showing voids on the surface of RCF specimen. 84
Figure 68 – SEM image of voids on the surface of RCF specimen. 85

Figure 69 – Optical profilometry of Inconel 718® shaft. 86
Figure 70 – Optical profilometry of Inconel 718® deposited onto Inconel 718® shaft. 87
Figure 71 – Optical profilometry of SS 431 deposited onto Inconel 718® shaft. 88
Figure 72 – Optical profilometry of SS 431/20 TiC deposited onto Inconel 718® shaft. 89
Figure 73 – Optical profilometry of SS 431/40 TiC deposited onto Inconel 718® shaft. 90

LIST OF TABLES

Table 1 – Additive manufacturing process parameters and results with various materials. 10
Table 2 – Carburized 8620 steel RCF testing results. 16
Table 3 – Rolling Contact Fatigue Testing condition details. 29
Table 4 – Chemical composition of 8620 steel alloy. 31
Table 5 – Properties of interest for 8620 steel alloy. 31
Table 6 – Measured and reported nominal chemical compositions for SS 431 powder. 36
Table 7 – Properties of interest for SS 431. 36
Table 8 – Measured and reported nominal chemical compositions for TiC powder. 40
Table 9 – Properties of interest for TiC. 40
Table 10 – Measured and reported nominal chemical compositions for Inconel 718® powder. .. 42
Table 11 – Properties of interest for Inconel 718®. 42
Table 12 – Vickers hardness of SS 431 and SS 431/TiC composite for single layer and multi-layer depositions. 57
Table 13 – Surface hardness of carburized 8620 steel and two selected deposition materials. 58
Table 14 – Micro hardness for SS 431/20 TiC deposit, HAZ, and substrate for the transverse and longitudinal cross-sections. 60
Table 15 – Micro hardness of Inconel 718® shaft with deposition materials. 61
Table 16 – EDS elemental analysis results of each region of the RCF testing specimen. 65
Table 17 – Results of SS 431/20 TiC RCF testing compared with reference carburized 8620 steel. 70
Table 18 – Surface roughness of RCF test specimens. 80
Table 19 – Surface roughness of baseline material and laser deposited materials for power shaft. 85

ACKNOWLEDGEMENTS

I would first like to thank my advisors: Dr. Richard Martukanitz and Dr. Gary Messing. They brought different perspectives and areas of expertise to the project, enabling me to have gained a broader perspective during my research. This thesis would not be possible without their advice and assistance.

I would also like to thank the staff of the Laser Processing Division of the Applied Research Laboratory: Jay Tressler and Ed Good. Because of their help, I was able to efficiently complete the experimental portion of the project. They also guided me through sample preparation for metallography.

A very special thanks to Aaron Isaacson, who not only operated the optical profilometer, but also coordinated rolling contact fatigue testing at the Gear Research Institution. Because of his assistance, we were able to complete this part of project on time.

Chapter 1. INTRODUCTION

1.1 **Statement of the Problems**

Carburized steel such as Alloy AISI 9310 (AMS 6265) and Alloy AISI 8620 (AMS 6274) is utilized as the standard material for many gear applications within the aerospace and automotive industry, many times in the case hardened condition. This steel is used because of its toughness and ability to be easily carburized, thus providing an exceptionally hard surface for wear resistance while retaining high damage resistance at the surface. However, the carburization process may result in distortion, which leads to a higher overall cost due to post-machining required to meet final dimensions. [1]

Additive Manufacturing (AM), Rapid Prototyping (RP) or 3-D printing have been developed since the 1980s, with printers becoming widely available commercially in recent years. With the rapid growth of laser processes and the reduced cost of laser systems, laser deposition technology is proposed as an alternate process for achieving high surface hardness for repairing high value components. The laser-based directed energy deposition (DED) process has been given specific attention because the process offers several advantageous features. [1] Laser deposition technology involves melting powder that is added as a thin solidified layer on the surface. [2] The process may be applicable to achieve high surface hardness and wear resistance on the surface of new parts, as well as for repairing case hardened components that have been worn beyond acceptable usage. This thesis describes initial evaluations in developing a laser deposition process and a material for application to aerospace components requiring high surface hardness, such as case hardened and chromium electroplated parts.

AM technology and the laser deposition process are well developed. The technology is being considered for rapid prototyping and repair of high value components. However, the materials and processes for evaluating the characteristics of a carburized or electroplated surface have not been defined.

1.2 **Research Plans**

Earlier research [3] had been conducted with metal matrix composite materials, representing metal alloys and carbides, for advanced wear and corrosion resistant using the laser deposition process. The metal matrix composite systems entailing TiC added to a ferrous matrix were investigated using computational thermodynamics and kinetic analyses, and composite materials were evaluated using the laser deposition process. The research showed an increase in hardness with higher amount of carbides in the composite systems. The results also indicated that a portion of the hardness increase was due to the formation of a metal carbon-nitride, M[CN], phase that formed during cooling. To achieve high level of the M[CN] phase, nitrogen gas was also utilized for shielding as a reactive gas. Recent research [4] also indicates that hardness increases, by adding TiC decreased ductility in the deposited material.

Two drivetrain component materials were chosen as substrates, carburized AISI 8620 steel (8620 steel) and Inconel 718® with a chromium electroplated surface. Carburized steel alloys have been heavily used in the automotive and aerospace industries, because the high surface hardness and wear resistance after carburization. Inconel 718®, a nickel based super alloy, is also used throughout the aerospace industry, as turbine blades and other critical engine and drivetrain components. The experimental composite materials selected for evaluation in this work were based on prior research by S.S. Babu, R. P. Martukanitz, and F Lia [3,4]. The selected powder materials for evaluation were stainless steel AISI 431 (SS 431) and titanium carbide (TiC), blends representing the SS 431 and TiC, and Inconel 718®. The selected powder materials were laser deposited on 8620 steel and Inconel 718® substrates, and evaluated based on microstructural analysis, micro hardness testing, and energy dispersive spectroscopy (EDS). The deposits created using these materials were required to be defect free and provide hardness and wear resistance comparable to the carburized 8620 steel or chromium electroplated Inconel 718® surface.

Based on the initial evaluations, final selection of a candidate material was performed, and performance evaluations were conducted using the selected material deposited onto carburized 8620 steel for rolling contact fatigue (RCF) testing and tribological analysis. Results of the RCF test representing the composite deposit were compared to earlier results of carburized

8620 material. Tribological analysis was used to determine if the repair deposits would meet surface finish requirements for service.

Chapter 2. LITERATURE REVIEW

2.1 Additive manufacture and laser deposition

Additive manufacturing (AM) or 3D printing is a process of adding features or building a complete component in layers by depositing material to virtually any shape from a digital model. AM involves a number of steps that move from the virtual CAD description to the resultant part. [2] In general, AM processes involve CAD design, conversion of the drawing design to a file format which can be accepted by AM machines, development of process parameters for AM machines, building of the actual part from design by AM machines, and post processing to meet the final geometry for the design. There are two typical processes used for additive manufacturing of metallic materials: directed energy deposition and powder bed fusion processes. The directed energy deposition process is used to add material for repair or refurbishment, and the powder bed fusion process is used exclusively to build components.

The powder bed fusion process commonly lays down a thin layer of powder or slurry materials, with layer thickness between 50 to 150 μm. The layer materials are spread across the build area by a scraping blade or a leveling roller. The machine then utilizes a laser or electron beam to melt and resolidify the powder layer designated by the CAD program. The machine will then lay down a new layer of materials on top of the previous layer, and repeat the process until the part has been built. Figures 1 and 2 demonstrate the powder bed fusion process. The building process usually takes place inside an enclosed chamber filled with inert gas, such as nitrogen (N_2), argon (Ar), or a vacuum, to minimize oxidation and degradation of the material. [2,5,6]

The directed energy deposition process involves injection of powder or a consumable wire into a laser or electron beam, respectively. The beam and added material is moved relative to the build plate to sequentially produce layers that result in the three-dimensional part. [2,5,6] During the process, the laser or electron beam creates a melt pool on the surface of the substrate and simultaneously adds material into the melt pool. Partial overlapping of individual tracks in a suitable pattern produces a continuous layer of material. With alternative stacks of layers above the previous deposition layer, three dimensional objects are generated. [7] Schematics of the directed energy process using a laser beam and powder are

shown in Figures 3 and 4. The building process also takes place inside an inert gas environment when a laser is employed and a vacuum when an electron beam is utilized.

When AM features are applied to repair a surface, it is usually referred to as laser deposition. As a subset of the DED process, laser deposition involves the fusing of a material onto a substrate using the laser as the heat source to provide full metallurgical bonding between the two materials. Powder material is utilized as the deposition material, which is used to coat the base metal or substrate. For repair applications the substrate is the existing part onto which an additional geometry or surface will be added. [5] The main advantage of laser deposition over traditional methods is the ability to apply a coating to a localized area with good fusion, limited heat distortion, and small heat affected zone (HAZ). The deposit provides improved surface properties, such as wear resistance, corrosion resistance, electrical conductivity, or thermal conductivity. Laser deposition technology for repair of worn or damaged materials is used in the aerospace, biomedical, auto-motive, and defense industries. [4]

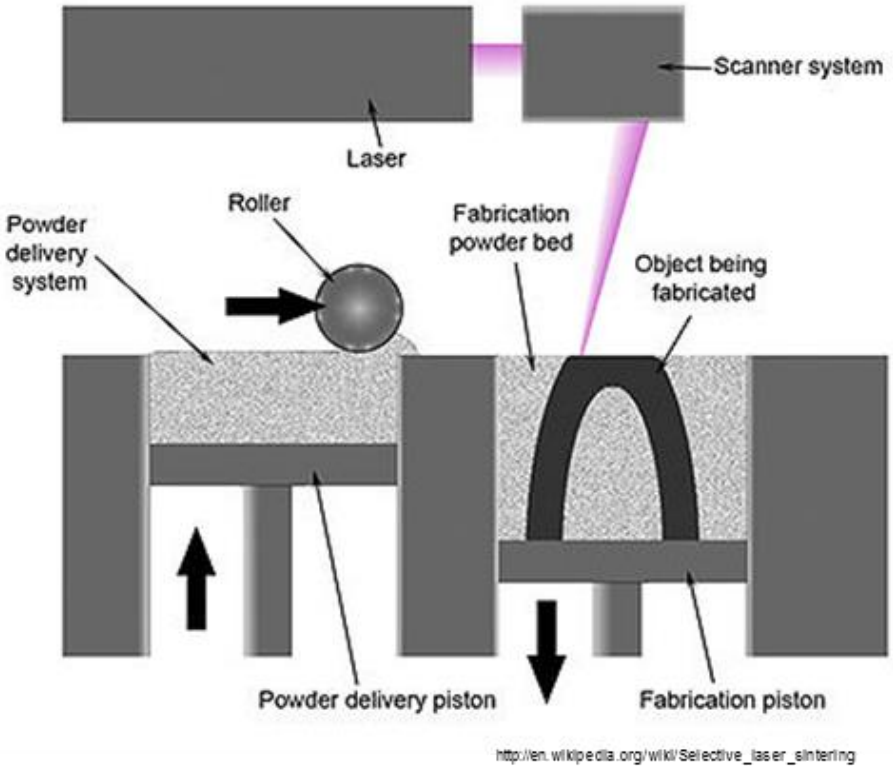

Figure 1 – Schematic of the machine for the powder bed fusion process.

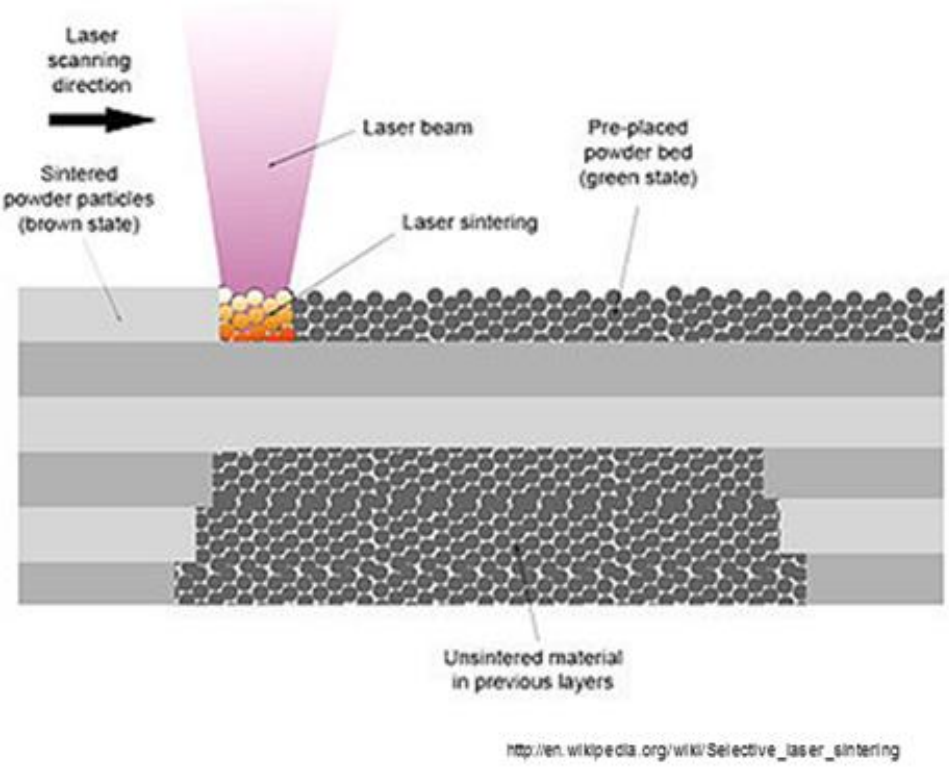

Figure 2 – Schematic of powder bed fusion process.

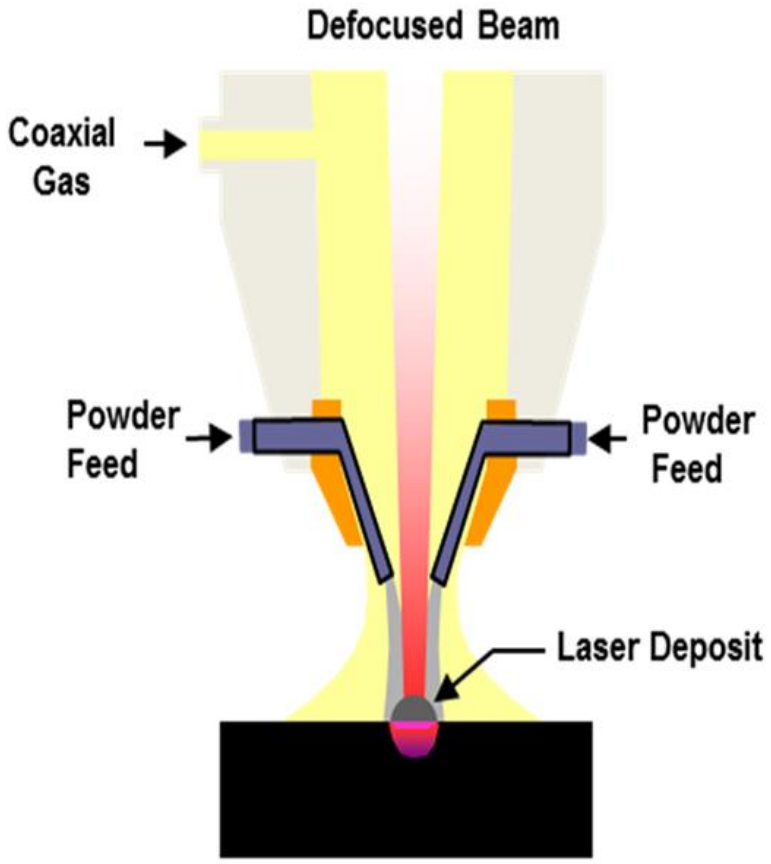

Figure 3 – Schematic of directed laser deposition process.

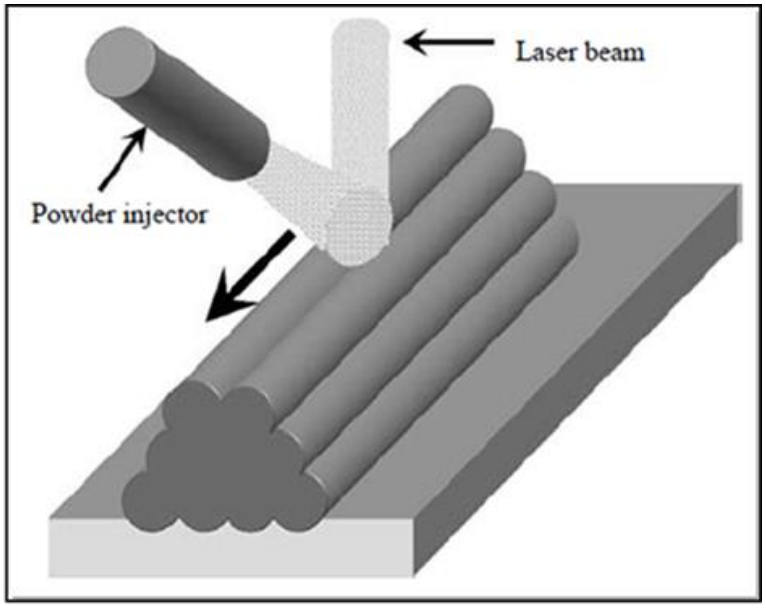

Figure 4 – Schematic the laser deposition technique. [7]

2.2 **Laser deposition with metal alloys, ceramics, or composite materials.**

Directed laser deposition has been used for depositing a wide-range of materials and alloys. A series of Inconel 625 samples were successfully fabricated by the laser deposition process without defects, cracks, bonding error or porosity. [8] The hardness of the deposit was higher than the annealed material due to the very fine microstructure and a higher degree of supersaturation of strengthening elements. The results revealed that directionally solidified components could be prepared or repaired by DMD when an appropriate processing strategy was followed, which specified that the laser scanning direction should be identical for the deposition of all layers. Laser deposition was also found to be an alternative technique for the fabrication of Inconel 625 components with an advantage in improved mechanical strength without sacrificing ductility. [9] The higher hardness achieved by the laser deposition was due to a rapid cooling rate during processing.

Utilizing the laser deposition process, metal matrix composite material may be deposited. A recent research paper reported the use of Inconel 625 powder forming the matrix, mixed with varying amounts of TiC powder or Ni-coated TiC powder as the reinforcement. [10] The process parameters were 280 W laser power, 14.8 mm/s (~ 35 in/min), and 10 RPM for the powder feed rate setting. The TiC particles were uniformly distributed in the Inconel 625 matrix, and the microstructure was defect free. Part of the Ni coating on the TiC particle surface was remelted and dissolved into the Inconel 625, which most of the Ni coating and others remained on TiC particles. Mechanical testing showed the Inconel 625 with Ni-coated TiC deposits had higher strength than Inconel 625 with TiC.

Another research group used 65 wt% of SS 316L powder and 35 wt% of silica (SiO_2) sol as a ceramic-matrix sol-gel process. [11] The sample was processed with a laser power of 25 to 45 W, 80 to 180 mm/s scan speed, and layer thickness of 50-150 μm. The results showed higher laser power provided higher bending strength and a lower percentage of porosity. Slower scan speed and smaller hatch spacing also increased bending strength. However, the process could result in bonding failure between SS 316L and silica sol. The research also recommended that the laser energy density should be below 0.4 J/mm^2 to prevent bond degradation and reduced strength. However, an energy density lower than 0.1 J/mm^2 would not be sufficient to gel the silica sol. The final sample required post heat treatment at 800 °C for 1 hour.

Table 1 is an evaluation of additive manufacturing using metal matrix and ceramic matrix composite materials. Several other researches on ceramics or composite materials have also been performed using AM processes, and a list of process, parameters, results, and issues are shown in Table 1.[12-18] The primary issue of processing ceramics or composite materials with AM processes is the final density (relative density) of the part. Table 1 shows that most of ceramics or composite parts only reach 95% of relative density, unlike metals or metal matrix composites that usually have fully dense structures due to the relatively lower melting point and higher thermal expansion coefficient. The other issue with processing ceramics and composite materials relates to the post heat treatment step. Post heat treatment process not only sacrifices the total production time of each sample, but also affects the microstructure of the sample and mechanical properties.

Table 1 – Additive manufacturing process parameters and results with various materials.

Materials	Sintering / Melting	Feed Stock	Processing Condition	Relative Density (%)	Microstructures	Issues
99.9% Al_2O_3 [12]	Sintering	LENS MR-7, powder injection	175 W, 10mm/s, 14g/min	94	Dense and crack-free with 6.6±2 µm grain size as-fabricated. 207±90 µm grain size after heat treated.	Al_2O_3 decomposed during processing, require post heat-treatment to 1600 °C for 5 h to reach 98% density and reform Al_2O_3
68 vol% Al_2O_3 and 32 vol% ZrO_2 [13]	Melting	Powder bed	60 W, 200mm/s,	94	Fine grain, nano-sized microstructure. 50 µm coarser crystals formed between layers.	Used another CO_2 laser to pre-heat powder up to eutectic T. (1860 °C)
58 vol% Al_2O_3, 14vol% ZrO_2, 3 vol% TiC, 12 vol% wax, and 13 vol% PMMA [14]	Sintering	Powder bed	14 W, 1400 mm/s, 0.15 mm powder depth, 50 °C pre-heat	95	Uniform dense microstructure, 24 µm particle size after 1 hour sintering time.	Post heat treatment to 300 °C at 100 °C /h for 1h, then heated to 450 °C at 100 °C/h for 2h, and finally heated to 1500 °C at 100°C /h 60 min before cooling at 30 °C /h.
4:1 ratio of YSZ (ZrO_2 90 wt.%, Y_2O_3 10 wt.%) and Al_2O_3 [15]	Sintering / Melting	Phenix Systems PM 100, Powder bed	2-30 W, 2-60 mm/s, Processed both in air and Ar	NA	Smooth uniform, but contained pores and cracks.	Sample cracked when laser power greater than 16 W and processed in air. Formed intermetallic Al_3Zr, caused by decomposition of ZrO_2
SiO_2 [16]	Sintering	Powder bed	45 W, 0.23 mm/s in y-axis, 40 Hz oscillation in x-axis	NA	Laser-irradiated surface of the part reveals a dense glassy structure while the opposite side wasn't completely dense.	A 120 µm diameter laser spot is scanned with about 10 mm/s over the porous surface of the SiO_2 body, to reach a dense structure.
Si/SiC [17]	Sintering	EOS M160, Powder bed	45-52 W, 200-300 mm/s	45-52	Distinct laminated structure with an open porosity of about 0.5%.	High oxygen content on top of each layer (SiO_2).
Porcelain, PM905 [18]	sintering	Powder bed	50 W, 85 mm/s, 0.6 mm hatch spacing	NA	Microstructures are compacted, but had pores even after post heat treatment.	Post heat treatment between 1425-1475 °C. Final sample contained mullite, quartz, and glass matrix. Residual thermal stress caused the delamination between adjacent layers and cracks in the sintering surface.
65 wt.% SS 316L powder, and 35 wt.% silica sol [11]	gelation	Powder bed, similar to ExOne system	35 W, 150 mm/s, 0.1mm layer thickness	NA	No microstructure result, but porosity among the built layers	Porosity. Post-heat treatment at 800 °C for 1 hour. Sample has 45 MPa strength, but its depending laser energy density, 0.4 J/mm2. Higher energy cause degradation of the silica gelled, lower energy won't gel the silica sol.
Inconel 625 mix with TiC or TiC/Ni 11 vol% TiC/Ni 22 vol% TiC/Ni 22 vol% TiC [10]	sintering	LENS	280 W, 14.8 mm/s, 10 RPM (powder feed rate)	NA	A portion of the Ni coating still remained on TiC particles, others remelting and dissolved into the Inconel 625	

2.3 **Recent research on the AISI 431 (SS 431) – TiC composite system**

R.P. Martukanitz and S.S. Babu [3] suggested that the stability of the hard reinforcement phase during the rapid heating and cooling cycle experienced in the laser deposition process is critical in developing affordable coatings having improved wear resistance, because dissolution of the reinforcement particles result in the loss of their ability to improved wear resistance. Carbide materials also create brittle microstructures that increase the sensitivity of the matrix to cracking upon cooling. The solubility of the particle may be estimated by its enthalpy of formation, ΔH_f. In general, lower values of ΔH_f denote decreased solubility of the particle and greater stability. The enthalpy of formation for various carbides, nitrides, and borides is shown in Figure 5. [3]

Microstructural observations shown in Figure 6, also indicate that dissolution of tungsten carbide particles in iron-rich liquids was faster than that in nickel-rich liquids for identical laser traversing speeds. [3] The dissolution of tungsten carbide particles in iron-rich liquid became less pronounced with an increase in laser traversing speed. Tungsten carbide particles developed complex, faceted surfaces in the nickel-rich structure.

Figure 7(a) shows the thermodynamic stability diagram at 1600 °C, and Figure 7(b) shows the solid volume fraction during cooling for a system represented by titanium or tungsten with carbon in stainless steel alloy 431. The greater stability, based on composition, was associated with TiC in the stainless steel alloy 431 when compared to WC and may be seen in the figure by the larger region showing TiC stability.

The stability diagram for the Fe-Ti-C-N system at 1800 K is shown in Figure 8. The calculations considered different extents of dissolved nitrogen as a function of titanium and carbon concentrations in the liquid iron. Since the TiC, TiN and Ti(CN) all have face centered cubic (FCC) crystal structure, in thermodynamic calculations the three phases are denoted as MX. The first set of calculations was performed in a simple Fe-C-T-N system with no dissolved nitrogen. The calculations showed a limited stability of the MX phase as shown by the shaded region. However, with an increase in nitrogen concentration to 0.003 wt%, the calculations showed increased stability of MX phase indicating that the MX phase is progressively changing from TiC to Ti(CN). At high concentrations of nitrogen, the

calculations showed that the MX phase is stable even with low-carbon concentrations. This showed that by the combined additions of titanium, carbon and nitrogen, the MX particles could be stabilized in the Fe-rich laser melt pool.

The stability of a phase is governed by its free energy, which can be described as Equation 1. The free energy contribution(G^{ϕ}) equals the pure components in that phase(G_o^{ϕ}) plus the contribution from ideal mixing($G_{idea-mix}^{\phi}$) plus the contribution due to non-ideal interactions between the components($G_{excess-mix}^{\phi}$). Equation 1 can be substituted by the chemical potential of element, μ_i^{ϕ} to obtain Equation 2.

$$\mathrm{G}^{\Phi} = \mathrm{G}_{\mathrm{o}}^{\Phi} + \mathrm{G}_{\mathrm{ideal+mix}}^{\Phi} + \mathrm{G}_{\mathrm{excess-mix}}^{\Phi} \qquad \text{Eq. (1)}$$

$$\mu_{\mathrm{A}}^{\Phi} = \mathrm{G}^{\Phi} - \mathrm{X}_{\mathrm{B}}^{\Phi} \frac{\partial \mathrm{G}^{\Phi}}{\partial \mathrm{X}_{\mathrm{B}}^{\Phi}}; \mu_{\mathrm{B}}^{\Phi} = \mathrm{G}^{\Phi} - (1 - \mathrm{X}_{\mathrm{B}}^{\Phi}) \frac{\partial \mathrm{G}^{\Phi}}{\partial \mathrm{X}_{\mathrm{B}}^{\Phi}} \qquad \text{Eq. (2)}$$

A two-phase Gibbs energy diagram is shown in Figure 9. The Gibbs energy diagram indicates that some mixture of α+β is the stable state for an alloy between the two tangent points. [19] The lower enthalpy governs lower free energy and chemical potential, which means the material with lower enthalpy in Figure 5 has a greater stability in the matrix.

The results of the research showed carbides in the form of TiC dendrites and also fine titanium carbonitrides, Ti(CN), formed within the SS 431 matrix. [3] The dissolved titanium, carbon and nitrogen reacted to precipitate as TiC and Ti(CN). The presence of the dendritic shaped TiC particles indicate these precipitates were forming before the primary solidification of the SS 431 matrix. The research also reported that the laser deposits of the SS 431 with the addition of TiC powder significantly increased the surface hardness of laser deposits.

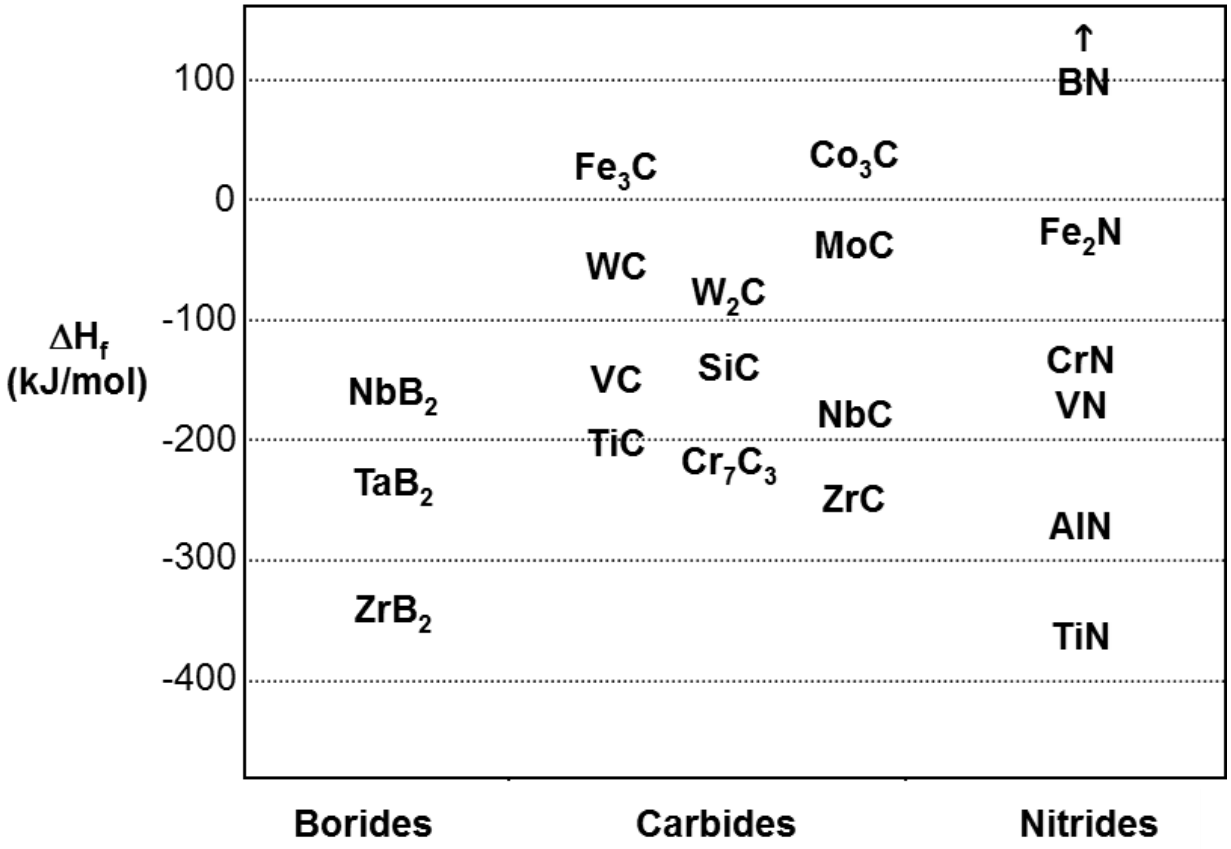

Figure 5 – Enthalpy of formation, ΔH_f, of various hard phases. [3]

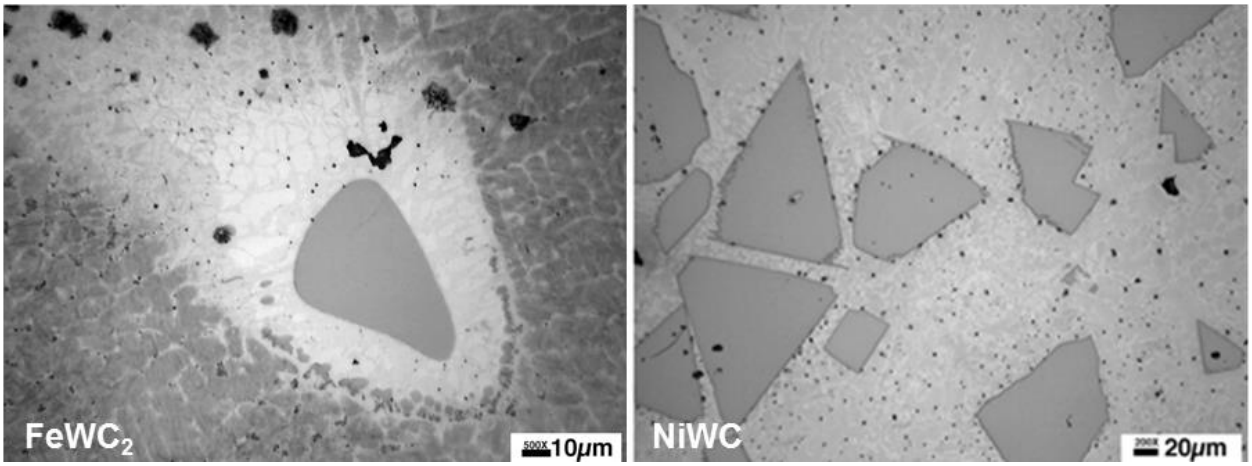

Figure 6 – Dissolution of WC particle in iron (left) and nickel (right). [3]

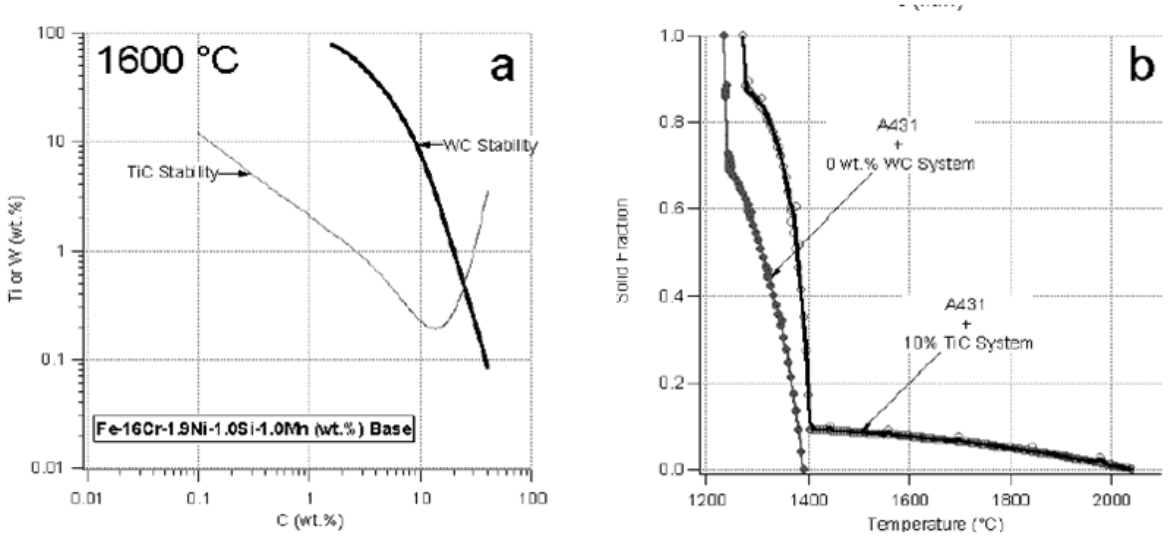

Figure 7 – Thermodynamic stability diagram (a) and solid volume fraction during cooling (b) for a system represented by titanium or tungsten with carbon in SS 431. [3]

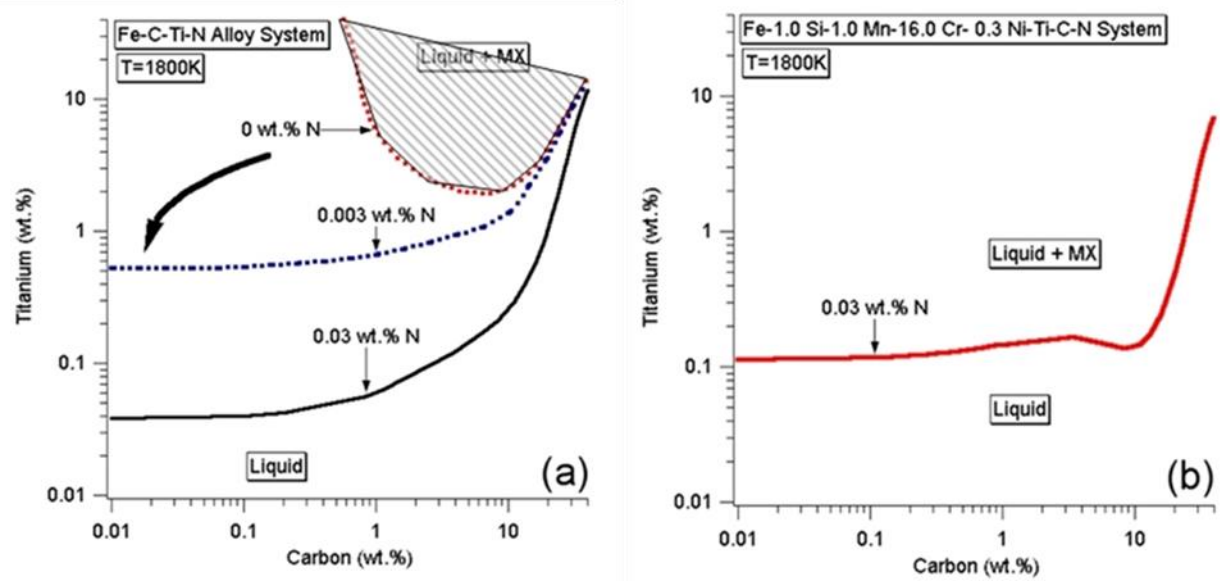

Figure 8 – Thermodynamic calculations of MX stability as a function of carbon and nitrogen for (a) a simple Fe-based and (b) complex Fe-base alloy. [3]

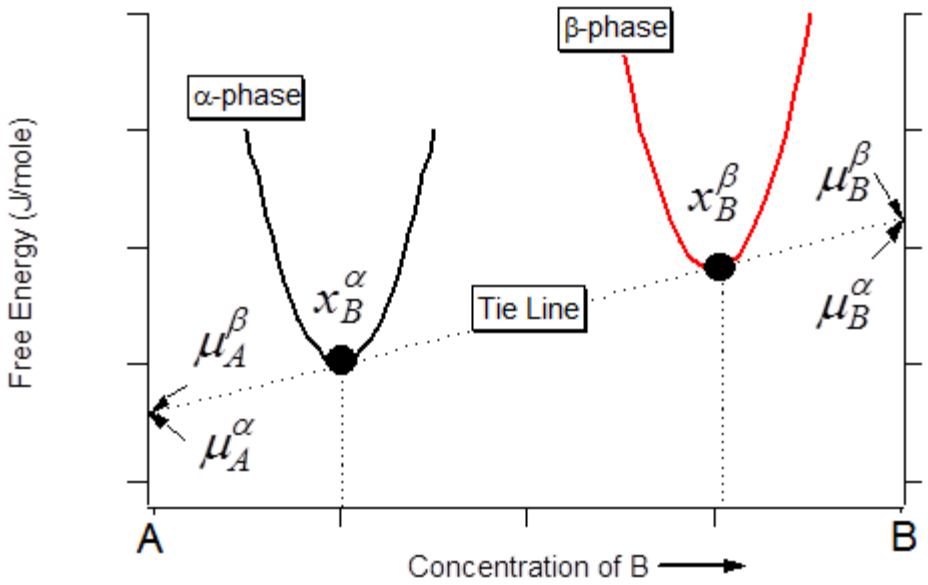

Figure 9 – Two-phase molar Gibbs energy diagram. [3]

2.4 **Target Properties after Deposition**

The results of the investigation should provide deposition properties that are comparable to gear components produced from AISI 8620 steel (8620 steel) that have been carburized and chromium electroplated Inconel 718®. The conclusion of this research should be based on two considerations: the hardness of the experimental deposits must be equal or higher than the carburized 8620 steel surface and the chromium electroplated Inconel 718®, and the results of rolling contact fatigue (RCF) testing of the laser deposited material on carburized 8620 steel should be equivalent to an 8620 carburized surface. The carburized 8620 steel surface is reported to have a hardness of between 700 and 750 Vickers hardness (HV). [20] Because of the wide range of hardness reported for chromium electroplated surfaces, hardness of the chromium electroplating on the Inconel 718® surface would be measured during this research. The RCF testing of laser deposit material on carburized 8620 steel will be directly compared with prior RCF test results of carburized 8620 steel. The RCF test simulates the rolling/sliding action that occurs in a gear mesh, the testing results typically determine the surface durability performance of the material by comparing the lives to failure of the tested specimens. [21] The

occurrence of wear in an RCF test is not typical, but can be used to compare the wear resistance of a material by measuring the wear rate or total time to a maximum wear interval of the test specimen. The prior RCF test results of carburized 8620 steel would be provided by the Drivetrain Technology Center at the Applied Research Laboratory. These prior results are shown in Table 2. [22]

Additionally, the finished specimens require a surface finish finer than Ra equal to 1.63 µm (64 µin) after grinding and preferably an Ra equal to 0.406 – 0.813 µm (16 – 32 µin). When the surface roughness of the bearing surface is greater than Ra equal to 64 µin, the component is considered non-serviceable. The ability of the deposited material to meet these tribology requirements after grinding is an important consideration for bearing surfaces under rotation.

Table 2 – Carburized 8620 steel RCF testing results.

Specimen #	Roller #	Stress (ksi)	Load (lbs)	Speed (rpm)	Hours	Cycles (x 10^6)	Specimen Ra (µin)	Roller Ra (µin)	Observations
341-1	341-30	300	1249	2922	135.4	23.738	30.25	3.3	Surface Origin Pitting
341-37	341-33	300	1249	2922	188.1	32.978	27.5	4	Surface Origin Pitting
341-33	341-36	300	1249	2919	84.2	14.747	26.5	13	Surface Origin Pitting
341-55	341-44	300	1249	2925	207.9	36.486	35.75	14.25	Surface Origin Pitting

Conditions		
	Speed	3000 rpm, High
	Temperature	70 °C (158 °F), Low
	Ra	High
	Sliding	High

Chapter 3. PROCEDURE AND CHARACTERIZATION

3.1 **Powder characterization**

3.1.1 SEM (ESEM)

The particle shape and morphology of the powders were acquired by SEM. A FEI Quanta 200 Environmental SEM (ESEM) was employed for characterizing the powders of interest. All powder samples were individually prepared with carbon tape to hold them in place in the SEM.

3.1.2 EDS

The chemical composition was obtained by the EDS, Oxford Instruments' INCA Software package, realizing EDS provides compositional analysis having relative accuracy when constituents are approximately 0.2% by weight. This was considered acceptable based on the objective of confirming alloy composition of the powder.

3.1.3 Particle size analyzer

The particle size distribution was analyzed by the laser scattering–wet dispersion method. The measurement was conducted with a Malvern Mastersizer "S" measurement equipment using a sample of the powder dispersed in isopropanol alcohol (IPA). This light scattering instrument provides the opportunity for wet measurements, while the light source operates at a wavelength of 633 nm. The equipment can measure particle sizes throughout a size range of 0.05 μm to 900 μm.

3.2 **Material preparation and selection**

Initial material selection was conducted with laser deposits of four different materials on a non-carburized low carbon steel substrate. The four selected deposition materials were: SS 431, SS 431 with 28.13 vol% (20 wt%) of TiC (SS 431/20 TiC), SS 431 with 53.07 vol% (40 wt%) of TiC (SS 431/40 TiC), and SS 431 with 70.14 vol% (60 wt%) of TiC (SS 431/60 TiC). The SS 431 – TiC powders were mixed by the weight percentage ratio before laser processing.

All selected materials were laser deposited with a single layer and a multi-layer deposition on to a low carbon steel substrate. All samples were examined by optical microscopy and measured using Vickers micro hardness testing. Two selected materials were determined for laser deposition on the carburized 8620 steel substrates. The exact deposition parameters were also developed to optimize deposition for defect-free and fully dense deposits.

Based on the results of initial material selection, deposition material SS 431/20 TiC and SS 431/40 TiC were selected for further evaluations on carburized 8620 steel substrates using a single layer deposition. Both samples were analyzed using microstructural images and micro hardness testing. A final deposition material was chosen for RCF testing. The RCF test specimen was not only tested by rolling contact fatigue, but also examined using microstructural images, micro hardness testing, and SEM and EDS analysis. Finally, the RCF specimen was measured for surface roughness after surface roller grinding.

Four different materials were selected for simulating chromium electroplating on Inconel 718®. The selected powder materials were Inconel 718®, SS 431, SS 431/20 TiC, and SS 431/40 TiC. All samples were examined by microstructural images and Vickers micro hardness testing. Surface roughness testing was also conducted on specimens after surface roller grinding.

3.3 **Process development**

Process development was conducted at the Center for Innovative Materials Processing through Direct Digital Deposition (CIMP-3D) at the Pennsylvania State University. The center currently houses three DLD systems, the Laser Engineered Net Shaping (LENS) MR-7 system, a Precitec laser deposit head on the Laser Articulating Robotic System (LARS), and the High Power High Deposition (HPHD) system. All systems represent the same process technologies, and process parameters are approximately interchangeable between the various machines. The distinction between the LENS and the LARS system is build envelop and laser power. The LENS has a build envelop of 30 cm x 30 cm x 30 cm, with a maximum power of 500 watts using an ytterbium fiber laser. The LARS system has a larger build envelop of 3.35 m x 3.35 m x 1.07 m,

with a maximum laser power of 12000 watts through an ytterbium fiber laser with a 200 μm fiber optic cable.

The initial laser deposition trials involved development of parameters that met the required deposition quality followed by detailed characterization involving optical microscopy and micro hardness testing. Process parameter for the initial laser deposition trials were based on a review of the literature [4] and prior experience. This resulted in a recommended contact angle between the deposition track and the substrate of 140 degrees. [4] This contact angle was found to be most suited for all of the powders that would be evaluated.

The original process parameters were developed for the LENS machine, with a powder feed rate of 0.826 cm^3/min with Ar carrier gas at 1.89 l/min (4 cfh), laser power at 350 watts at a wavelength of 1.07 microns, spot size of 2 mm, coaxial powder nozzle at 9.27 mm away from the substrate, a travel speed of 1.06 cm per second (25 in/min), and Ar shielding gas at 18.88 l/min (40 cfh). The resultant tracks produced beads having a contact angle of 141 degrees, being 0.711 mm (0.028 in.) in width, and 0.127 mm (0.005 in.) in height. The spacing between tracks, Δw_{track}, calculated using Equation 3 [4], was 1.905 mm (0.075 in.). Equation 3 may be used to determine the spacing between tracks that will result in a flat deposit which is necessary to prevent the formation of inter-track and inter-pass lack of fusion defects. The h is the height of the deposit track above the substrate, and the w is the width of the deposit track.

$$\Delta w_{track} = \frac{4hw\left(-2w^2 + h\left(8h + \sqrt{\frac{\left(-4h^2 + w^2\right)^2}{h^2}}\right)\right) + \left(4h^2 + w^2\right)^2 \mathrm{ArcSin}\left[\frac{4hw}{4h^2 + w^2}\right]}{64h^3} \qquad \text{Eq. (3)}$$

Based on prior experience and adjustments of the LARS process parameters for the SS 431 powder, it was concluded that applicable parameters for achieving good deposition quality were powder feed rate of 1.0 cm^3/min with Ar carrier gas at 9.44 l/min (20 cfh), 2000 Watts of laser power, spot size of 4 mm, coaxially powder nozzle at 10 mm away from the substrate, a travel speed of 1.06 cm per second (25 in/min), Ar shielding gas at 9.44 l/min (20 cfh), and additional trailing Ar gas at the melt pool to prevent oxidation during laser deposition at 14.16 l/min (30

cfh). The build size of the single track deposition was 3.2 mm (0.126 in) wide, height above substrate was 0.267 mm (0.0105 in), contact angle at 161°, and Δw_{track} spacing was 1.905 mm (0.075 in), which is shown in Figure 10.

For the contact fatigue samples or cylindrical specimens, a "helical" pattern was employed, with the tracks starting against the profile of the filet in the reduced section. The specimen was rotated during deposition at a speed (RPM) calculated with respect to the increased radius of the bar, which is shown in Equation 4. Therefore, the tangential velocity of the surface being deposited was maintained at a travel speed of 1.06 cm per second (25 in/min).

$$RPM = \frac{25}{2\pi\,[radius\ of\ bar + (layer\ thinckness \times number\ of\ layers)]} \qquad \text{Eq. (4)}$$

Parameters (laser power, travel speed, mass flow rate, track spacing, and layer thickness) were established using the SS 431 powder and remained consistent with the other deposition materials. The powder flow rate was adjusted to provide the same volumetric flow rate of material to the melt pool between materials of different density.

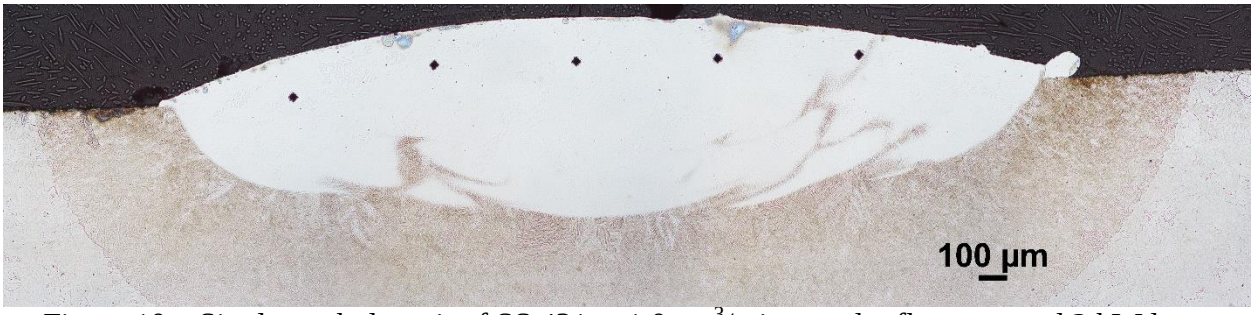

Figure 10 – Single track deposit of SS 431 at 1.0 cm^3/min powder flow rate and 2 kW laser power.

3.4 **Production of test specimens**

Upon selection of the stainless steel alloy 431 and the 431/20TiC composite material, specimens were prepared for further characterization of deposit attributes, such as rolling/sliding contact fatigue (RCF) testing. Four RCF test specimen were laser deposited

with SS 431/20 TiC on carburized 8620 steel bars. These specimens were produced at CIMP-3D using the LARS laser deposition system. The process parameters were adjusted to reduce heat input and dilution of the substrate during the deposition. The new process parameters were powder feed rate of 1.0 cm^3/min with Ar carrier gas at 9.44 l/min (20 cfh), 1000 Watts of laser power at a wavelength of 1.07 microns, spot size of 2.5 mm, coaxially powder nozzle at 10 mm away from substrate, a travel speed of 1.06 cm per second (25 in/min), Ar shielding gas at 9.44 l/min (20 cfh), and additional trailing Ar gas at the melt pool at 14.16 l/min (30 cfh). The build size of the single track deposition was 3.1 mm (0.122 in) wide, height above substrate was 0.378 mm (0.015 in), contact angle at 151°, and Δw_{track} spacing was 1.27 mm (0.05 in), Complete process parameters for both process development and specimen production are listed as Appendix A.

Shown in Figure 11a and Figure 11b are the carburized 8620 base material and deposition specimens that were used for producing samples for RCF testing. As shown in Figure 11a, the carburized 8620 steel specimens for contact fatigue tests were 2.515 cm (0.9905 in.) in diameter and 12.42 cm (4.89 in.) in length. A small recess approximately 0.0318 mm (0.00125 in.) in depth and 2.29 cm (0.9 in.) wide was machined into the bar at the center. Deposits approximately 3.43 cm (1.35 in.) in width and 0.254 mm (0.010 in.) thick were deposited circumferentially onto the recess at the midpoint of the bar, shown in Figure 11b. Photographs of the specimens produced for characterization are shown in Figure 12. After deposition, the final dimensions, shown in Figure 13, were obtained by roller grinding at Quala-Die, Inc. at St Marys, PA to the dimensions shown in Figure 14.

The production of Inconel 718® specimens is shown in Figure 15. The Inconel 718® turbine shaft was laser deposited with powder materials of Inconel 718®, SS 431, SS 431/20 TiC, and SS 431/40TiC. The process parameters that were utilized were the same parameters that were developed during process development. The powder flow rate was adjusted based on material densities, which provided the same volumetric flow rate of material at 1.0 cm^3/min. The four laser deposited samples were roller ground to match the surface finish requirement at Quala-Die, Inc. Figure 16 shows the finished samples.

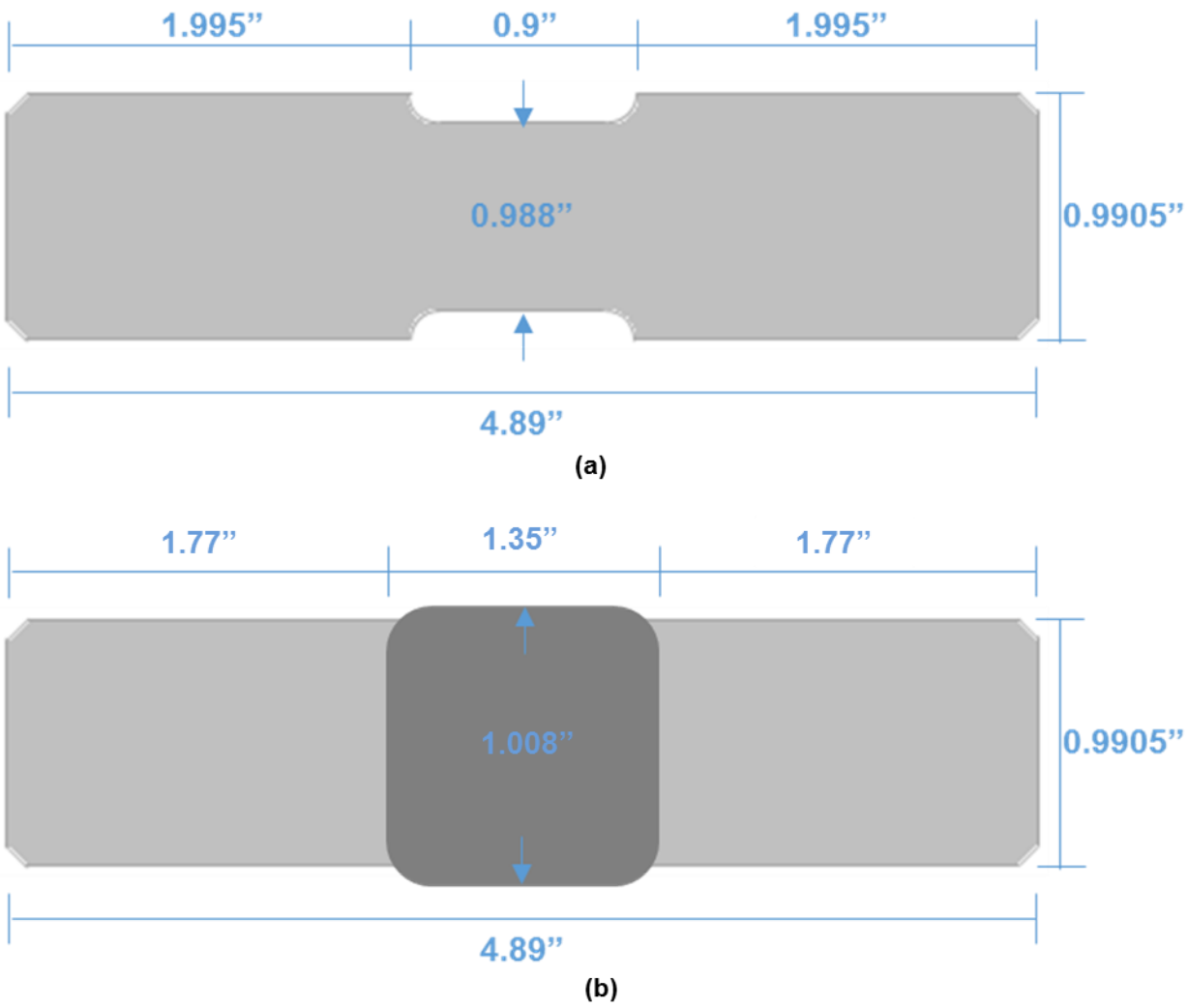

Figure 11 – Schematics of the specimen produced for RCF testing (a) initial machined specimen. (b) Specimen after with laser deposition materials over the center of carburized 8620 steel bar (Units are inches).

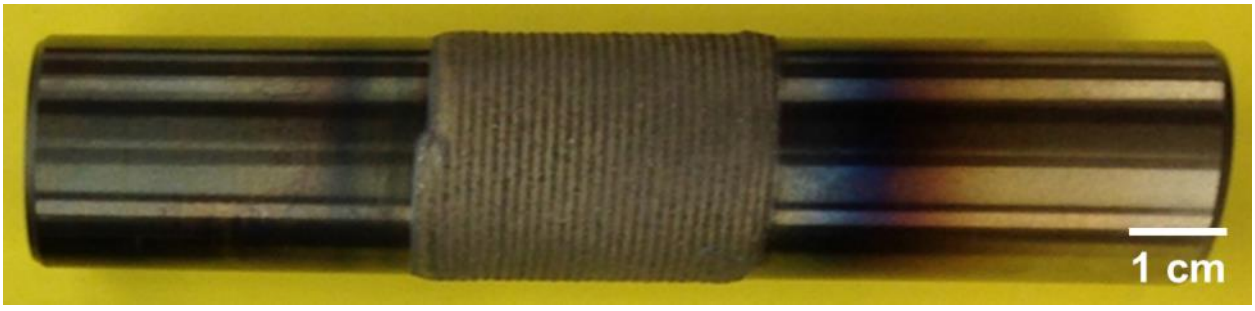

Figure 12 – Carburized 8620 steel specimen that had been laser deposited with SS 431/20 TiC.

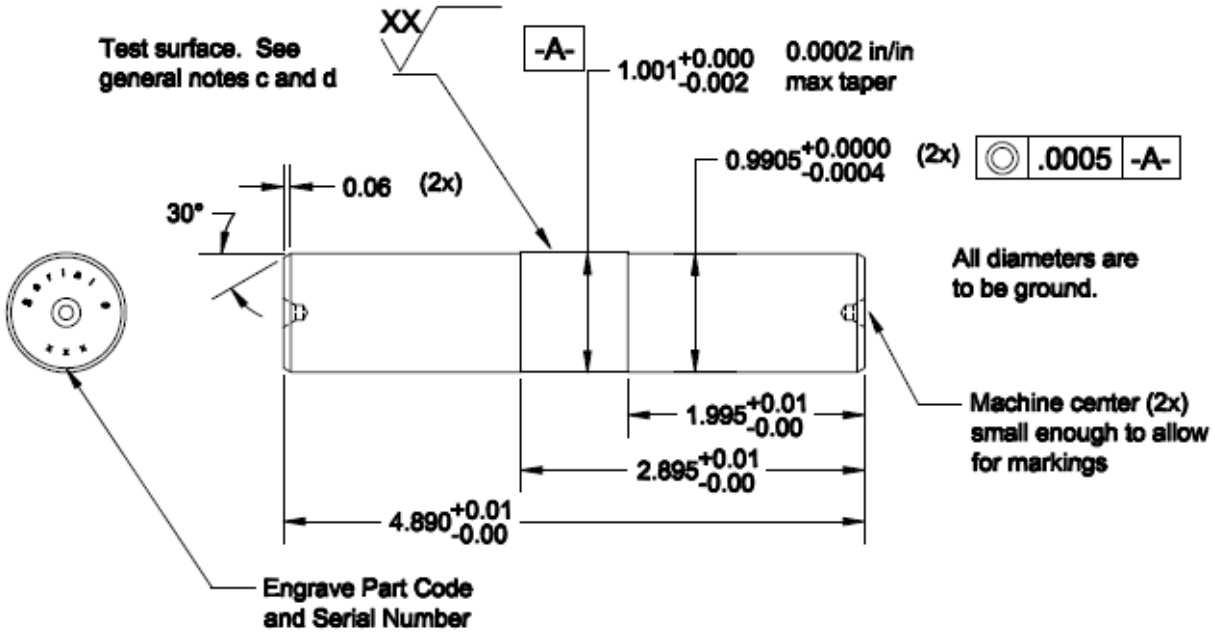

Figure 13 – The final dimension of the RCF test specimen.

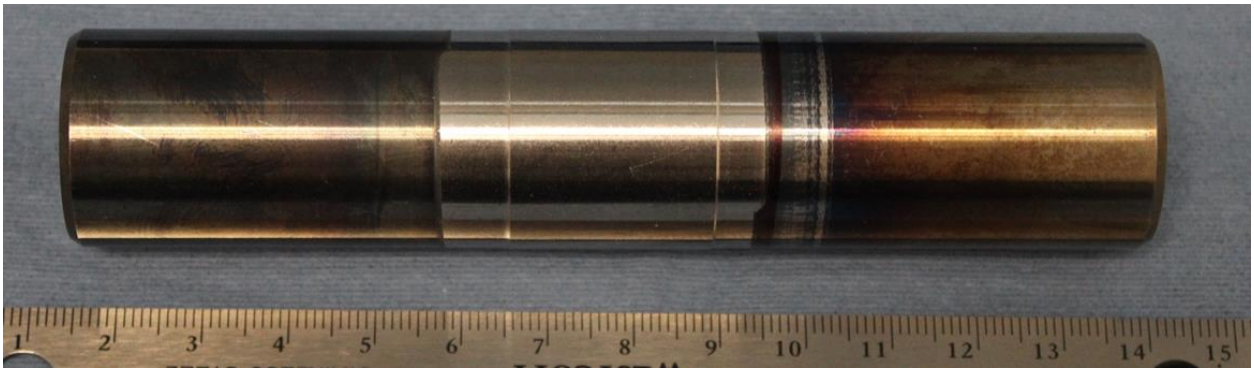

Figure 14 – The RCF test specimen with laser deposited SS 431/20 TiC (scale in cm).

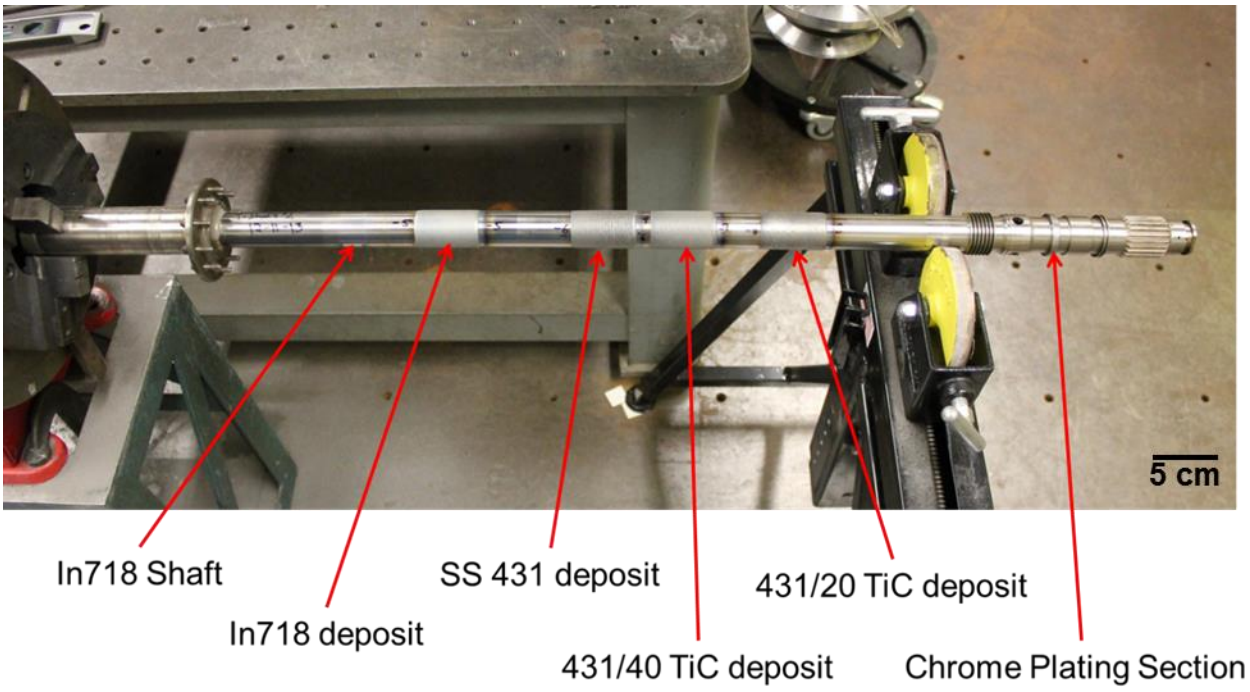

Figure 15 – Inconel power shaft showing laser deposition with selected materials.

Figure 16 – Laser deposited materials on Inconel 718® power shaft after roller grind machining (scale in cm).

3.5 **Specimen characterization**

3.5.1 Microstructural analysis

All samples were removed from the cylindrical specimens by wet cutting using a Struers Labotom-3 and were then hot mounted in epoxy resin using a Struers Pronto-Press 2. All samples were ground and polished on a Struers Pedomax-2. Grinding utilized various grits including 240, 320, 400, 500, 600, 800, 1000, 1200, and 2400. Each grit size was used for two

minutes, followed by a rinse prior to the subsequent paper. After the samples were ground, they were polished using a 3 micron diamond suspension and 1 micron diamond suspension. The samples were polished for 3 minutes each with the diamond suspensions, alternating the use of the diamond suspension and a polishing lubricant (Blue Lube) every 15 seconds. The colloidal silica was used for 3 minutes, alternating between silica and distilled water being sprayed on the polishing pad every 15 seconds.

All samples were etched for microstructural imaging after polishing using a 2% Nital solution. The Nital solution was applied for 5 seconds to etch the 8620 steel substrate and HAZ. Deposit materials, Inconel 625, SS 431, and SS 431/TiC composite, required electrolytic etching with 10% oxalic acid solution. Due to electrolytic etching of the deposited materials, over etching of the HAZ and 8620 steel substrate occurred. Therefore, both 8620 steel substrate and HAZ microstructural images were taken before electrolytic etching.

3.5.2 Vickers hardness test

After metallographic analysis, micro hardness measurements were conducted based on the ASTM-E384 specification [23] using a Leco M-400-G1 micro hardness tester in the Vickers scale. This was conducted by applying a 300 gram load. Before micro hardness testing, samples were re-ground, re-polished, and etched lightly with the 2% Nital solution to reveal the heat affected zone (HAZ). Since the HAZ was so narrow, hardness samples were taken in a staggered procedure using two rows separated by 0.5 mm and depth spacing of 0.125 and 0.25 mm from the top surface of the deposit, and resulting in 4 to 6 rows on each sample. Figure 17 demonstrates the location and spacing for micro hardness testing. This was performed to ensure that prior indentations and deformation zones were at least 2.5 times away from prior indentations, and would not affect the results of the current hardness measurement. A hardness conversion chart, Appendix B, was used to convert the reference hardness in Rockwell C (HRC) unit to Vickers hardness (HV) units. The complete Vickers hardness testing for each test indent is listed in Appendix C. [24]

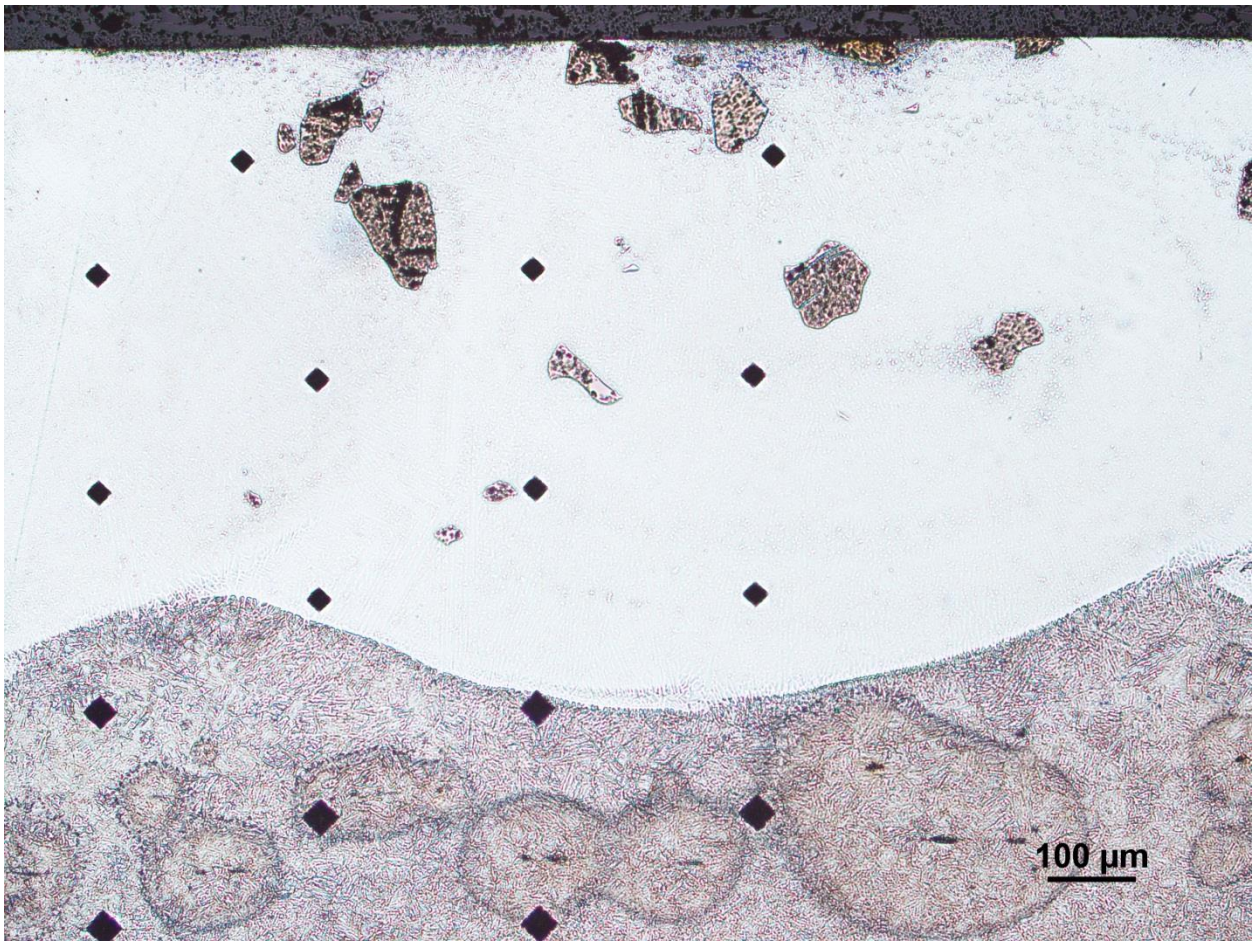

Figure 17 – Demonstrating the staggered procedure for measuring micro hardness.

3.5.3 EDS – mapping analysis

EDS mapping provided images of elemental distributions within the sample. Element maps show the spatial distribution of elements in a sample. Maps of different elements over the same area can help to qualitatively determine phases that are present. Element maps provide a complete two-dimensional picture of chemical distribution within the sample. [25,26]

The mapping analysis was conducted while performing SEM and EDS at the same time. The results of elemental mapping were computed in the mapping setting of the INCA Software.

3.5.4 Rolling contact fatigue test

The rolling contact fatigue (RCF) test simulates the rolling and sliding action that occurs in a gear mesh. Figure 18 shows a general schematic of the rolling contact fatigue test, and Figure 19 is a picture of the rolling contact fatigue test rig. The specimen and load rollers are cylindrical. The outside diameter of the load roller is crowned to concentrate the load at the center of contact, and eliminate the possibility of concentrated loading at the edge of contact due to misalignment. A normal load is applied by air pressure. Phasing gears, attached to the shafts on which the specimen and load rollers are mounted, control the extent of sliding at the specimen/load roller interface. For this testing, 56 tooth and 16 tooth gear were utilized to cause the load roller surface velocity to be 1.21 times that of the specimen velocity. Tests were conducted at 3000 RPM, and a 2068 MPa (300 ksi) stress load. Complete details of the test are shown in Table 8. [22]

The intent for this evaluation was to compare the performance of the specimens representing the deposited material to prior data representing the 8620 base metal that had been carburized. All tests were conducted in oil heated to 70°C (158°F). Searching tests were conducted with a baseline group of specimens to find loads that resulted in initial surface durability failures.

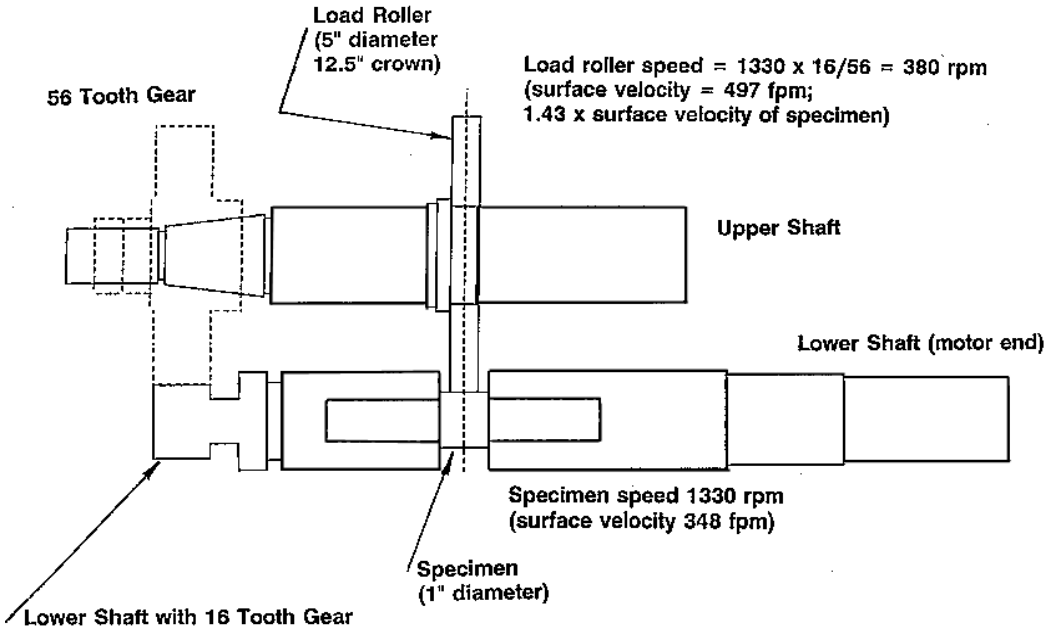

Figure 18 – Schematic of the rolling contact fatigue test. [21]

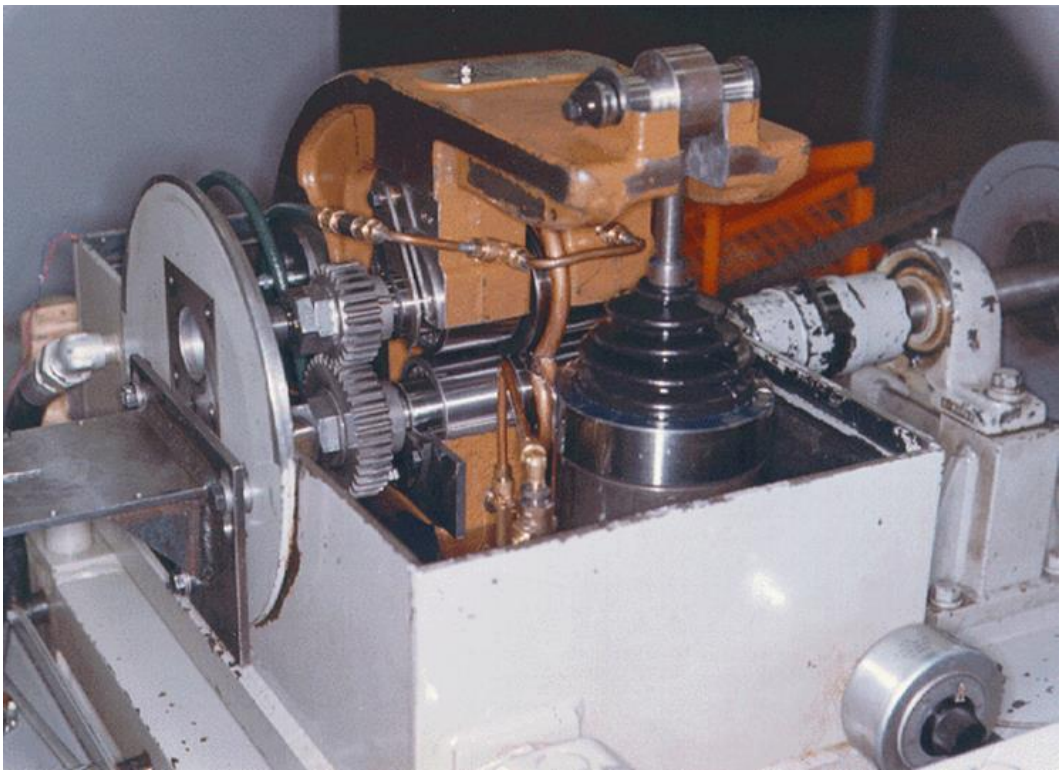

Figure 19 – Photograph of the rolling contact fatigue test at the Drivetrain Technology Center of the Applied Research Laboratory.

Table 3 – Rolling Contact Fatigue Testing condition details.

RPM:	3000 (approximately)
Phasing Gear Set:	16/56 Tooth
Test Plan:	1) Conduct searching tests to find loads to result in 12-15 million cycles to pitting and 30-50 million cycles to pitting. First searching load 350 KSI. 2) Conduct six tests at each load. Use three machines (two at each load on each machine). Work this testing with that for Half Factorial Conditions 1-6, and 8.
Run Out Limit:	100 million cycles
Run-in:	Stabilize at temperature. Roll over by hand with no load on load rod. Run 10 minutes at each of 25%, 50% and 75% contact stress. Reset timer and run 10 minutes at test stress.
Lubricant:	Texaco OEM DEXRON III
Lubricant Temp:	70°C (158°F)
Filter:	10 micron (nominal)
Lubricant Change Interval:	about 1200 hours
Wear Measurement:	Measure diameter of specimen at start of test, at each inspection, and at end of test. **STOP TEST IF WEAR EXCEEDS 0.0015 INCHES DIAMETER REDUCTION.** For long tests with low wear, measure diameter every other inspection.
Special Notes:	Inspect all specimens and load rollers per attached.

3.5.5 Tribology analysis

A Zygo NewView 7300 optical profilometer at the Materials Characterization Laboratory was used for measuring surface roughness. Zygo optical profilometer is a non - contact profilometer which measures light reflection from the surface of the test samples. A beam from the instrument is split into two paths by a beam splitter. One path lights onto the sample surface, and the other lights to a reference mirror. Reflections from both paths of light projected onto a detector. The different wavelengths of light occur due to height variances from the test sample and reference surfaces. The software package, MetroPro, measures the height difference from bright and dark bands, and generates a surface measurement 3D map along with surface roughness measurement. [27,28] The complete results of the tribology analysis results which generated by Metro are included in Appendix D.

Chapter 4. CHARACTERIZATION RESULTS AND DISCUSSION

4.1 **Materials characterization results**

4.1.1 AISI 8620 steel

AISI 8620 steel contains a wide range of alloying additions that typically include C, Mo, Cr, Mn, Mo, Ni, and Si, fixed for carbon steels. The chemical composition of 8620 steel is shown in Table 4. [20] These types of steels are more responsive to mechanical and heat treatments than plain carbon steels. Alloy 8620 steel is a common, carburizing alloy steel. This steel is flexible during hardening treatments, thus enabling improvement of case/core properties. Normalized 8620 steel has a hardness of approximately at 270 HV; however, carburization of 8620 steel develops an excellent wear resistant surface in the range of 700 to 760 HV (60 – 63 HRC). Properties of interest for the 8620 steel for this study are shown in Table 5. [20]

Table 4 – Chemical composition of 8620 steel alloy.

	Fe	Cr	Ni	Mn	Mo	C	Si
8620 Steel	96.9-98.02	0.4-0.6	0.4-0.7	0.7-0.9	0.15-0.25	0.18-0.23	0.15-0.35

Table 5 – Properties of interest for 8620 steel alloy. [20]

Theoretical Density (g/cm^3)	Melting Temperature (°C)	Normalized Hardness (HV)	Carburized Hardness (HV)
7.85	1427	272	697 – 763

4.1.2 AISI stainless steel 431

AISI stainless steel alloy 431 (SS 431) is a case hardenable steel that exhibits excellent corrosion resistance. Martensitic stainless steels contain more than 10.5 wt% Cr along with other austenite-stabilizing elements, such as carbon, nitrogen, nickel, and manganese, to expand the austenite phase field and permit heat treatment. The nominal composition of alloy 431 is Fe-0.2C-1Si-1Mn-16Cr (wt%). [29] The composition must be carefully balanced to prevent delta-ferrite formation at the austenitizing temperature. Delta-ferrite in the hardened structure should be avoided for embrittlement and attain the best mechanical properties. Alloy 431 also has excellent tensile and torque strength, and good toughness.

The stainless steel alloy 431 powder was acquired from Carpenter Technology, with a particle size of between 45 to 149 μm (-100/+325 mesh). The powder was gas atomized. As shown in Figure 20, the particles are spherical. The image of Figure 21 shows the topography of a particle, which indicated a rough texture. The sub particle structure was small and densely formed. The mean particle size (d_{50}) was found to be 87 μm with a standard deviation of 45.4 μm, which is shown in Figure 22. The EDS spectrum for the SS 431 is shown in Figure 23. A chemical composition comparison is shown in Table 6, and matches the nominal reference composition. [29] However, relatively high levels of carbon were found to be present and may be due to sample preparation with carbon tape. Properties of interest for SS 431 are shown in Table 7. [29]

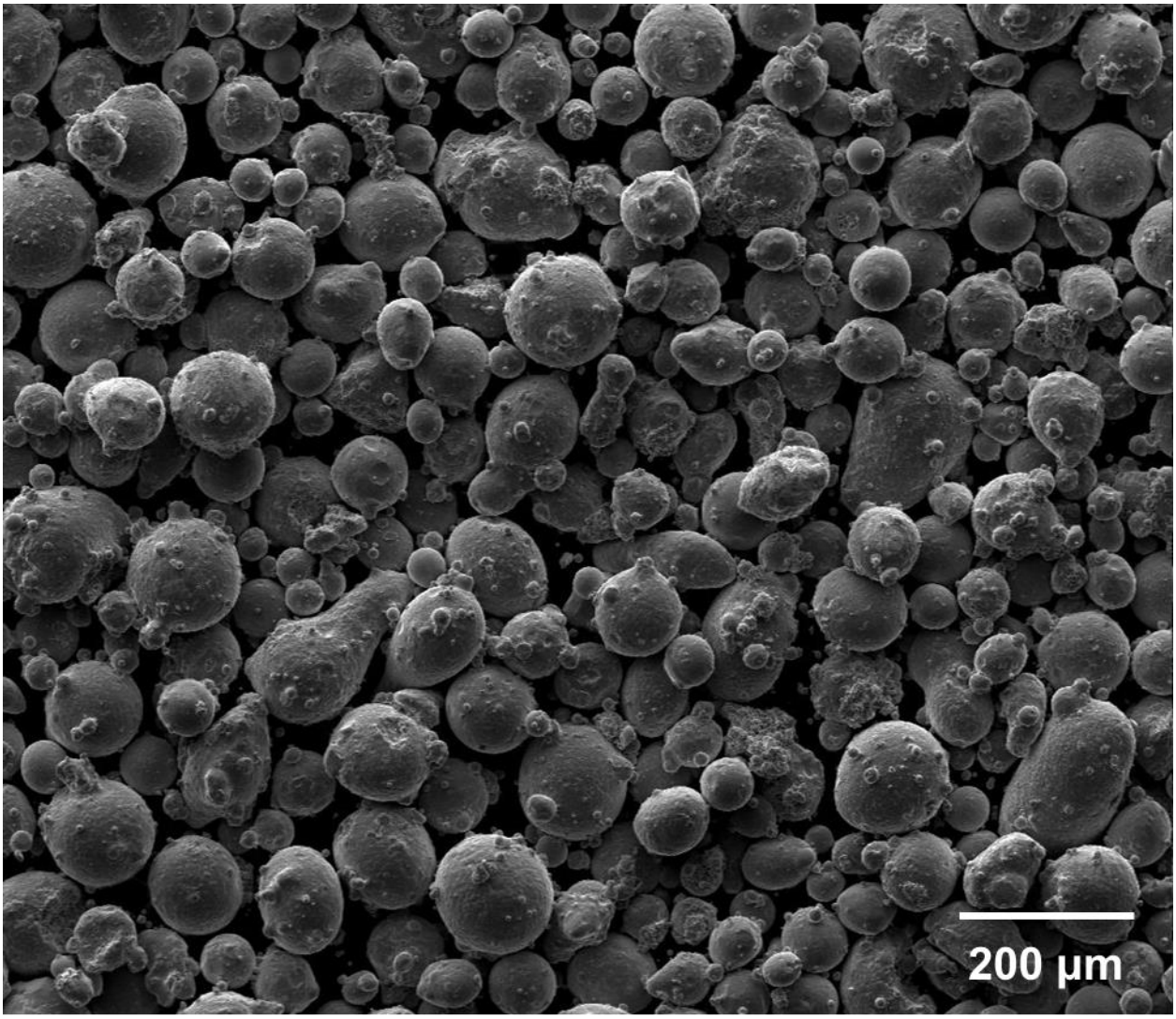

Figure 20 – SEM image of SS 431 particles of powder obtained from Carpenter Technology.

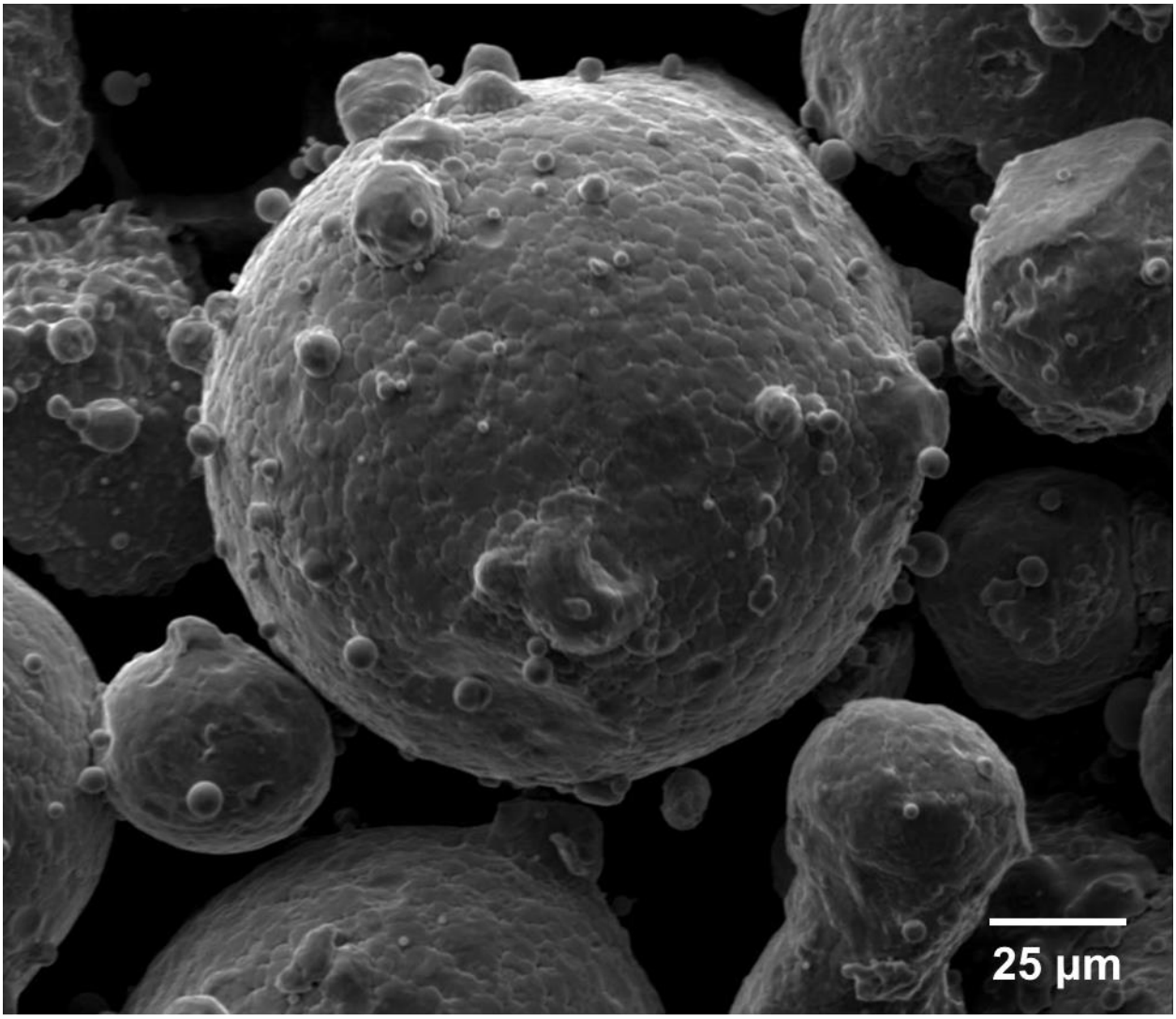

Figure 21 – SEM image of SS 431 particle with satellites around the dense spherical particle of powder obtained from Carpenter Technology.

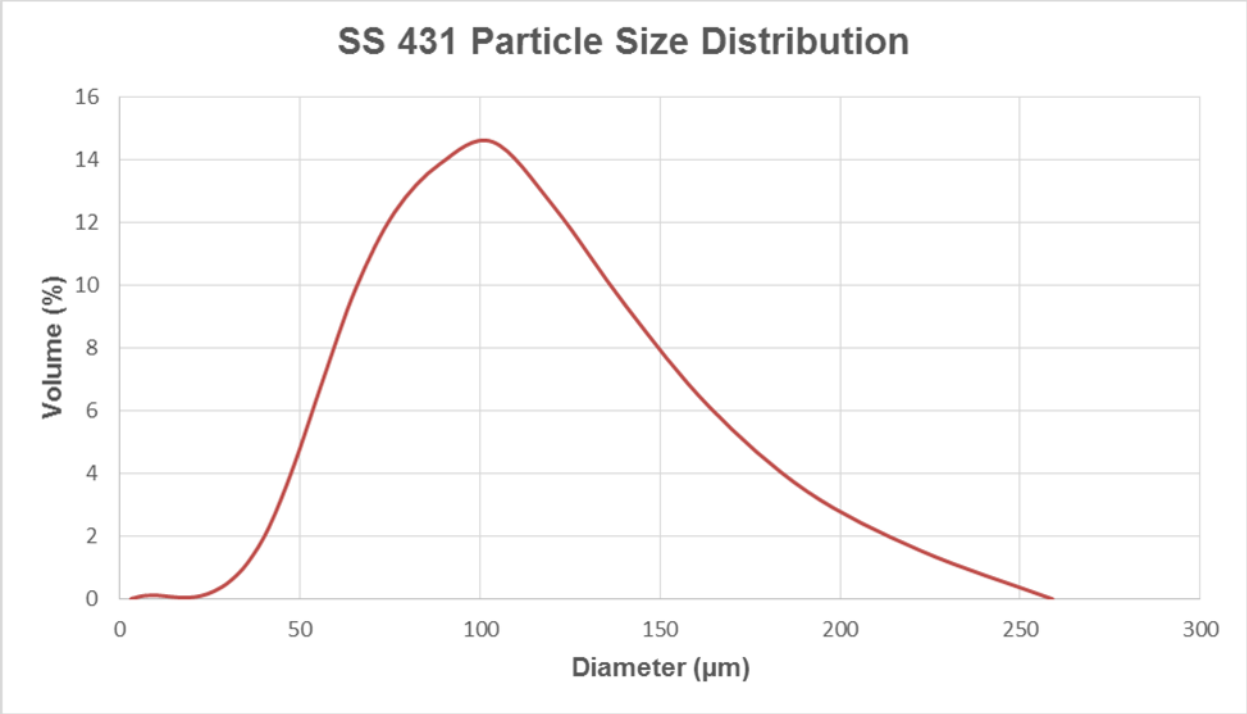

Figure 22 – Particle size distribution of SS 431 powder.

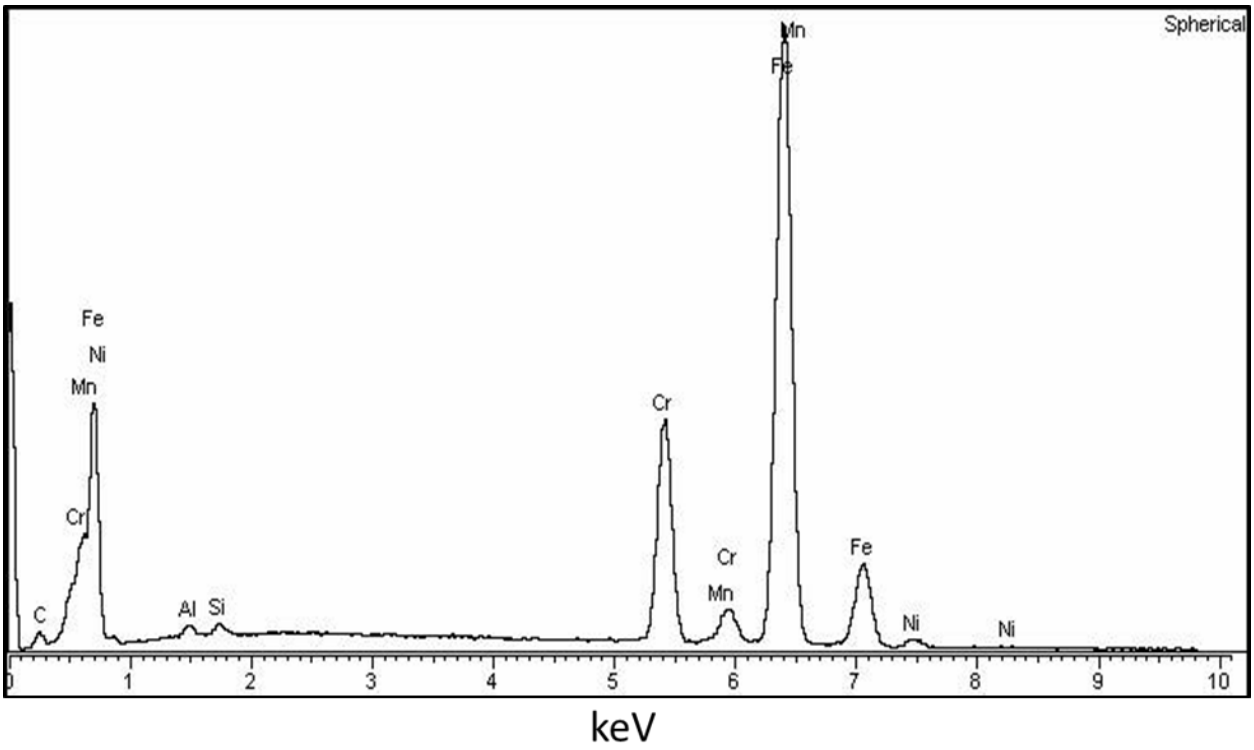

Figure 23 – EDS spectrum of SS 431 powder.

Table 6 – Measured and reported nominal chemical compositions for SS 431 powder.

wt%	Fe	Cr	Ni	Mn	C	Si	Al
SS 431	79.17	15.58	1.36	0.44	2.5	0.4	0.54
Reference[29]	80	15-17	1.25-2.25	1	0.2	1	-

Table 7 – Properties of interest for SS 431. [29]

Theoretical Density (g/cm^3)	Melting Temperature (°C)	Hardness (HV)
7.8	1482	392

4.1.3 Titanium carbide

The titanium carbide (TiC) powder is an extremely hard ceramic material. Titanium carbide has excellent properties for wear and corrosion resistance, which aided the decision to utilize this material within the metal matrix.

The TiC powder was obtained from AEE Corporation, with a particle size of 45 to 149 μm (-100/+325 mesh). The AEE TiC powder was manufactured by carburizing titanium particulate and found to be irregular in shape, and is shown as Figure 24. The particles exhibited pores and debris on the surface, and this is shown as Figure 25. The mean particle size (d_{50}) was found to be 88 μm with a standard deviation of 41.5 μm, which is shown in Figure 26. The EDS spectrum for the TiC is shown in Figure 27. A comparison of measured and reported composition is shown in Table 8, and the measured composition was similar to the nominal composition. [30] There was also a small amount of vanadium (V), approximately 0.3%, that was observed in the TiC powder, and was probably in the TiC raw material. Properties of interest for the TiC are shown in Table 9. [30]

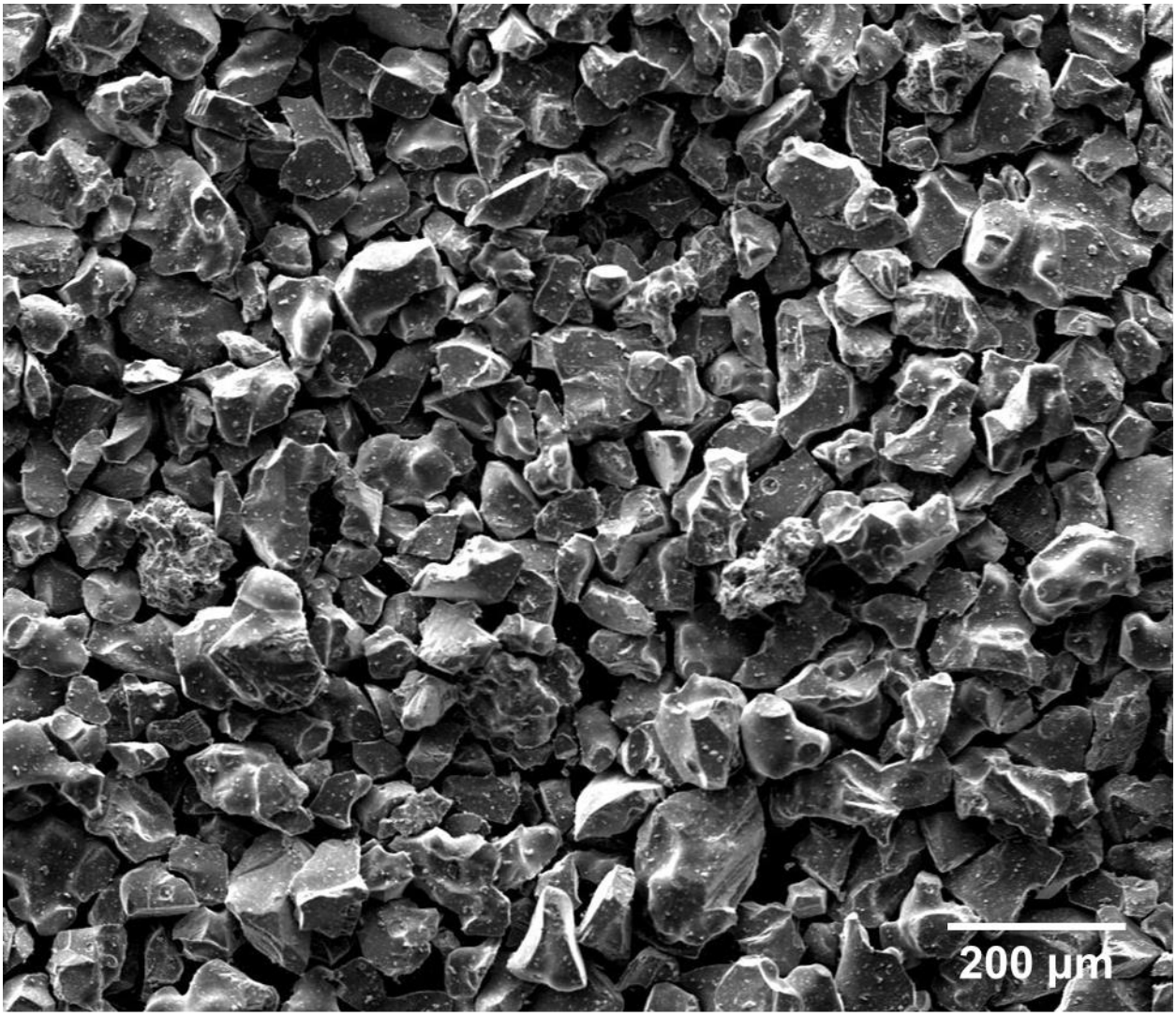

Figure 24 – SEM image of TiC particles of powder obtained from AEE Corporation.

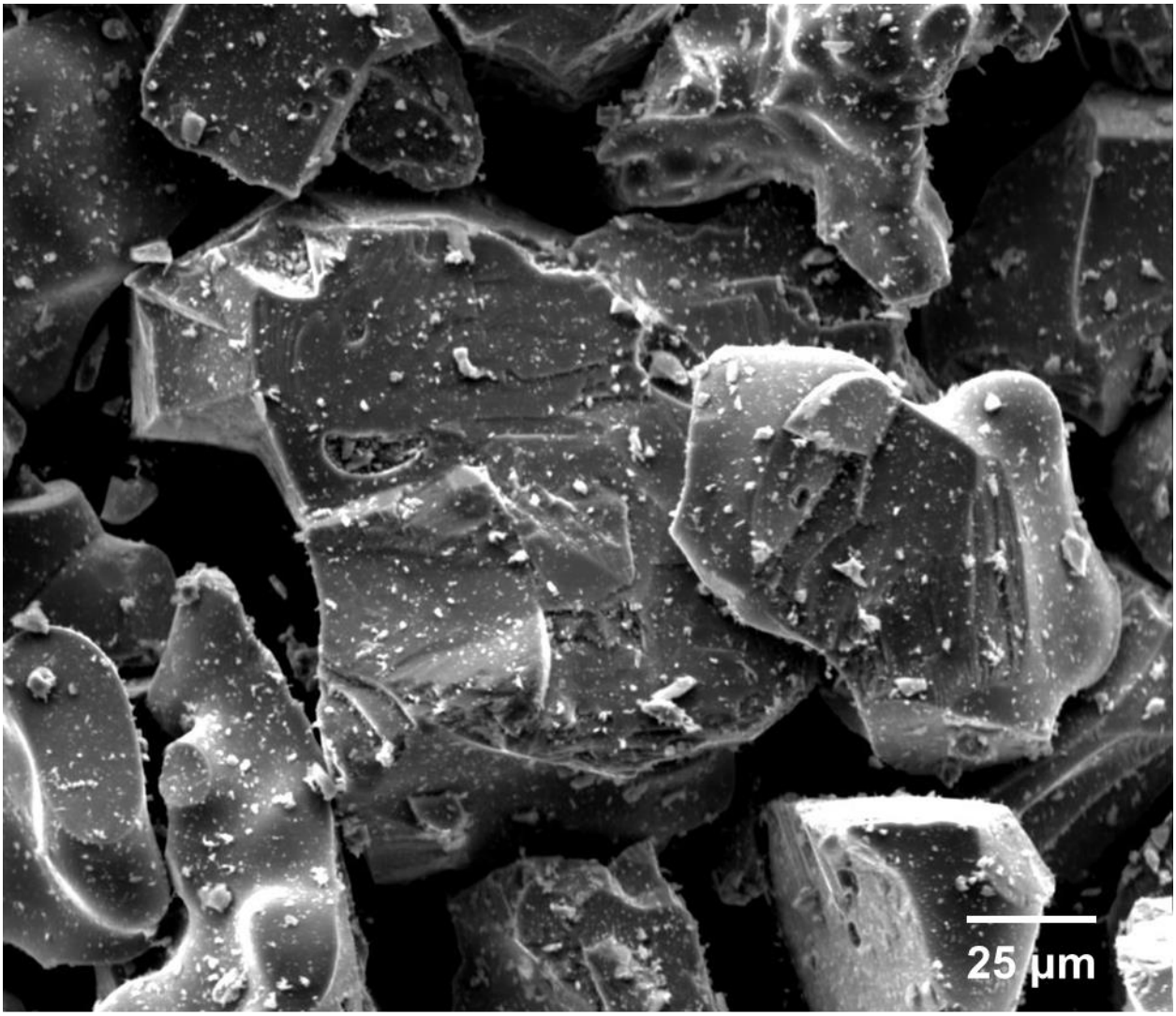

Figure 25 – SEM image of TiC particle with pores at the surface of powder obtained from AEE Corporation.

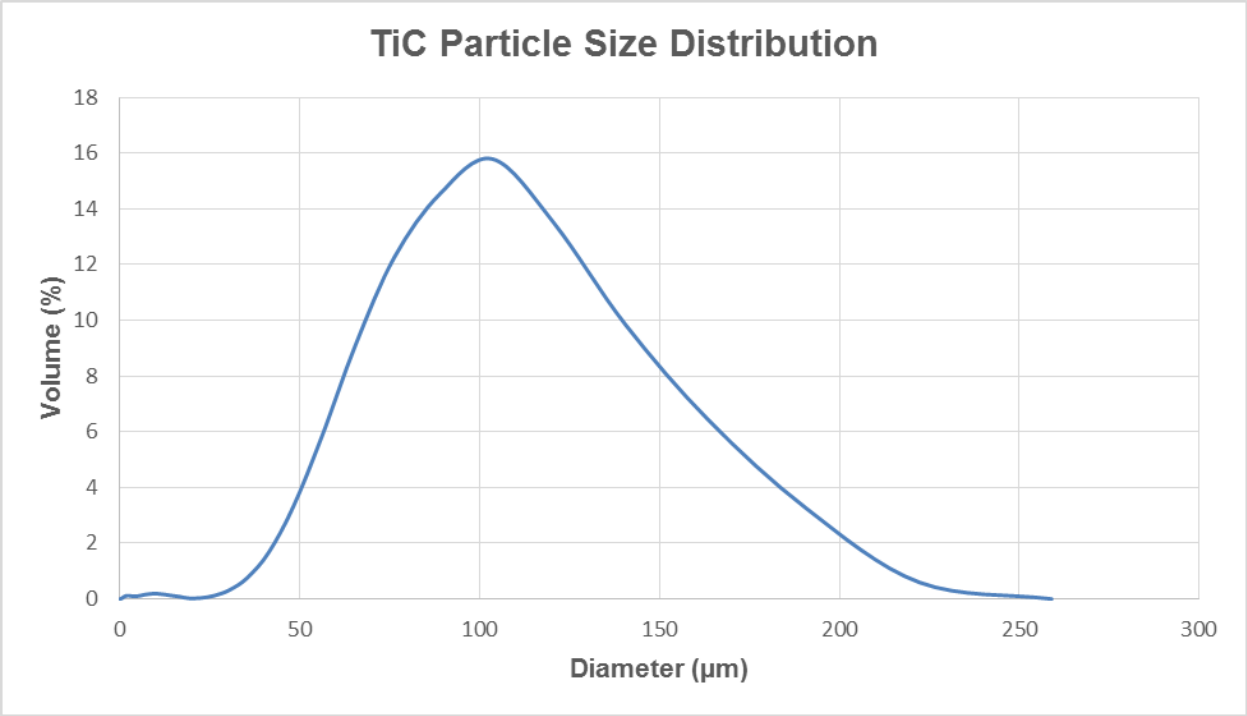

Figure 26 – Particle size distribution of TiC powder.

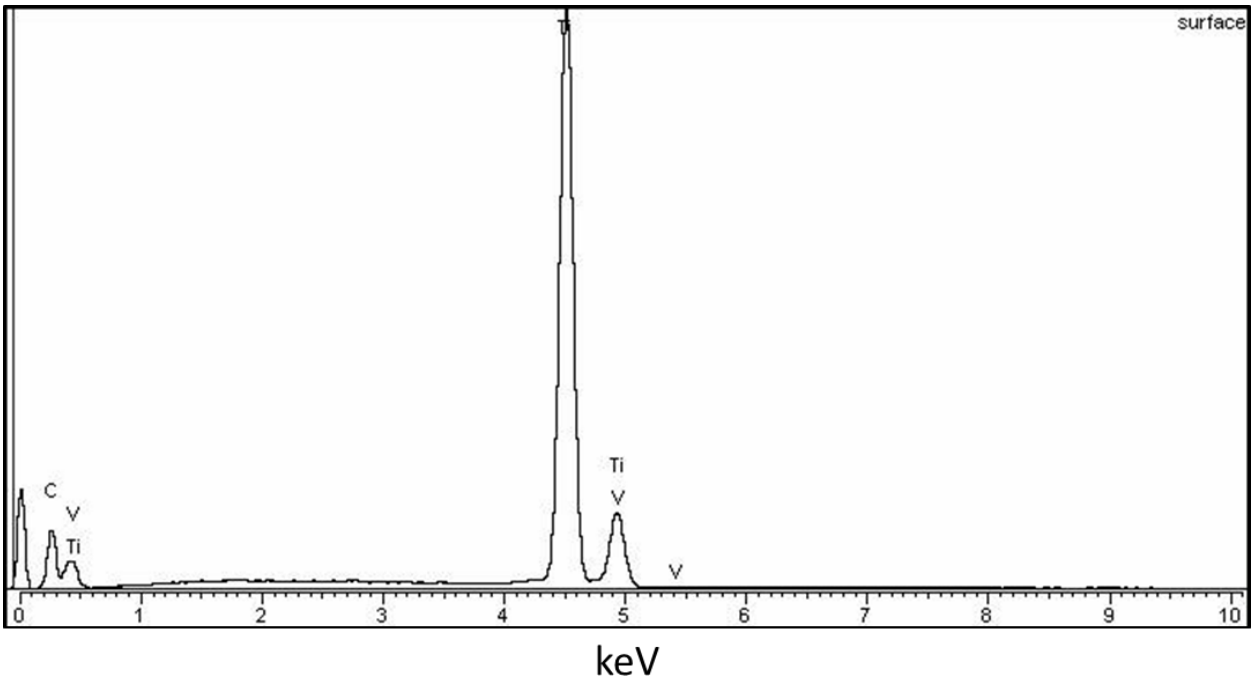

Figure 27 – EDS spectrum of TiC powder.

Table 8 – Measured and reported nominal chemical compositions for TiC powder.

wt%	Ti	C	V
TiC	83.81	15.85	0.34
Theoretical [30]	79.9	20.1	–

Table 9 – Properties of interest for TiC. [30]

Theoretical Density (g/cm^3)	Melting Temperature (°C)	Hardness (HV)
4.93	3140	3500

4.1.4 Inconel 718®

Inconel alloy 718® is a high-strength, corrosion-resistant, nickel chromium material used in the temperature range of -252.8°C to 704°C. The nominal composition of Inconel 718® is Ni-19.0Cr-18.0Fe-3.0Mo-5.0Nb+Ta-1.0Ti (wt %). [31] The strength of alloy 718 is dependent on the precipitation of secondary phases, such as gamma prime (γ') and gamma double prime (γ''). Inconel 718® is used in a variety of applications because of the ease and economy with which it can be fabricated, combined with its good tensile, fatigue, creep, and rupture strength.

Inconel 718® powder was acquired from Sulzer Metco with a particle size of between 45 to 125 μm (-120/+325 mesh). The powder was gas atomized, and spheroidal in shape. Most of the particles were similar in size, which is illustrated in Figure 28. The powder appeared to have no signs of contamination; however, a small amount of satellites are observed in Figure 29. The mean particle size (d_{50}) is 78 μm with a standard deviation of 30.0 μm. The measured size distribution is shown in Figure 30. The EDS spectrum is shown in Figure 31, and a complete compositional comparison is listed as Table 10. The measured composition is similar to the reported nominal composition of Inconel 718®. [32,33] Properties of interest for Inconel 718® are shown in Table 11. [32,33]

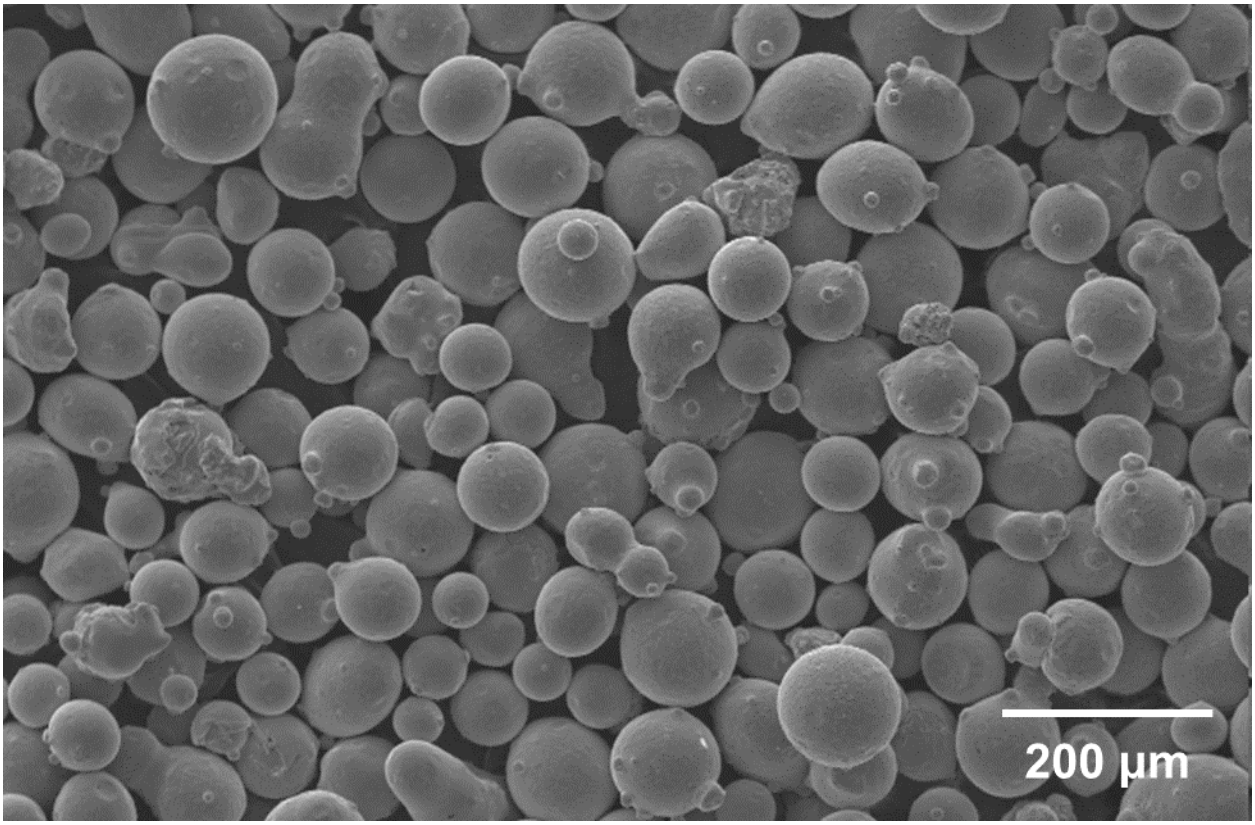

Figure 28 – SEM image of Inconel 718® spherical particles of powder obtained from Sulzer Metco.

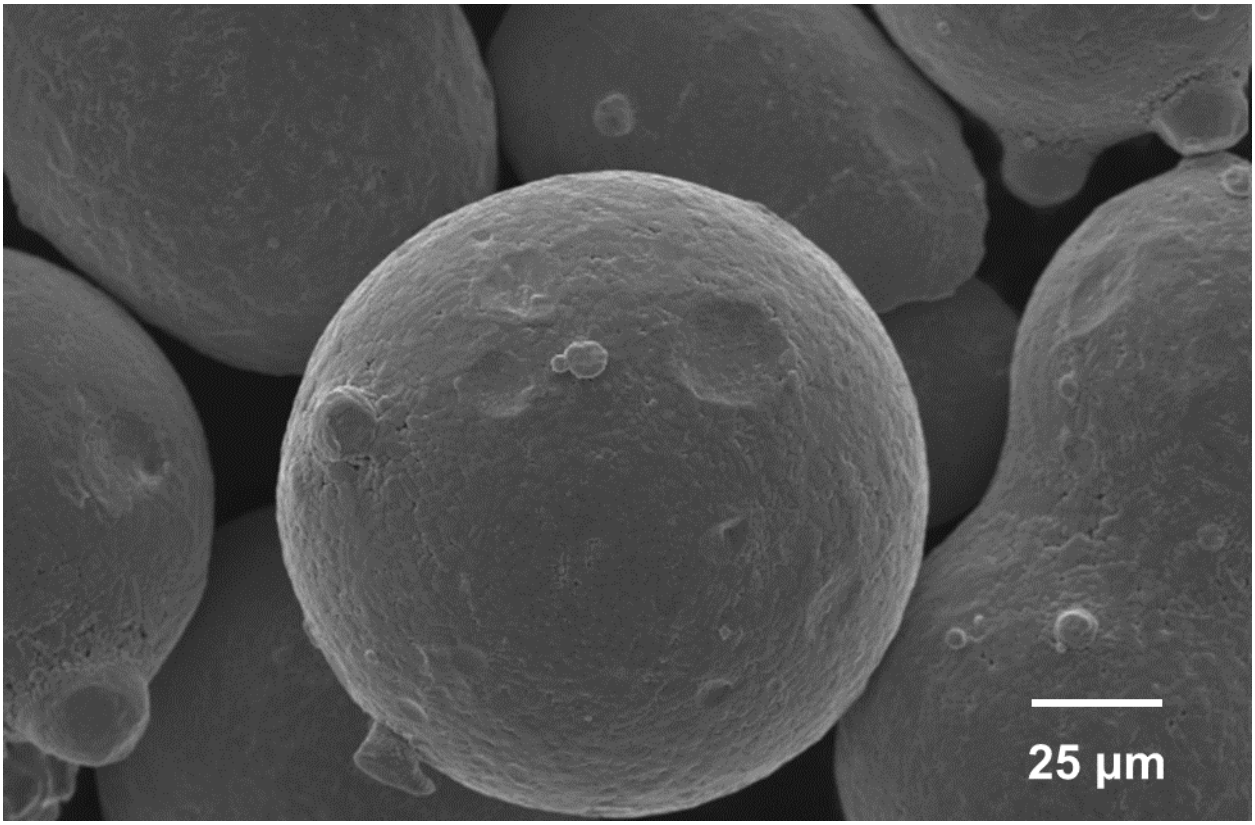

Figure 29 – SEM image of dense spherical Inconel 718® particle of powder obtained from Sulzer Metco.

Table 10 – Measured and reported nominal chemical compositions for Inconel 718® powder.

wt%	Ni	Cr	Fe	Nb+Ta	Mo	Ti	Al	Cu	Co
Inconel 718®	50.78	19.08	18.87	4.6	3.35	1.32	0.83	0.78	0.42
Reference[31]	53	19	18	5	3	1	0.5	–	1

Table 11 – Properties of interest for Inconel 718®. [32,33]

Theoretical Density (g/cm^3)	Melting Temperature (ºC)	Hardness (HV)
8.19	1260 – 1343	272

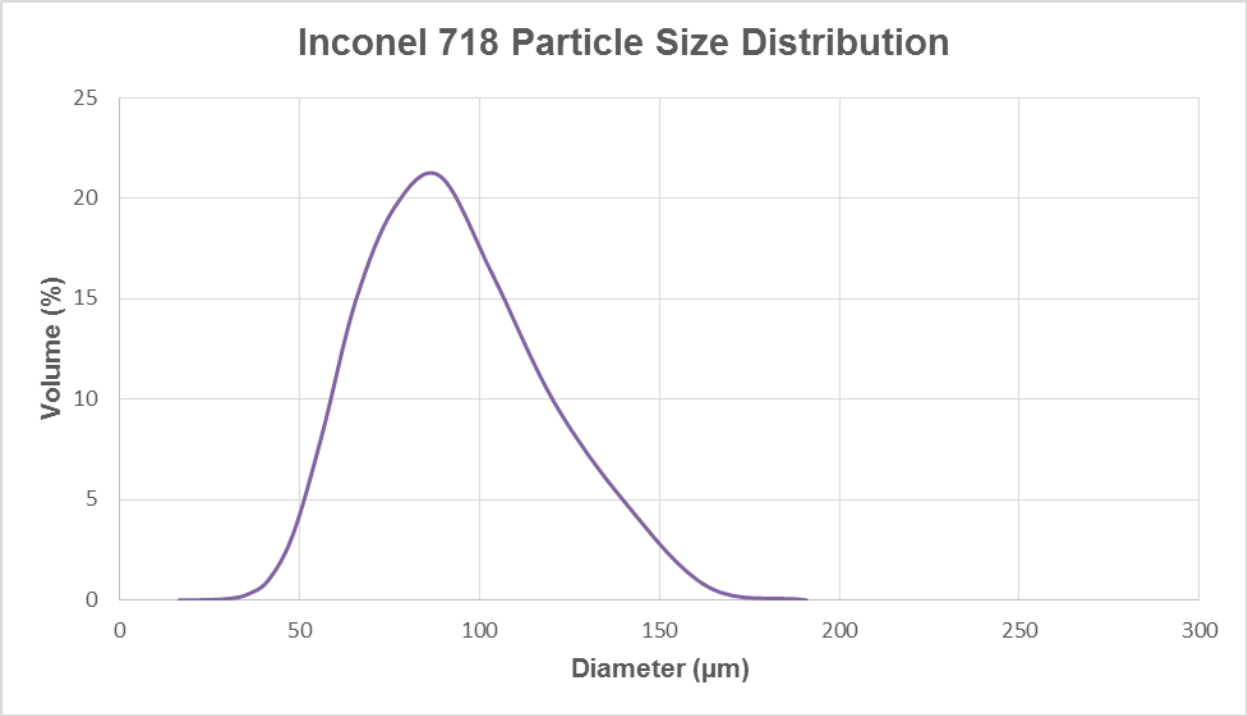

Figure 30 – Particle size distribution of Inconel 718® powder.

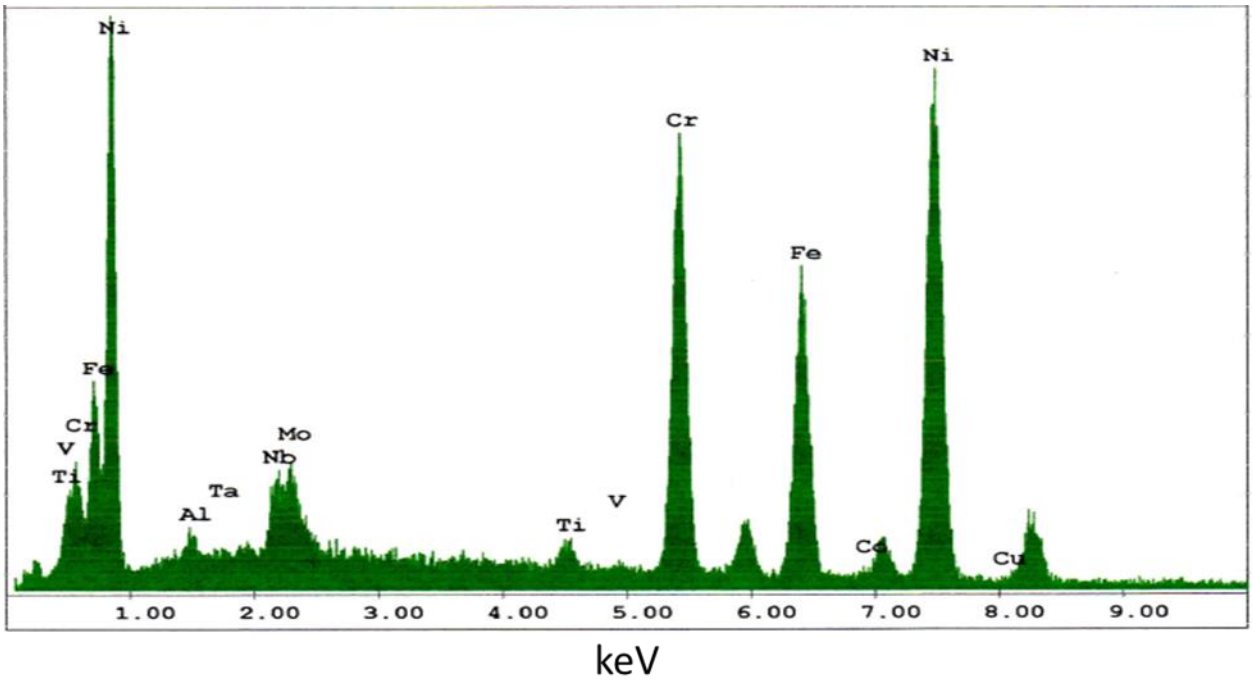

Figure 31 – EDS spectrum of Inconel 718® powder.

4.2 **Characterization of Laser Deposited Materials**

4.2.1 Microstructural analysis

4.2.1.1 Process development specimens

Optical microscopy provided insight into the development of the cast microstructure of the laser deposits for the various deposition materials and resultant microstructures of the heat affect zone (HAZ) in the non-carburized steel substrate. Microstructural images were obtained for all deposition materials, with images originally taken by optical microscopy at 500X magnification. Images were "stitched" to provide a broad view that included deposition materials, HAZ, and the non-carburized steel substrate. These images were obtained at 100X magnification. The microstructural images of the deposition materials deposited on low carbon steel are shown in Figures 32 to 35. Figures 36 and 37 show additional images of deposition material deposited onto carburized 8620 steel substrate.

Figure 32 shows the fully dense and defect free deposits of (a) single layer and (b) multi-layer SS 431. Figure 33(a) shows the fully dense and defect free SS 431/20 TiC deposit as a single layer deposited on low carbon steel. Figure 33(b) represents the multi-layer of SS 431/20 TiC deposit, and Figure 34(a) shows a fully dense and defect free single layer SS 431/40 TiC deposit, Figure 34(b) represents the multi-layer SS 431/40 TiC deposit with a small crack at the interface region. Figure 35(a) shows the fully dense single layer SS 431/60 TiC deposit, and Figure 35(b) represents the multi-layer SS 431/60 TiC showing a crack between the top of two deposit tracks. The size of the cracks increased with higher concentration of TiC. The microstructures of the deposits represented a fine, as cast microstructure for the respective material systems. Besides the defects on the surface of the deposition materials having high TiC loading, the microstructures also exhibited a higher concentration of TiC particles, as well an increase in finer features within the matrix, shown as a fine grey phase. These small dark grey features are believed to represent precipitation of a secondary phase due to available Ti and C that was dissolved from the original TiC particles during laser deposition.

The microstructural cross-sections of two materials deposited on carburized 8620 steel substrate are shown in Figure 36. The microstructural images indicated that unmelted TiC

particles tended to remain at the top of deposit surface. This is believed due to the relatively lower density of TiC particles providing buoyancy within the molten SS 431 pool. Multiple boundary lines also appeared within the microstructure and delineated the multiple tracks. This observation is reinforced in the image of Figure 37. The length of the boundary line increased at higher TiC content. These boundary lines may also indicate cracks that have been backfilled by liquid during the deposition process.

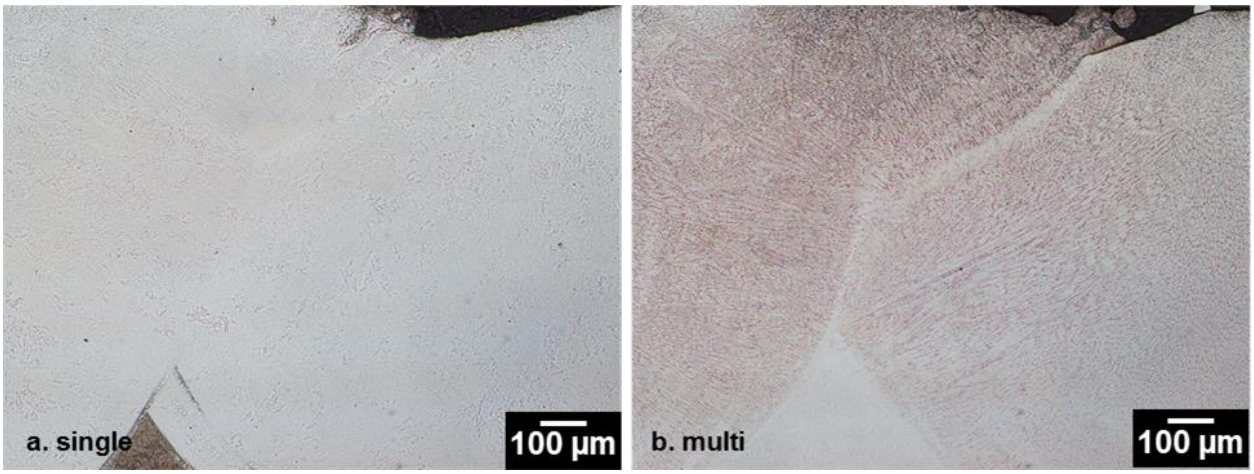

Figure 32 – Microstructures of laser deposited SS 431 between (a) single layer and (b) multi-layers.

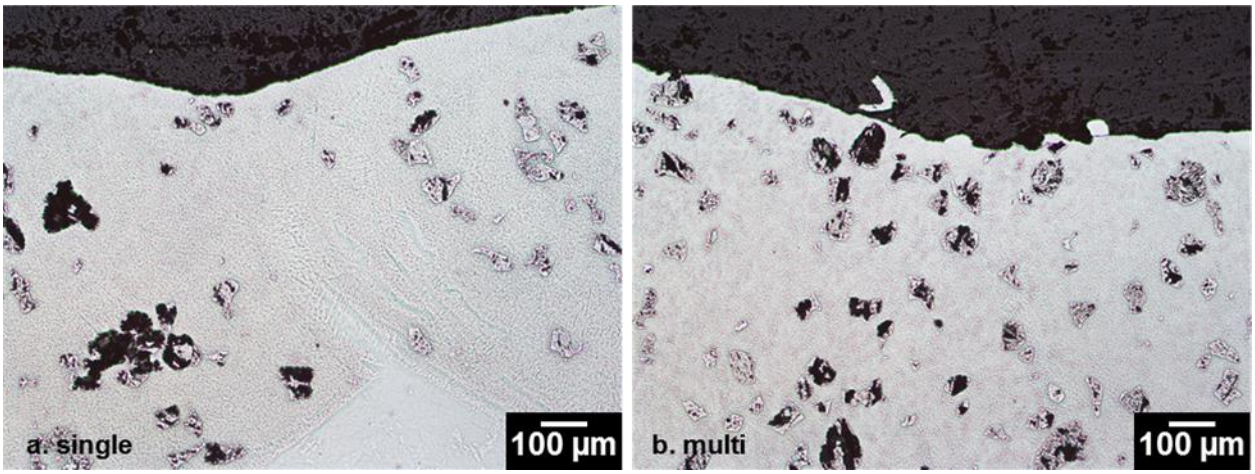

Figure 33 – Microstructures of laser deposited SS 431/ 20% TiC between (a) single layer and (b) multi-layers.

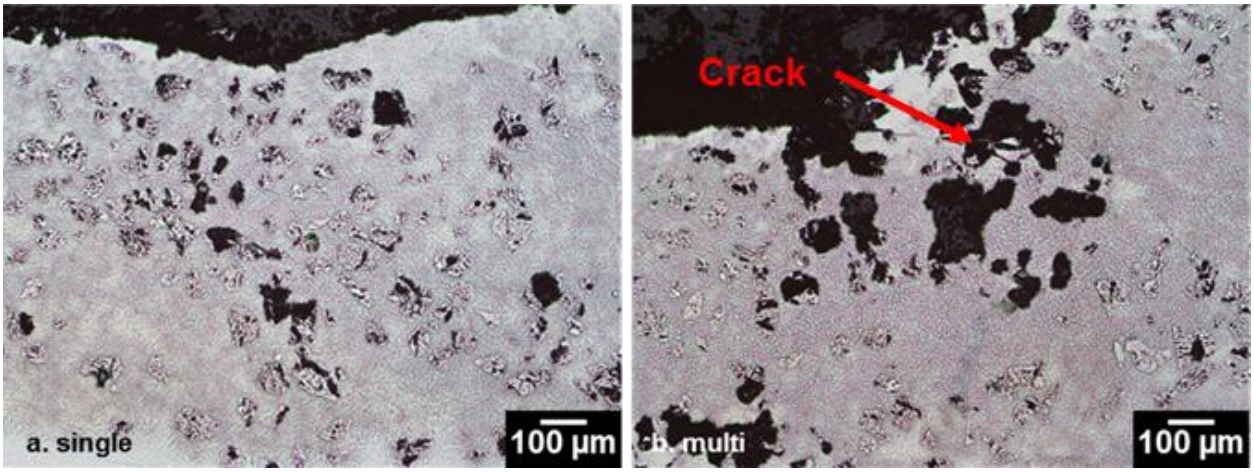

Figure 34 – Microstructures of laser deposited SS 431/ 40% TiC between (a) single layer and (b) multi-layers.

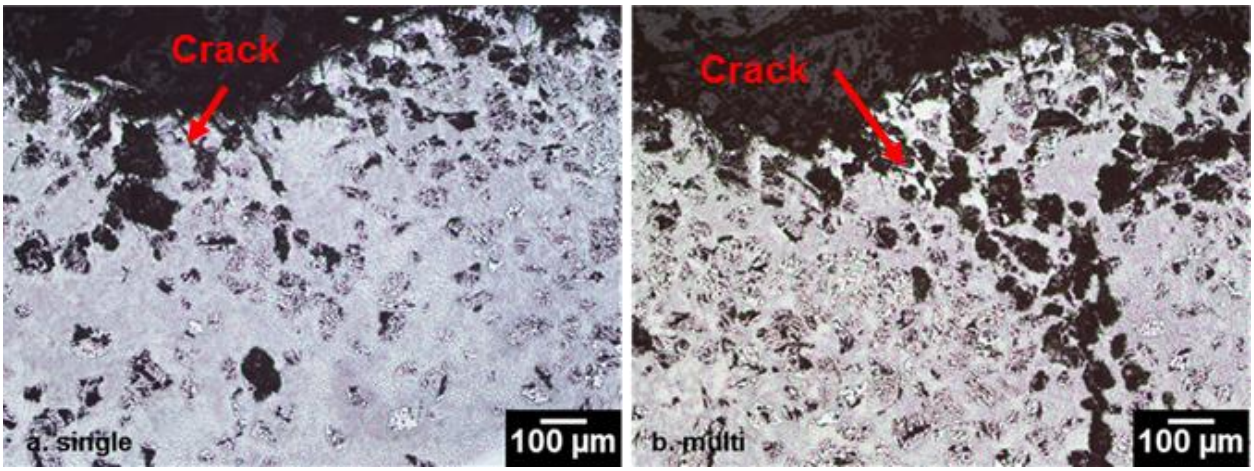

Figure 35 – Microstructures of laser deposited SS 431/ 60% TiC between (a) single layer and (b) multi-layers.

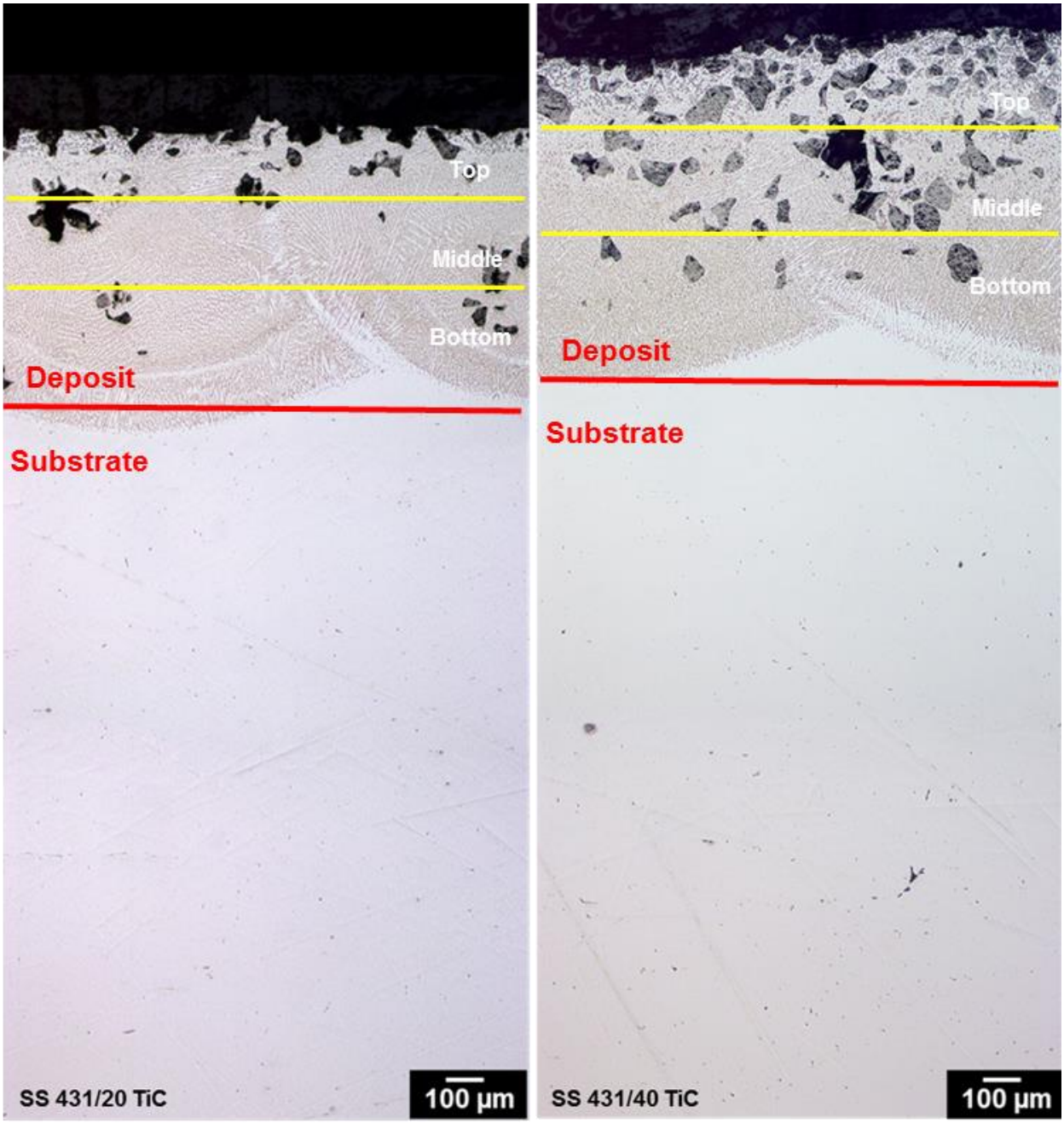

Figure 36 – Microstructure cross-section of each sample with respective deposit, HAZ, and 8620 base material.

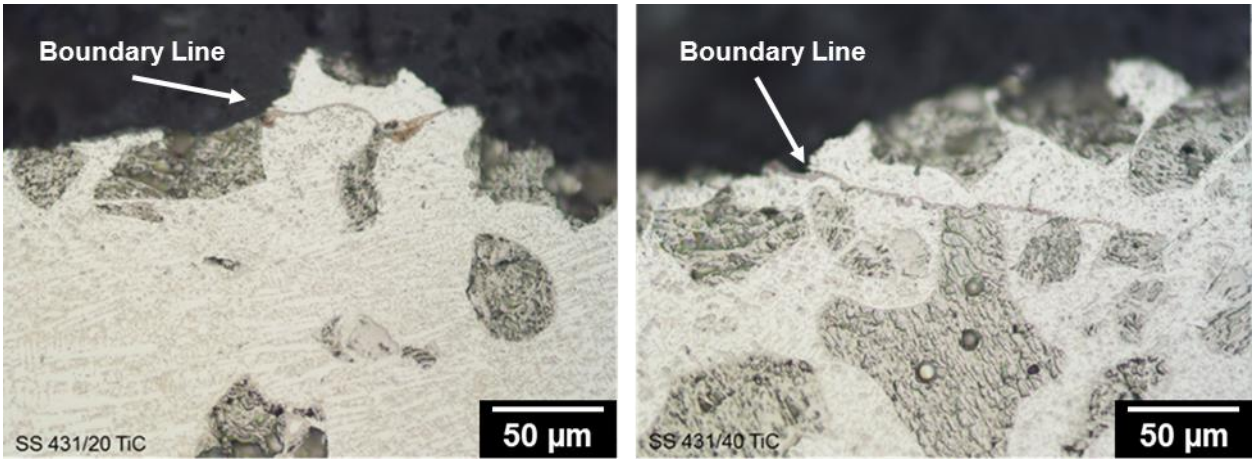

Figure 37 – Boundary lines which appeared in each deposition sample.

4.2.1.2 Test specimens

Microstructural examination was conducted on the RCF test specimen and involved preparation of two samples, a transverse cross-section and a longitudinal cross-section. The transverse sample was cut perpendicular to the laser deposition direction, and the microstructure is shown in Figure 38. The longitudinal sample was cut parallel to the laser deposition direction, and microstructural images for the longitudinal sample are shown in Figure 39.

Microstructural examination was also performed on the four materials deposited onto the Inconel 718® shaft, and these images are shown in Figures 40 to 44. The microstructural images of the Inconel 718® shaft substrate, HAZ, and laser deposited material were obtained at higher magnification and stitched to provide a broad view. Figure 40 represents the cross-section and microstructure of the Inconel 718® shaft. Figures 41 to 44 are cross-sections of deposited materials representing the Inconel 718®, SS 431, SS 431/20 TiC, and SS 431/40 TiC, respectively. The various materials deposited onto the Inconel 718® did not show evidence of cracking. Additionally, the cross-section of the chromium electroplated coating on the shaft is shown in Figure 45. A thin layer of chromium, less than 100 µm, was found on the surface of the Inconel 718® shaft. This material was also used to obtain baseline micro hardness representing the chromium electroplated surface.

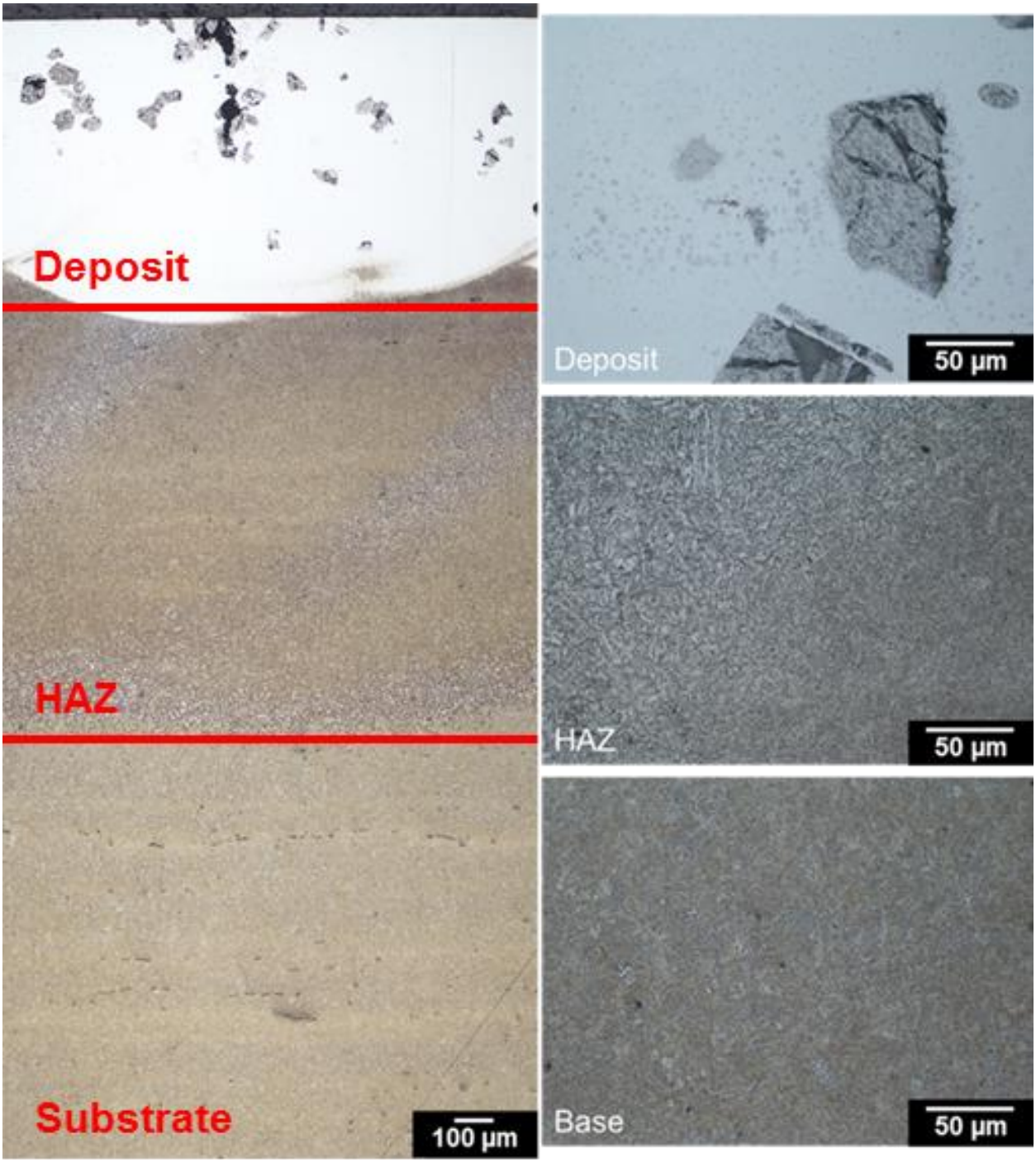

Figure 38 – Microstructures of RCF test specimen with laser deposited SS 431/20 wt% TiC representing transverse cross-section.

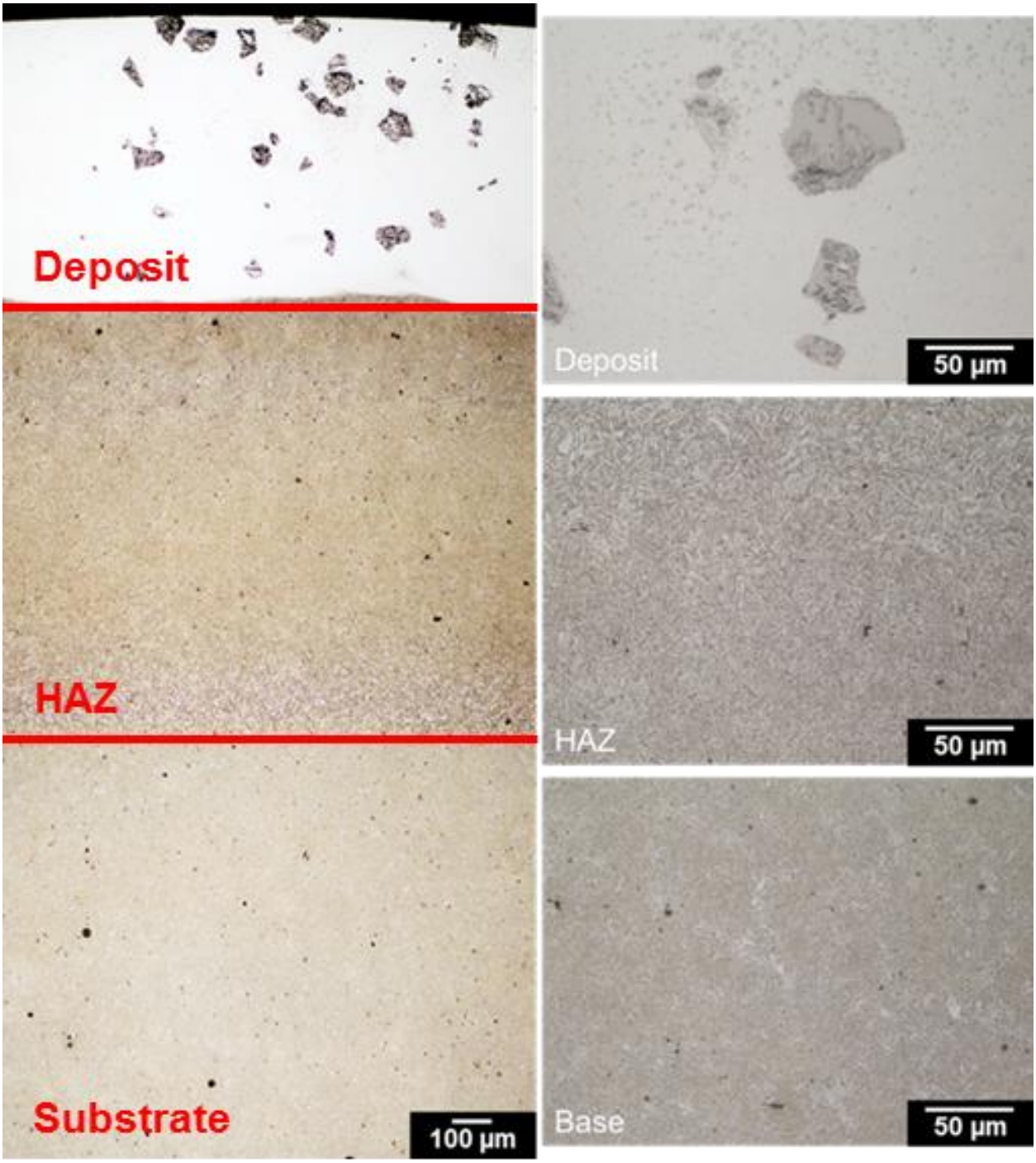

Figure 39 – Microstructures of RCF test specimen with laser deposited SS 431/20 wt% TiC representing longitudinal cross-section.

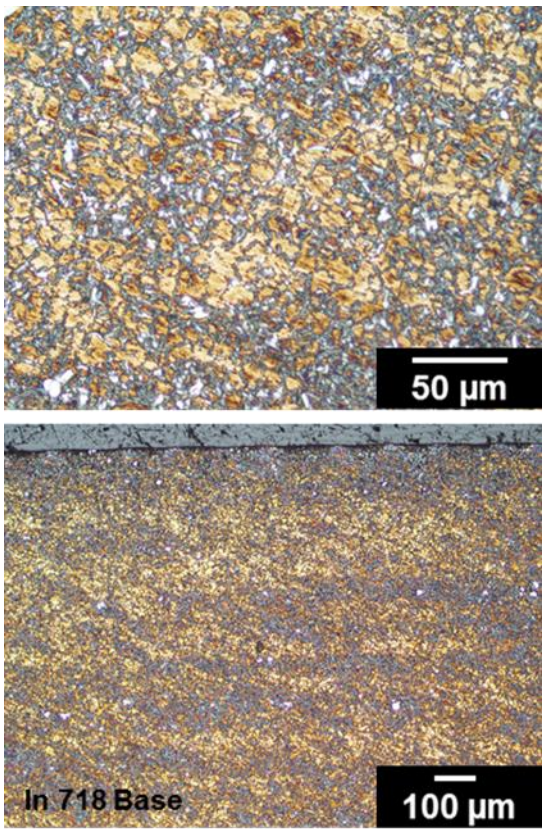

Figure 40 – Microstructures of Inconel 718® shaft.

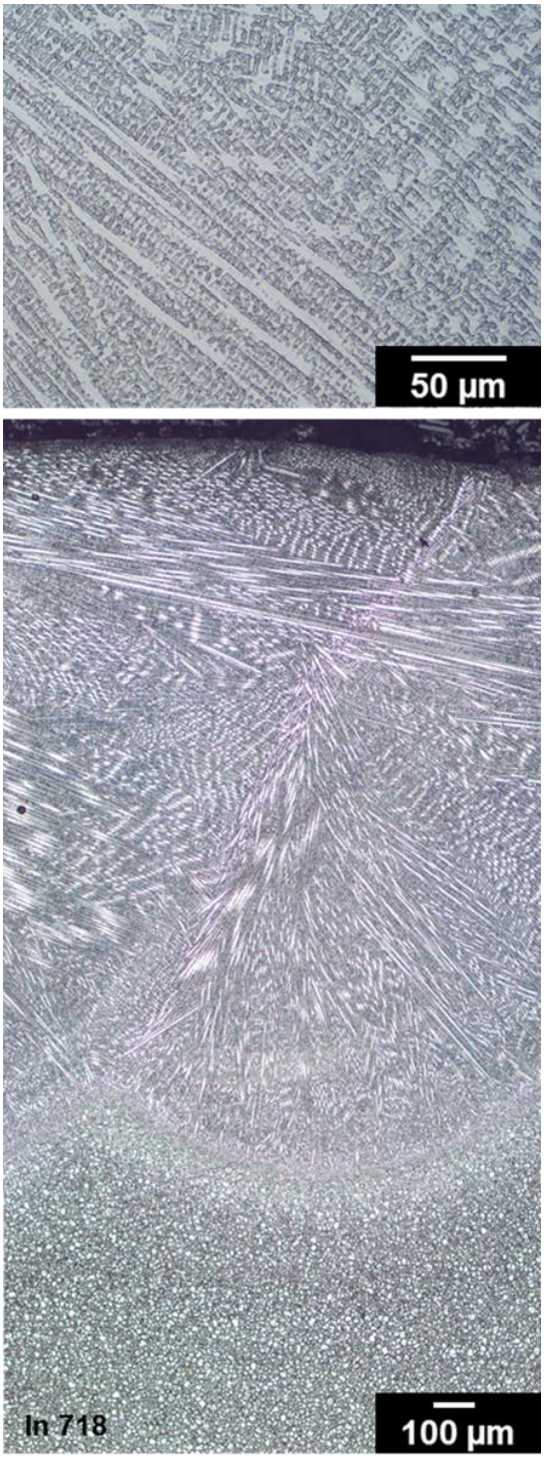

Figure 41 – Microstructures of Inconel 718® deposited on Inconel 718® shaft.

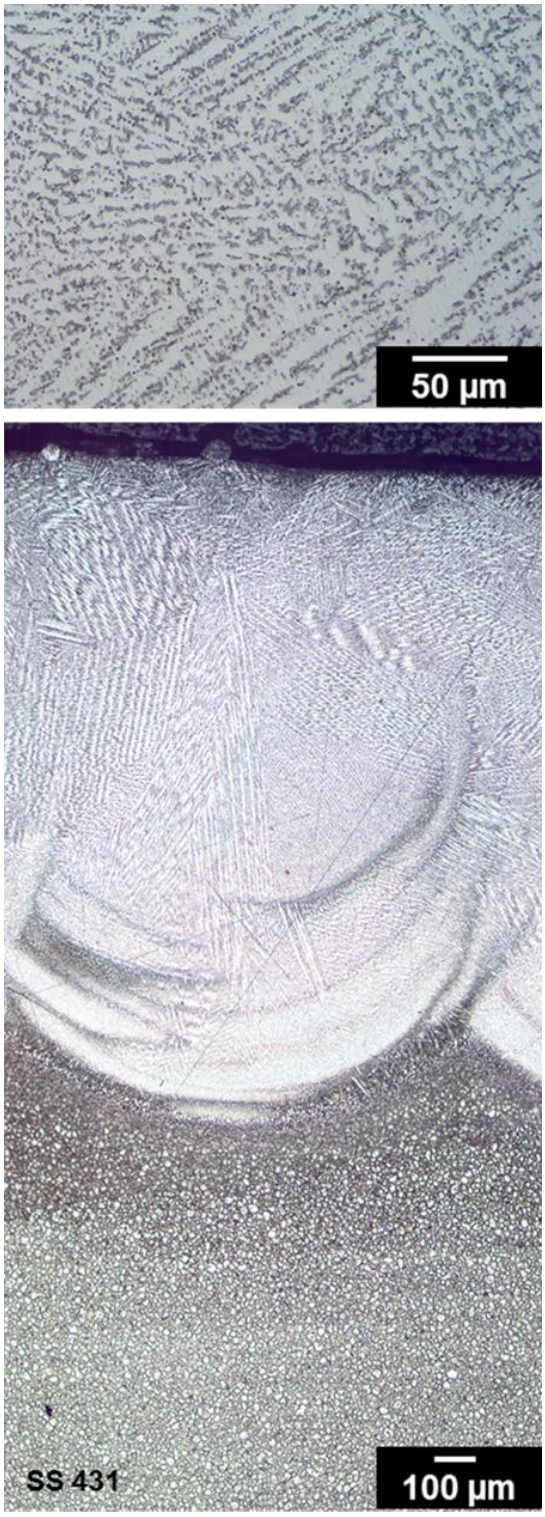

Figure 42 – Microstructures of SS 431 deposited on Inconel 718® shaft.

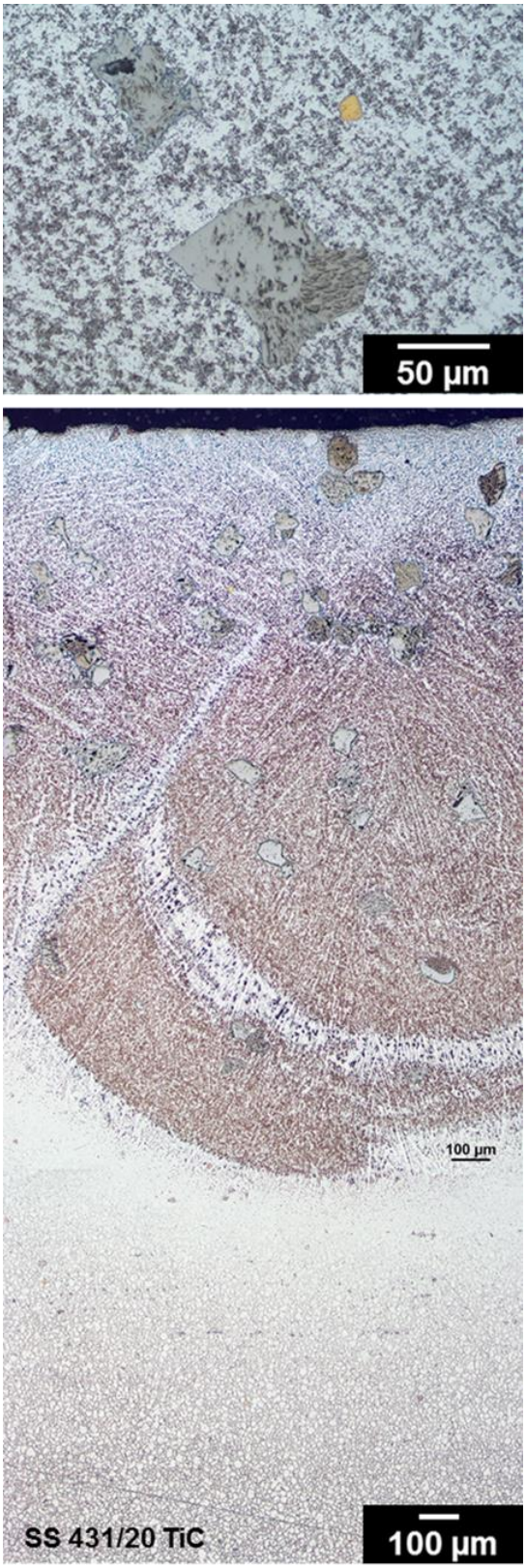

Figure 43 – Microstructures of SS 431/20 TiC deposited on Inconel 718® shaft.

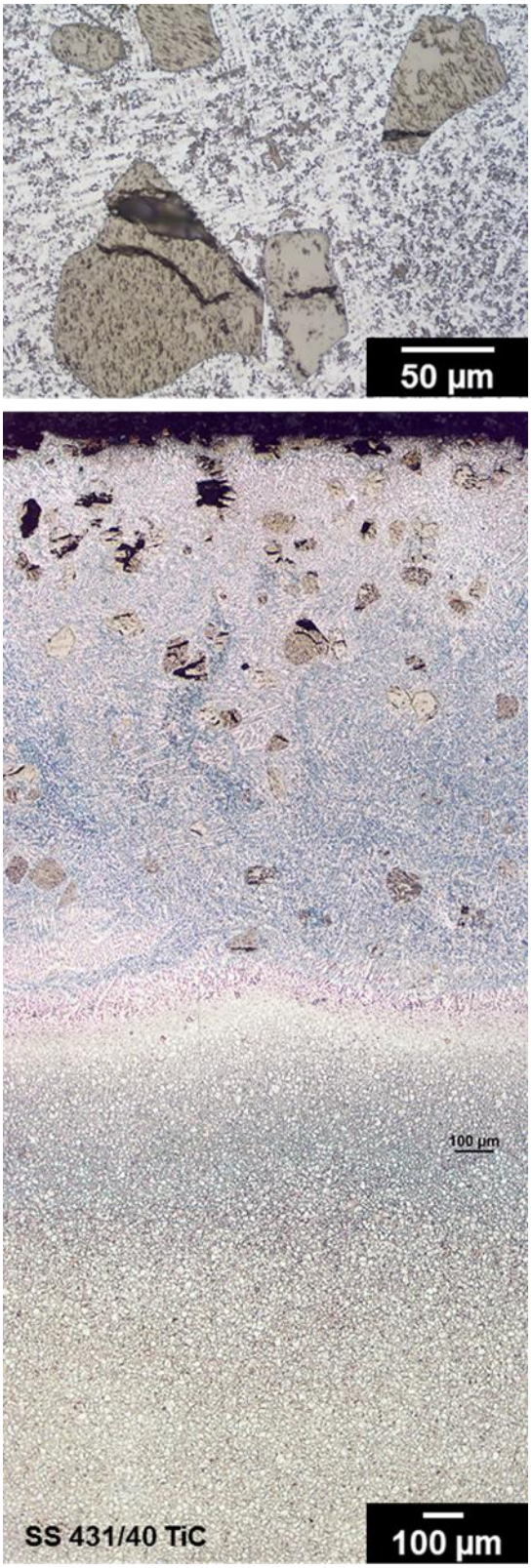

Figure 44 – Microstructures of SS 431/40 TiC deposited on Inconel 718® shaft.

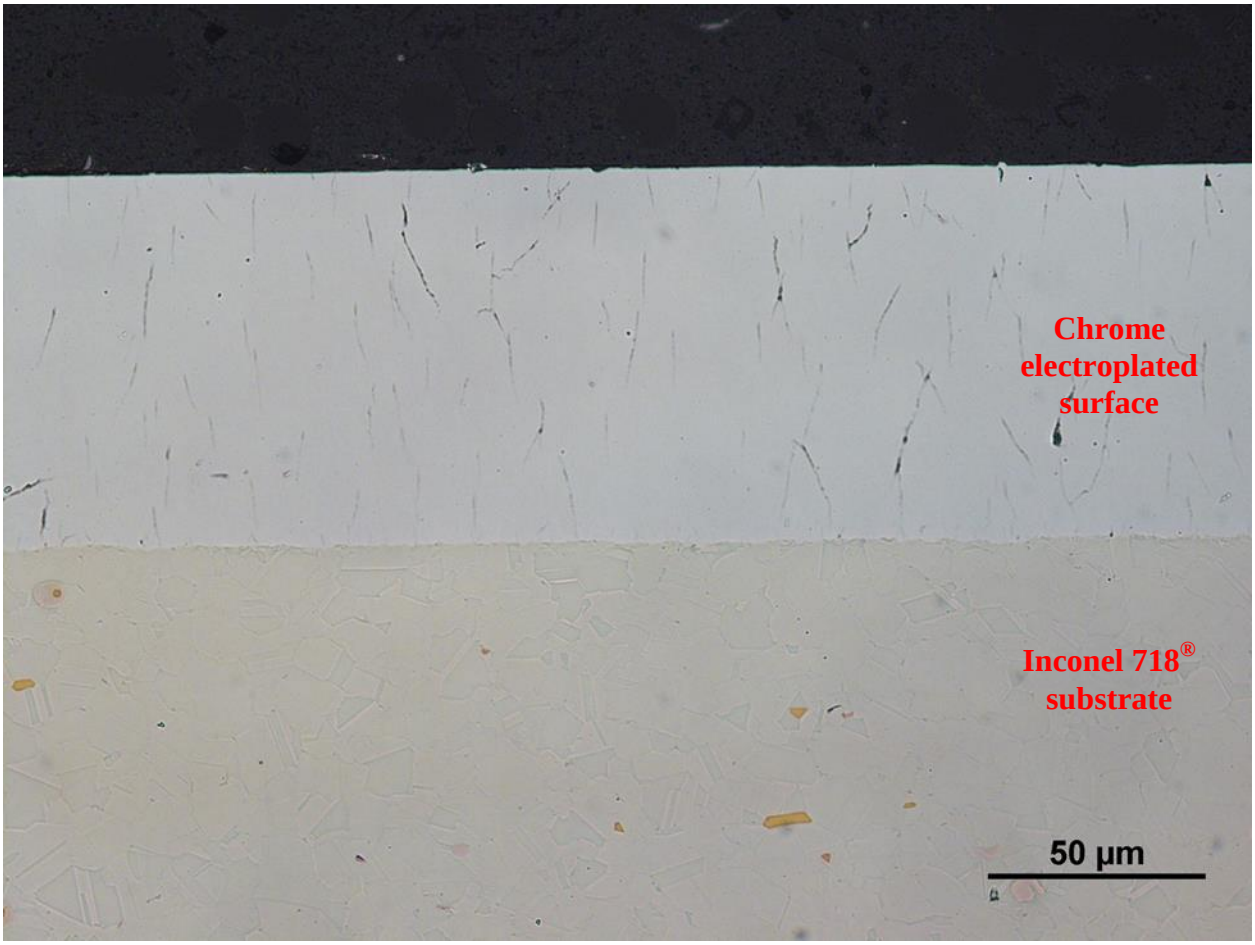

Figure 45 – Microstructural images of Inconel 718® shaft with chrome electroplated surface.

4.2.2 Vickers hardness test

4.2.2.1 *Process development specimens*

Hardness tests were performed using the applicable ASTM-E384 specification with a Leco M-400-G1 hardness tester in the Vickers scale using a 300 g load. The hardness profile of each deposition material on low carbon steel is shown in Figure 46, and the average hardness of the deposit for each sample is shown in Table 12. The hardness profiles indicate that the deposition material hardnesses had been increased by significantly higher TiC concentrations. The hardness also slightly increased, by approximately 25 HV, with multi-layer deposition when compared to the single layers. The localized hardness measurements on the TiC particles were above 2000 HV.

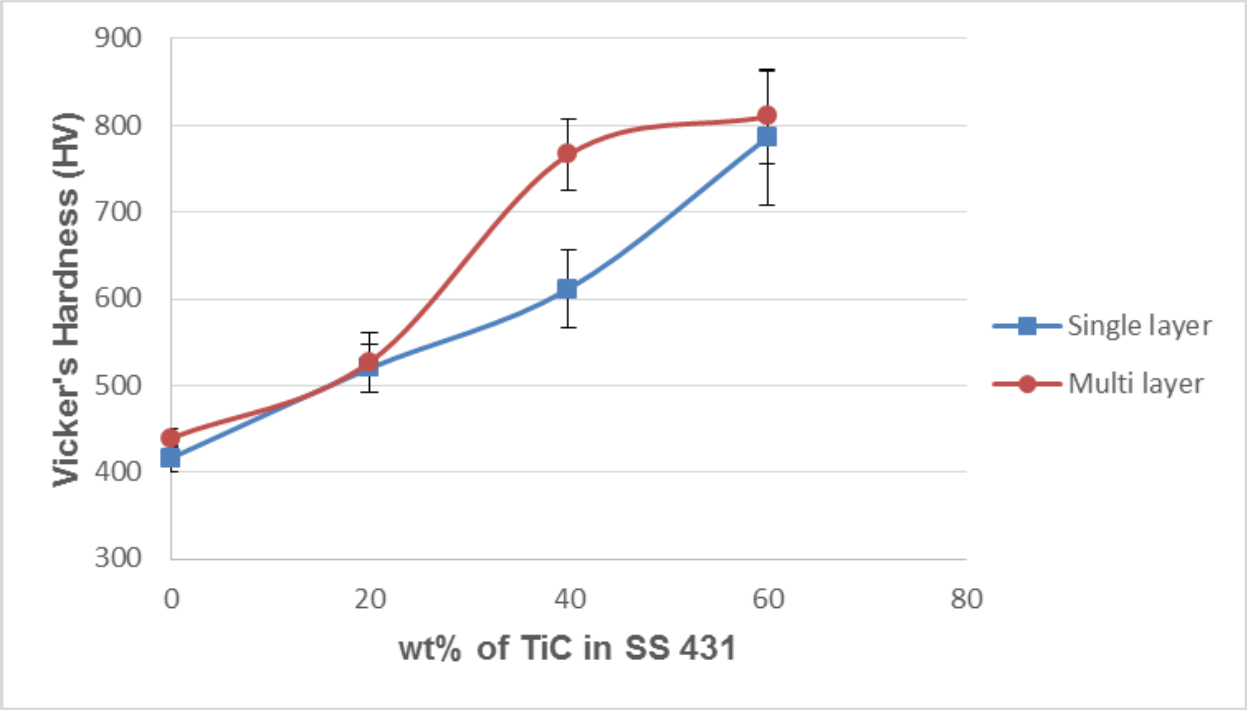

Figure 46 – Hardness of deposits produced using increasing amount of TiC blended in SS 431 powder that had been deposited on low carbon steel.

Table 12 – Vickers hardness of SS 431 and SS 431/TiC composites for single layer and multi-layer depositions.

	SS 431		SS 431/ 20 wt% TiC (28.13 vol% TiC)		SS 431/ 40 wt% TiC (53.07 vol% TiC)		SS 431/ 60 wt% TiC (70.14 vol% TiC)	
Deposit Layers	Single	Multi	Single	Multi	Single	Multi	Single	Multi
Average Vickers Hardness	416	439	520	527	611	766	786	810
Standard Deviation	15.74	10.65	28.50	34.02	45.51	40.27	77.48	54.12

The hardness profiles for the carburized 8620 steel and two selected deposition materials, SS 431/20 TiC and SS 431/40 TiC, are shown in Figure 47. The measured surface hardness of the samples are also shown in Table 13. The hardness profiles indicate that both deposition

materials had achieved higher hardnesses than the carburized 8620 steel. The surface hardness of the carburized 8620 steel was 703 HV. The deposition material SS 431/20 TiC exhibited a hardness of approximately 50 HV above the carburized 8620 steel which was seen to be 746 HV. The hardness of the deposition material representing the SS 431/40 TiC was found to exceed the required hardness by over 100 HV.

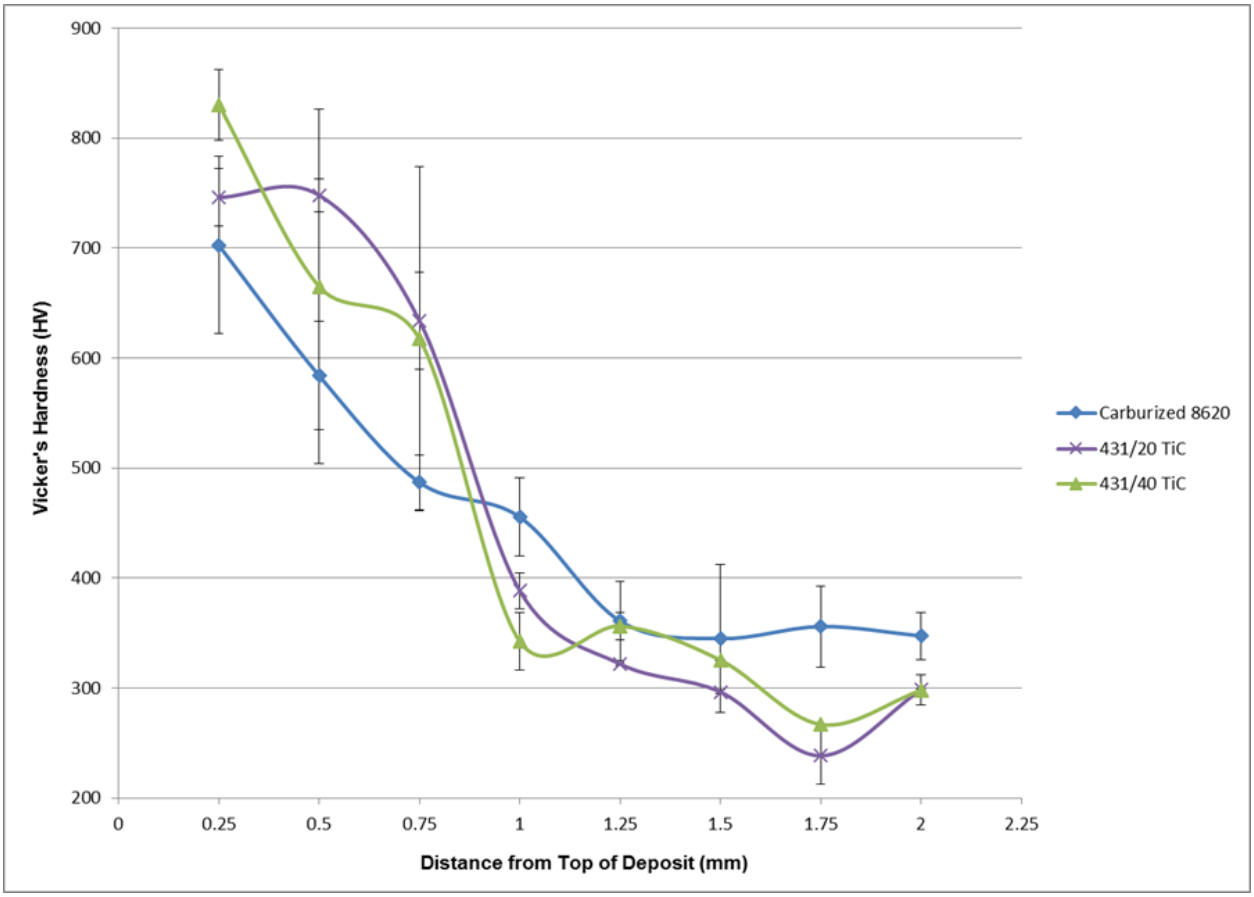

Figure 47 – Hardness profile with four different mixtures of SS 431 and TiC on carburized 8620 steel.

Table 13 – Surface hardness of carburized 8620 steel and two selected deposition materials.

	Carburized 8620 Steel	SS 431/20 TiC	SS 431/40 TiC
Average Vickers Hardness	703	746	830
Standard Deviation	80.5	21.25	142.4

4.2.2.2 *Test specimens*

The micro hardnesses of transverse and longitudinal cross-sections representing the RCF test specimens are shown in Figure 48 and Table 14. Hardness of the HAZ was approximately 290 HV. The non-carburized 8620 steel substrate, representing the carburized surface removed, had a hardness of approximately 320 HV for the transverse and longitudinal cross-sections. However, the deposited material at the transverse cross-section displayed higher hardness of 65 HV. The roller grind surface of the laser deposited RCF specimen had a hardness at 697 HV.

The micro hardness profiles for the deposition materials and the substrate for the Inconel 718® shaft are shown in Figure 49, and the surface hardness of the samples are shown in Table 15. The original Inconel 718® shaft had an average hardness at 442 HV, and the chromium electroplated surface of the shaft had a hardness of 711 HV. All of the deposited materials on Inconel 718® exhibited lower hardness of 400 HV than the chromium electroplated surface. It is believed that dilution of the nickel base material into the deposit was responsible for the lower hardness values. Reducing heat input during the deposition process could possibly minimize the dilution and SS 431 and/or SS 431 with TiC, which could result in higher concentration of the deposition material chemistry and increased hardness for multiple layers.

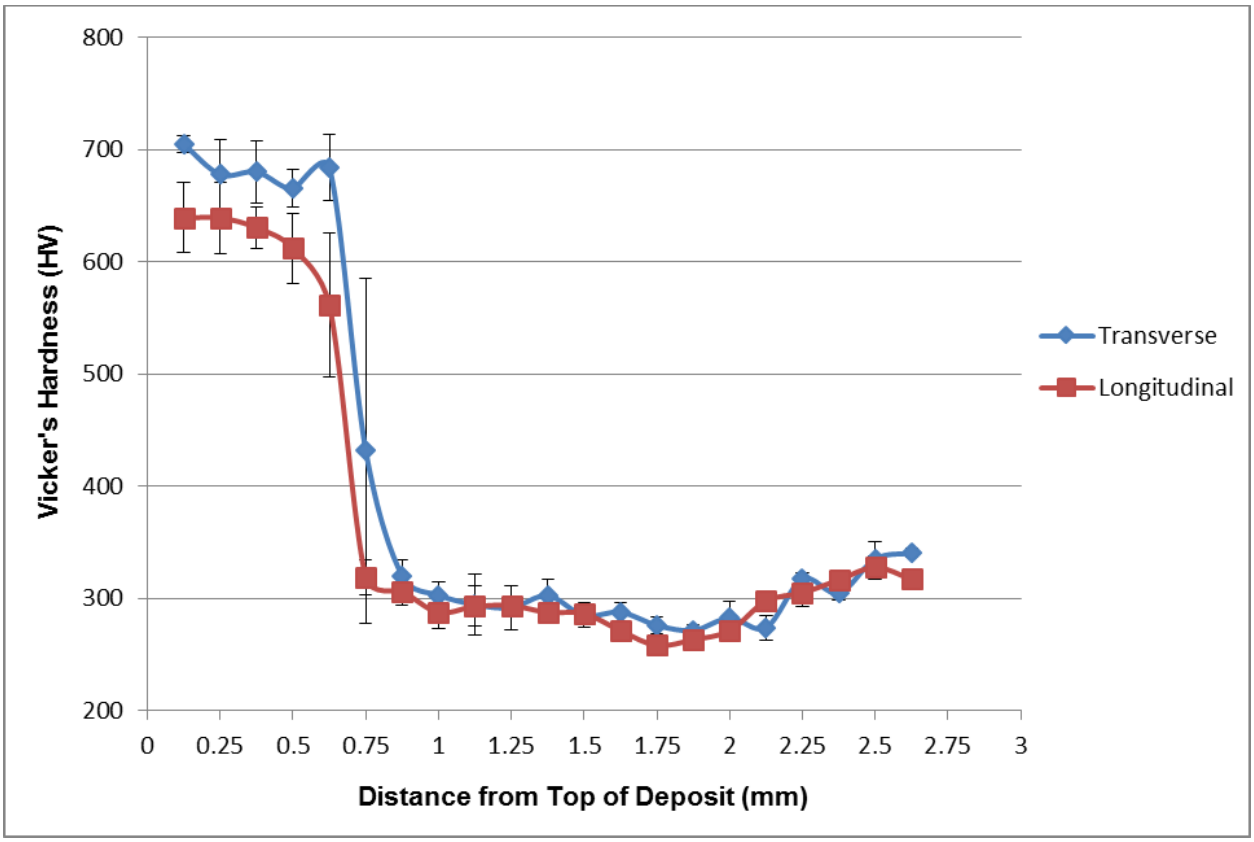

Figure 48 – Hardness profile of SS 431/20 TiC laser deposited on 8620 carburized steel of transverse and longitudinal cross-sections.

Table 14 – Micro hardnesses for SS 431/20 TiC deposit, HAZ, and substrate for the transverse and longitudinal cross-sections.

	SS 431/20 TiC Deposition Materials	HAZ	8620 Steel Substrate
Average Transverse Hardness (HV)	682 (STDEV = 12.81)	290 (STDEV = 13.92)	324 (STDEV = 14.27)
Average Longitudinal Hardness (HV)	616 (STDEV = 29.34)	286 (STDEV = 16.96)	317 (STDEV = 8.05)
Average Surface Hardness (HV)	697 (STDEV = 18.78)	–	–

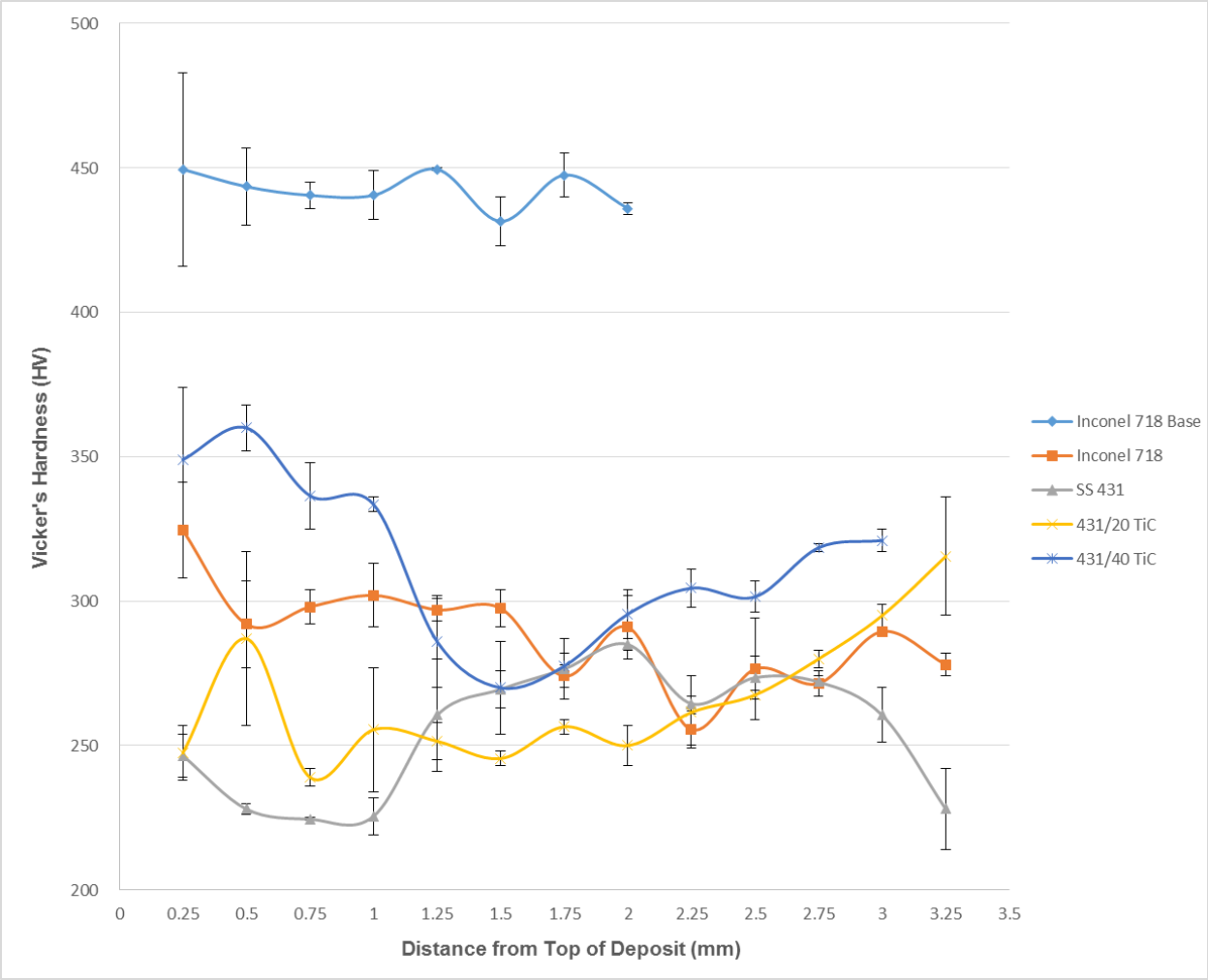

Figure 49 – Hardness of Inconel 718® shaft with deposited materials.

Table 15 – Micro hardnesses of Inconel 718® shaft with deposition materials.

	Inconel 718® Shaft	Inconel 718® Deposit	SS 431 Deposit	SS 431/20 TiC Deposit	SS 431/40 TiC Deposit	Chrome Electroplated
Average Vickers Hardness	442	304	231	257	345	711
Standard Deviation	6.07	12.29	8.97	18.14	10.55	21.47

4.2.3 EDS – mapping analysis of laser deposited SS 431/20 TiC specimen

The cross-section of the SS 431/20 TiC produced for RCF testing was characterized by ESEM and EDS. Figure 50 shows an SEM image of the normalized 8620 steel, which was used by EDS for elemental analysis. Figure 51 shows an SEM image of the HAZ, which was evaluated by EDS for elemental analysis. Figure 52 shows an SEM image of the SS 431/20 TiC that had been deposited. In Figure 52, three locations were chosen for elemental analysis. Location A (white area) represented the SS 431 rich region. Location B (dark dendrite) is believed to be the TiC phase that had precipitated within the SS 431 matrix, and location C represented an unmelted TiC particle. The complete results of the elemental analysis of each region are listed in Table 11.

The SEM image in Figure 52 shows a TiC particle that had been retained within the molten pool, as well as other phases that had been formed during processing. Most notably, the secondary phase apparent at this magnification appear to be dendritic TiC. Figure 53 shows the rich region of individual elements in the composite system. The EDS mapping images also provided evidence that the TiC had dissolved and diffused into SS 431. This is based on the location of titanium (Ti) and iron (Fe) shown in Figure 53. A small amount of vanadium (V), which was observed in the original powder, was also present in the TiC particle. Elemental Ti and V only appeared at unmelted TiC particles and the small dark regions. The elements contained within the SS 431, Fe, Cr, and Ni, remained only in the white areas. The EDS elemental analyses results also showed that the amount of carbon increased in the SS 431 region, as shown in Table 11. The higher carbon within the matrix material would enhance the overall hardness of the matrix. SEM image via back-scattered electrons, Figure 54 and 55 also showed that the TiC particles were dissolved and formed small dendritic constituents near the surface of the TiC particle. The dissolved Ti and C phase that surrounded the original TiC particles are believed to be responsible for the formation of TiC that had reprecipitated during cooling.

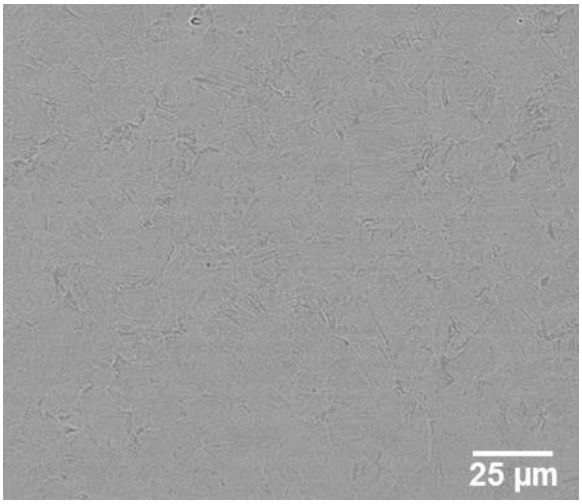

Figure 50 – SEM image of normalized 8620 steel used for substrate.

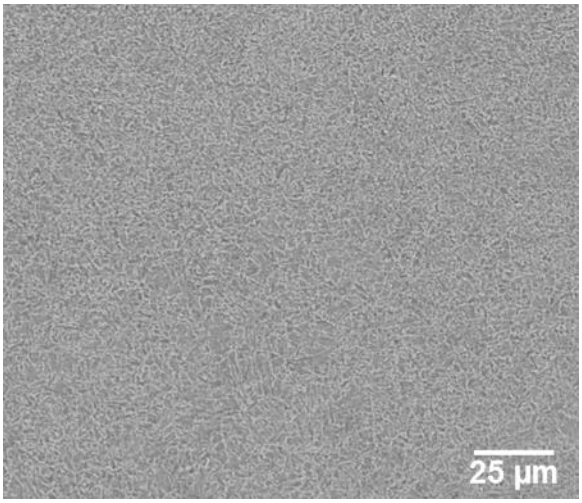

Figure 51 – SEM image of HAZ of substrate used for laser deposition experiment.

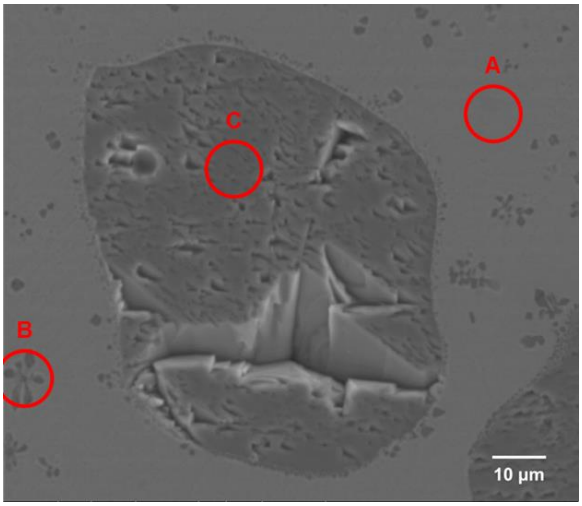

Figure 52 – SEM image of SS 431/20 TiC laser deposited material. Red circles indicate the area characterized by EDS analysis.

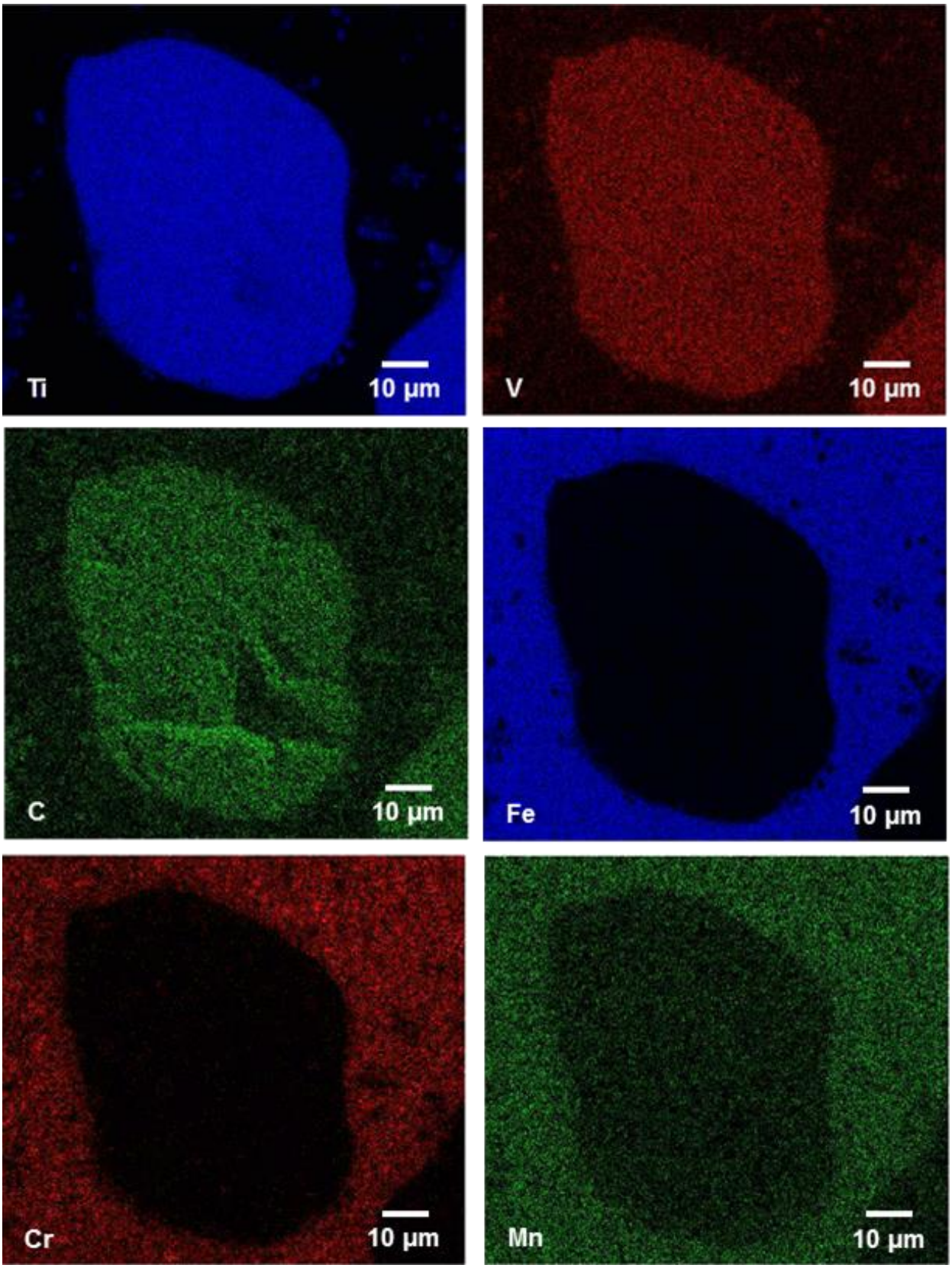

Figure 53 – Images generated by EDS mapping analyzer. Each image shows the respected element located from Figure 52.

Table 16 – EDS elemental analysis results of each region of the RCF testing specimen. The results are also compared to the chemical composition from the reference.

Elements (wt%)	Fe	Cr	Ti	Ni	Mn	V	C	Si	Al	Ca
8620 Base	97.19	0.51	-	0.40	0.67	-	0.88	0.36	-	-
HAZ	96.83	0.59	-	0.47	0.62	-	1.04	0.45	-	-
A. Deposit (White Area)	78.47	10.01	4.58	1.01	0.42	-	3.98	1.26	0.27	-
B. Deposit (Black Dot)	33.76	4.77	47.69	0.37	0.24	0.34	11.51	1.08	-	0.22
C. Deposit (Black Particle)	21.09	2.27	62.26	0.23	-	0.31	13.85	-	-	-
Normalized 8620 steel (ASM Handbook)	96.9-98.02	0.4-0.6	-	0.4-0.7	0.7-0.9	-	0.18-0.23	0.15-0.35	-	-
SS 431	79.17	15.58	-	1.36	0.44	-	2.5	0.4	0.54	-
TiC	-	-	83.81	-	-	0.34	15.85	-	-	-

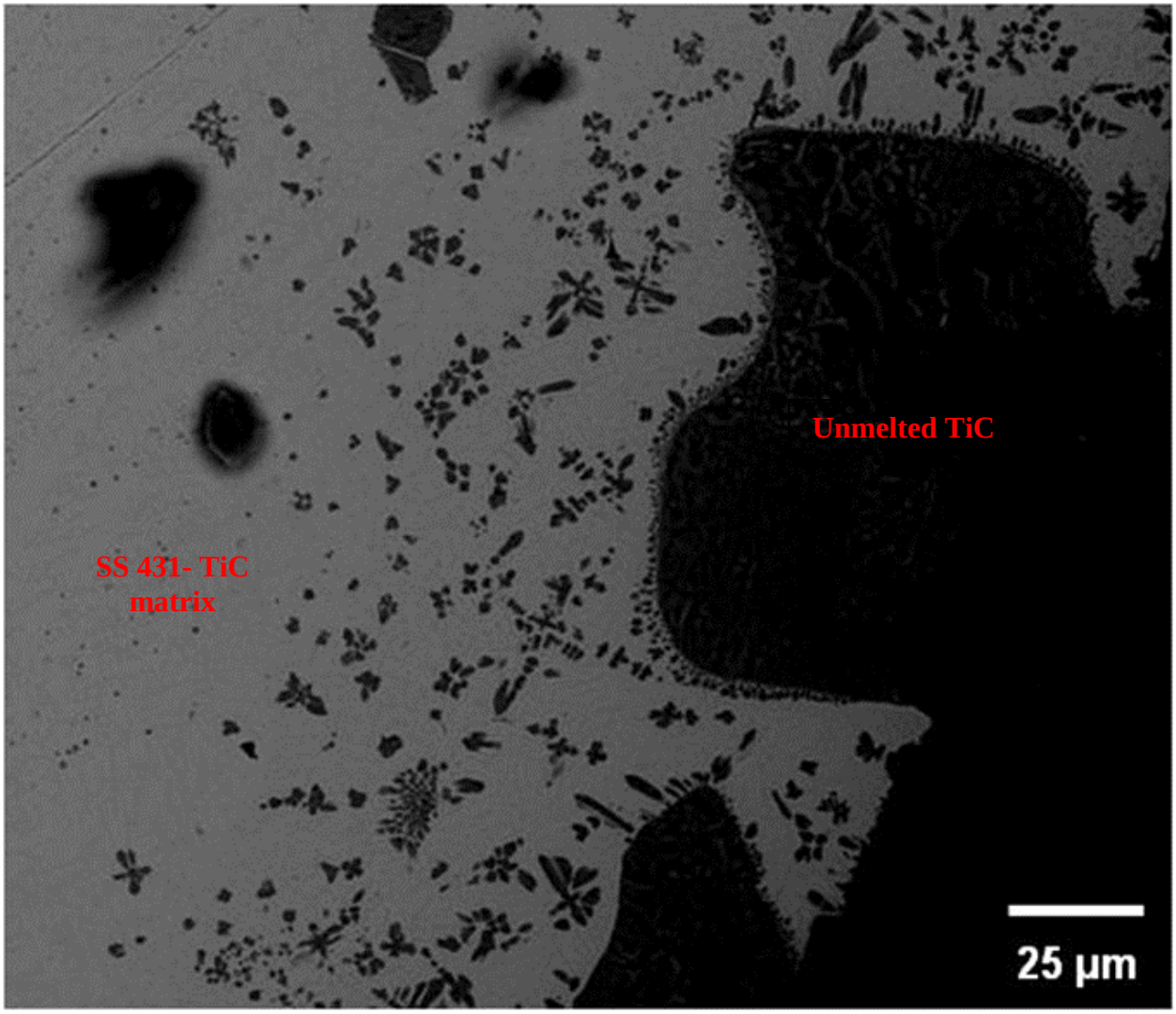

Figure 54 – SEM image showing TiC particles along with precipitates of TiC formed during cooling.

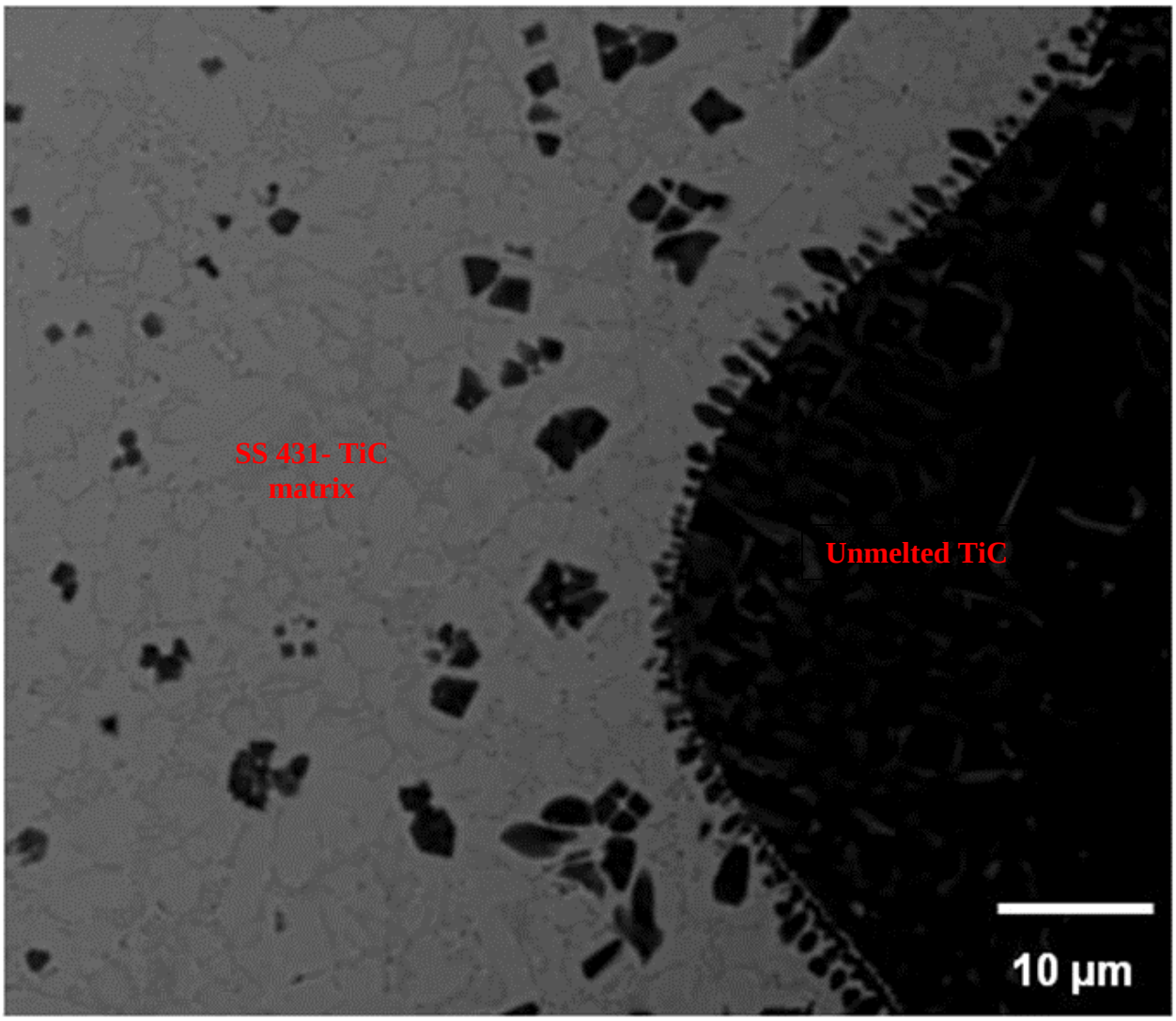

Figure 55 – SEM image showing TiC precipitation.

4.2.4 Rolling contact fatigue test

Three specimens representing the SS 431/20 TiC deposited on carburized 8620 steel were tested by rolling contact fatigue at the Gear Research Institute. Test specimens were contacted against a carburized 8620 steel roller. Tests were conducted at 3000 RPM, and a 2068 MPa (300 ksi) bearing load, with lubricant heated to 70°C (158°F). These testing conditions reflected the exact parameters that were used previously during RCF testing of carburized 8620 steel.

Comparable testing results are shown in Table 17. The results of the SS 431/20 TiC samples showed an average of 98.8 hours of lifetime (17,300,000 cycles), and all specimens failed with surface scuffing on both the specimen and roller. The surface scuffing failure of the SS 431/20 TiC specimen is shown in Figure 56. Surface scuffing occurs when both surfaces of the test specimen and test roller exhibit wear. This condition is shown as Figure 57 and results in an increased surface contact area during RCF testing. The increased contact area reduces the stress load on the test specimen, and affects both the RCF test result and service life of the test specimen. Test 3, which represented the SS 431/20 TiC specimen, failed with surface pitting, which is illustrated in Figure 58. The surface pitting failure is usually caused by internal voids or cracks within the test specimen. Figure 58 appears to indicate that the pitting occurred at the interface of the deposited material and the 8620 steel substrate. This could be due to lack of fusion occurring at the deposit and substrate interface during the laser deposition process.

A Weibull plot representing the SS 431/20 TiC specimens and the prior results for the carburized 8620 steel specimens tested under rolling contact fatigue is shown in Figure 59. The SS 431/20 TiC specimens have a R^2 value at 0.96 and the Weibull equation is show in Equation 5. The carburized 8620 steel specimens have a R^2 value at 0.97 and the Weibull equation is show as Equation 6.

$$y = 4.9772x - 23.727 \quad \text{Eq. (5)}$$

$$y = 2.8317x - 14.612 \quad \text{Eq. (6)}$$

The high Weibull modulus reflected in the 431/20 TiC material had the similar wear failure time from surface scuffing. The carburized 8620 steel failed at the middle of the contact region after more than 150 hours, averaging 27,000,000 cycles. Figure 60 is a photograph of the carburized 8620 steel specimen, representing the surface pitting failure and without surface scuffing.

The surface scuffing occurred on both the SS 431/20 TiC specimen and the carburized 8620 steel roller; this is believed due to the extreme high hardness of the unmelted TiC particles on the surface of the specimens. Surface finish measurement were also conducted on the RCF testing rollers and SS 431/20 TiC specimens. Figure 61 represents the surface finish of carburized 8620 steel roller for RCF Test 2 and shows a relatively smooth curved surface of the testing roller. As the roller was worn, the measured curve became uneven, which is shown as Figure 62. The SS 431/20 TiC specimen from Test 2 also exhibited a worn surface due to surface scuffing, and this is illustrated in Figure 63.

There are several explanations for the surface scuffing observed on the specimen and roller. Because the SS 431-TiC composite structure is softer than the undissolved TiC particles, the SS 431 matrix material could experience local wear causing detachment of the TiC particles which remained on the uneven surface of RCF specimen. The high hardness of the TiC particles would promote wear on the surface of the carburized steel roller. Another explanation is that the granular morphology of the TiC particles promoted wear on both the test specimen and the roller. Detailed results of the surface roughness for the RCF test specimen are shown in next section, “Results of Tribology Analysis”.

Table 17 – Rolling contact fatigue testing of SS 431/20 TiC and reference carburized 8620 steel.

Test #	Substrate	Coating	Load (N)	Speed (RPM)	Lifetime (Hours)	Cycles ($x10^6$)	Observation
SS 431/20 TiC Deposited on Carburized 8620 Steel							
1	8620	SS 431/20 TiC	5720	2915	96.2	16.83	Wear Failure, Surface scuffing on both specimen and roller
2	8620	SS 431/20 TiC	5720	2915	80.6	14.10	Wear Failure, Surface scuffing on both specimen and roller
3	8620	SS 431/20 TiC	5720	2915	119.7	20.94	Surface Origin Pitting, Surface scuffing on both specimen and roller
				Average	98.8	17.29	
Carburized 8620 Steel							
1	8620	8620	5556	2922	135.4	23.74	Surface Origin Pitting
2	8620	8620	5556	2922	188.1	32.98	Surface Origin Pitting
3	8620	8620	5556	2919	84.2	14.75	Surface Origin Pitting
4	8620	8620	5556	2925	207.9	36.49	Surface Origin Pitting
				Average	153.9	26.99	

Figure 56 – RCF test results showing scuffing surface on the SS 431/20 TiC.

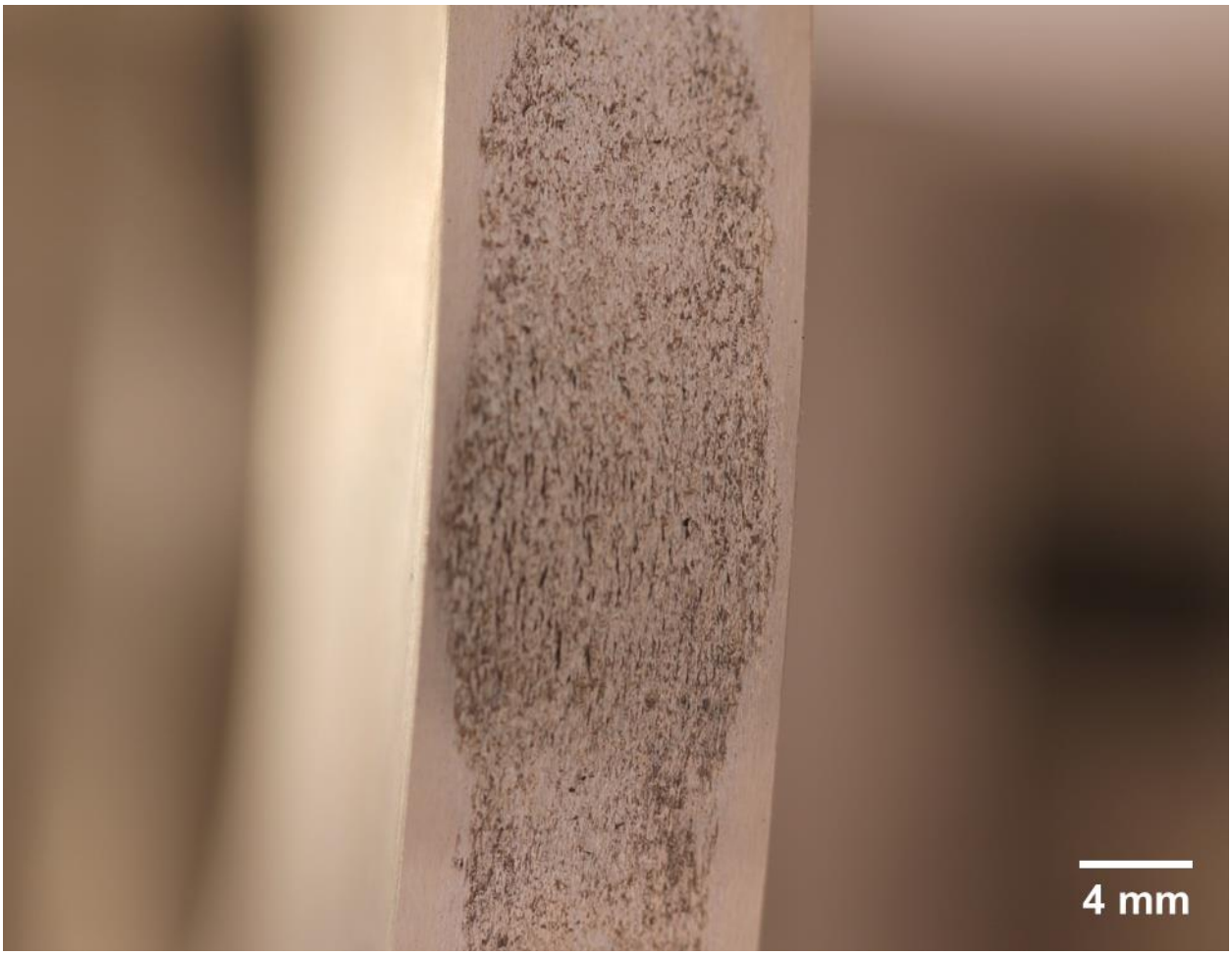

Figure 57 – RCF test results showing scuffing surface on the carburized 8620 steel roller.

Figure 58 – RCF test results showing surface pitting on the SS 431/20 TiC specimen.

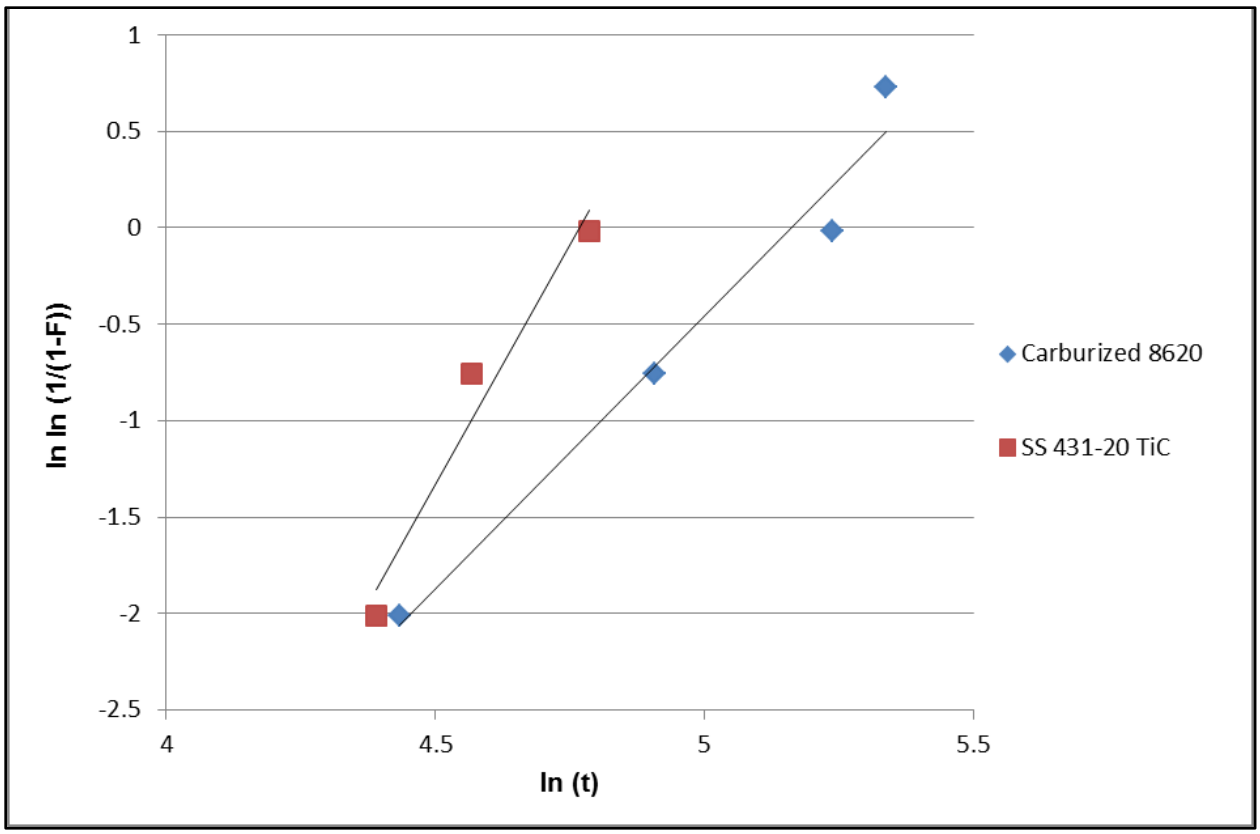

Figure 59 – Weibull plot of rolling contact fatigue life time for the carburized 8620 steel and laser deposited SS 431/20 TiC.

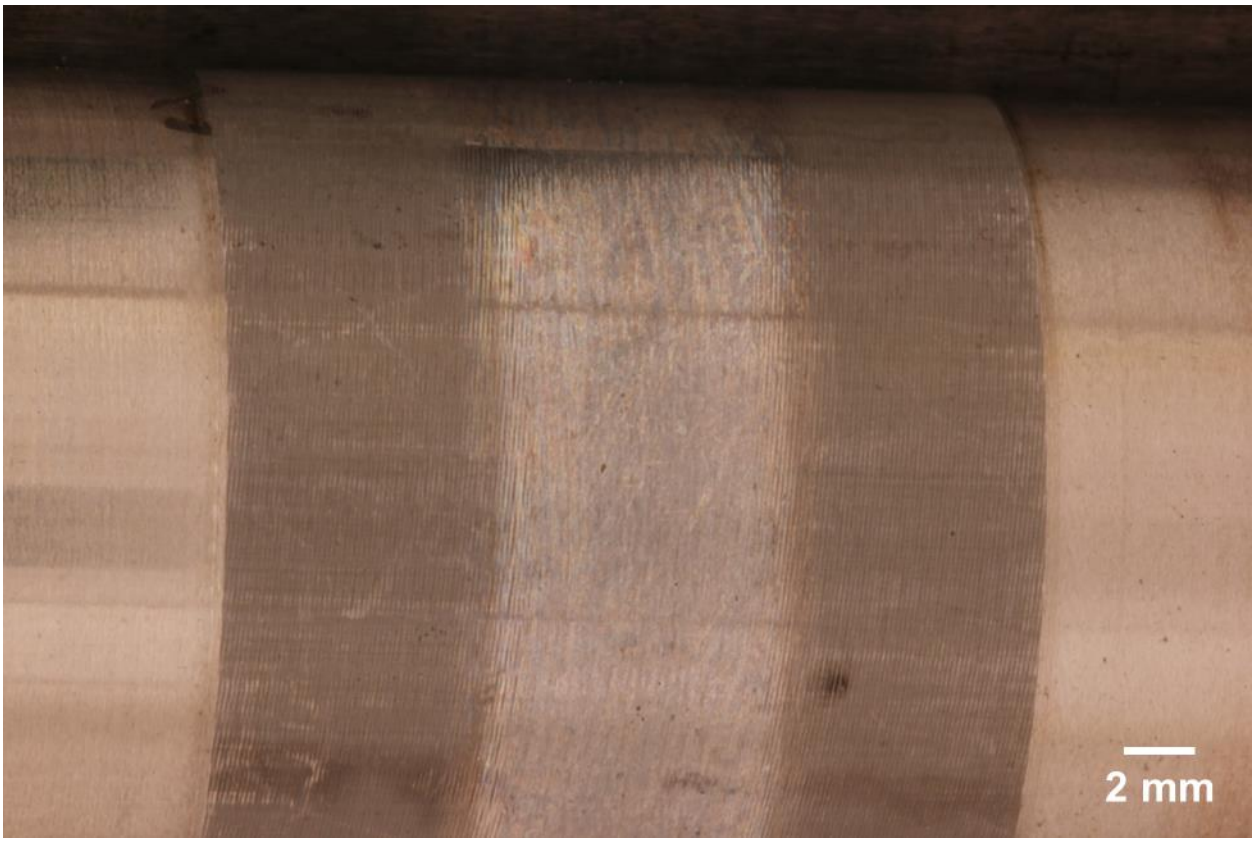

Figure 60 – RCF results of the carburized 8620 steel specimen without scuffing surface.

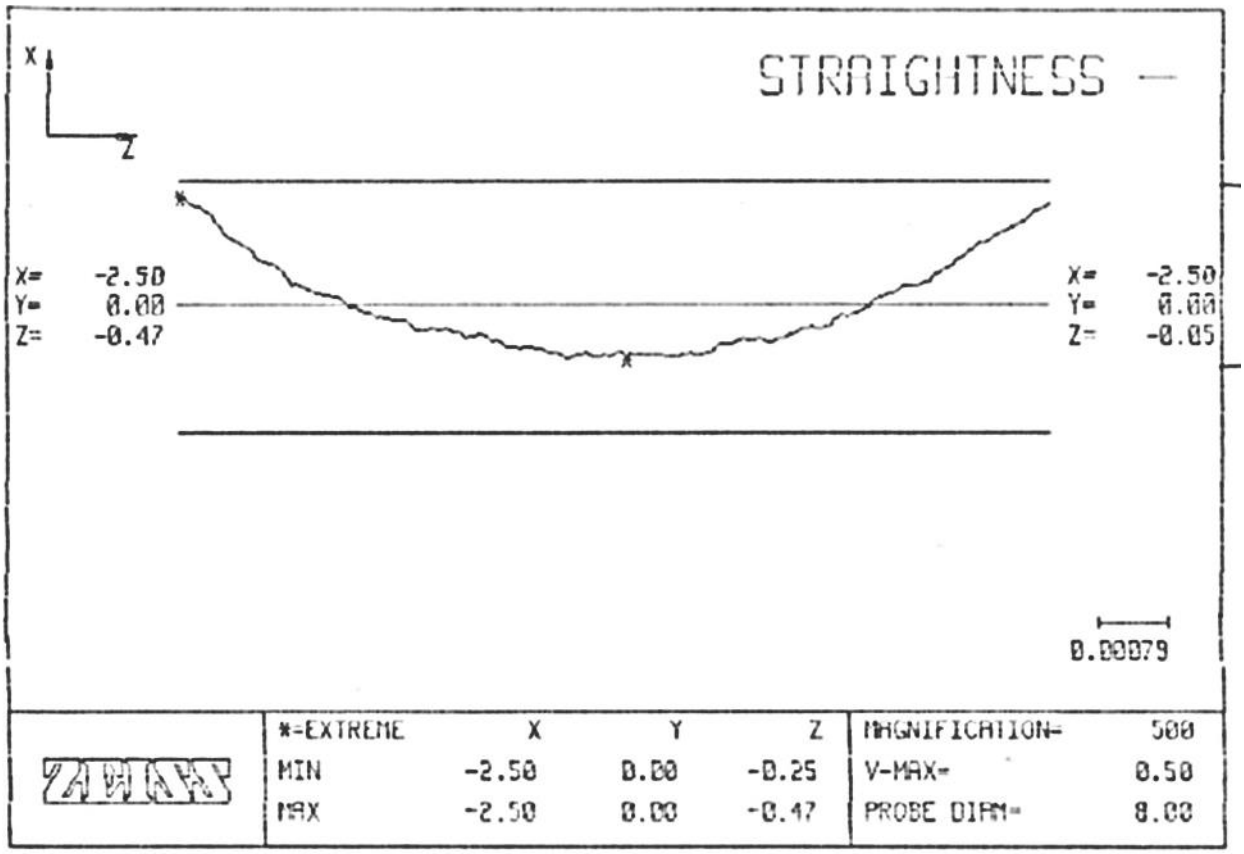

Figure 61 – Tribology analysis results of carburized 8620 steel roller before RCF testing.

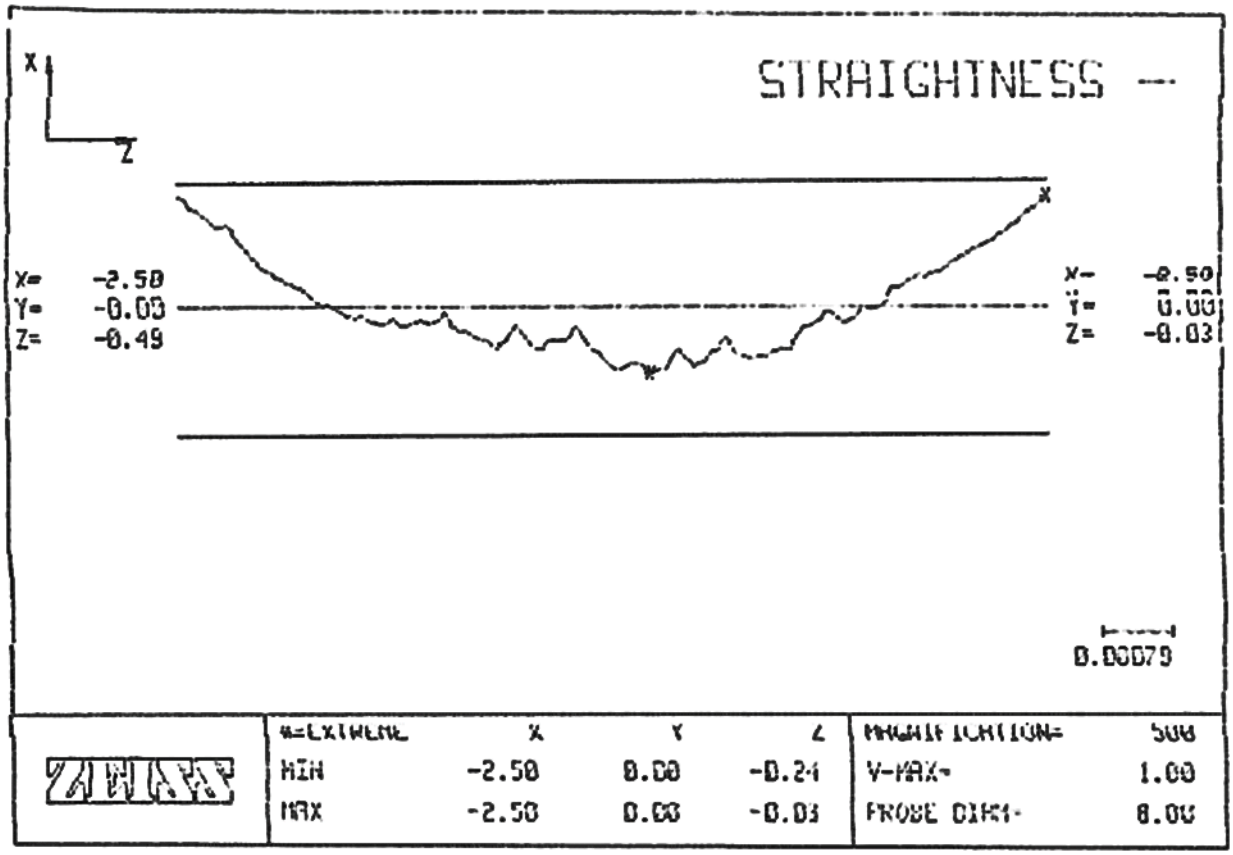

Figure 62 – Tribology analysis results of carburized 8620 steel roller after RCF testing.

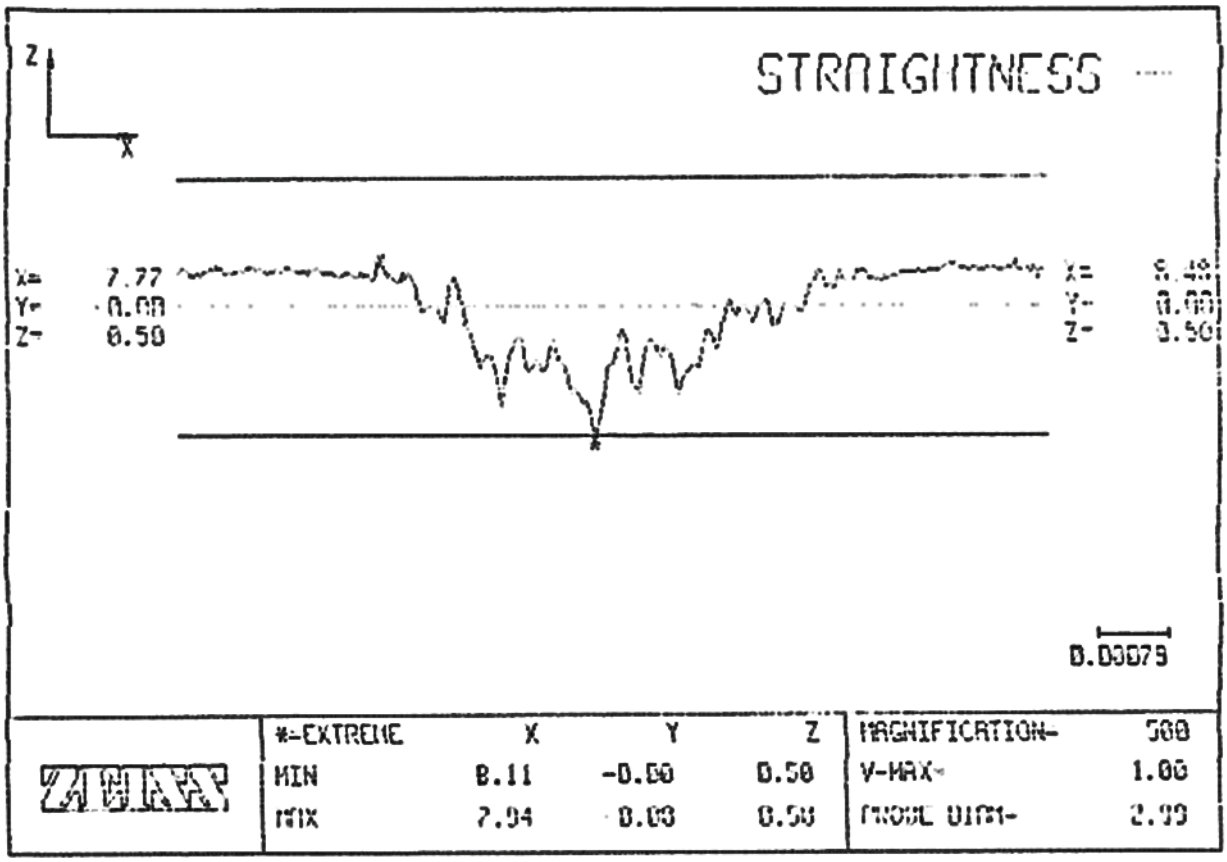

Figure 63 – Tribology analysis results of SS 431/20 TiC deposit material after RCF testing.

4.2.5 Tribology analysis

A Zygo NewView 7300 optical profilometer was used for tribology characterization and surface roughness analysis. The surface roughness was measured with both the carburized 8620 steel RCF specimen and the laser deposited SS 431/20 TiC RCF specimen. Measurement was also conducted on the Inconel 718® shaft and the four materials that had been laser deposited onto the shaft: Inconel 718®, SS 431, SS 431/20 TiC, and SS 431/40TiC.

The results of the surface roughness measurements on the carburized 8620 steel RCF specimen and the laser deposited SS 431/20 TiC RCF specimen are shown in Table 18. Individual surface roughness maps are also shown in Figures 64 to 66. The roughness measurements showed the surface of the SS 431/20 TiC deposit could meet the smoothness requirement dictated by the application for a bearing surface. However, Figure 66 represents a portion of the surface area of the SS 431/20 TiC deposit that exhibits pores on the surface, with resulted in a slightly rougher surface than the results from Figure 65. The microstructural SEM image representing the cross-section is shown in Figures 67 and 68. Both microstructure and SEM images show the pores may be related to ejection of the original TiC particles. This is believed to be caused by removal of the TiC particles during yielding of the adjacent matrix material during cyclic loading of the roller grinding process. The morphology of the TiC particles could contribute to the uneven surface on the SS 431/20 TiC deposit and the surface scuffing during RCF testing.

The Inconel 718® shaft and the four different laser deposited materials on the Inconel 718® shaft were also analyzed using the Zygo optical profilometer for surface roughness. The results for Inconel 718® samples are shown in Table 19, individual surface roughness maps are also shown in Figures 69 to 73. The Ra values for all of the deposit materials are larger than that defined for the application. The results also indicated a much rougher surface was produced with the deposited materials than the carburized 8620 steel. This data are shown in Table 13. It is believed that the surface roughness obtained after machining was related to the hardness of materials. The softer materials were more easily scratched by small particles that were removed during machining and resulted in a rougher surface finish. The hardness of the Inconel 718® and the deposited materials on the Inconel 718® shaft were much softer than the carburized 8620 steel and the SS 431/20 TiC deposited on the carburized 8620 steel. The

comparison of surface roughness with the respected hardness results are shown in Table 15. This data shows a correlation between higher hardness and lower Ra value, or a smoother surface.

Table 18 – Surface roughness of the RCF test specimens.

	Baseline Carburized 8620 Steel	SS 431/20 TiC on Carburized 8620 Steel	SS 431/20 TiC on Carburized 8620 Steel (with defects)
Avg. Ra (μm)	0.848	0.171	0.193
Areal Ra (μm)	0.856	0.183	0.193

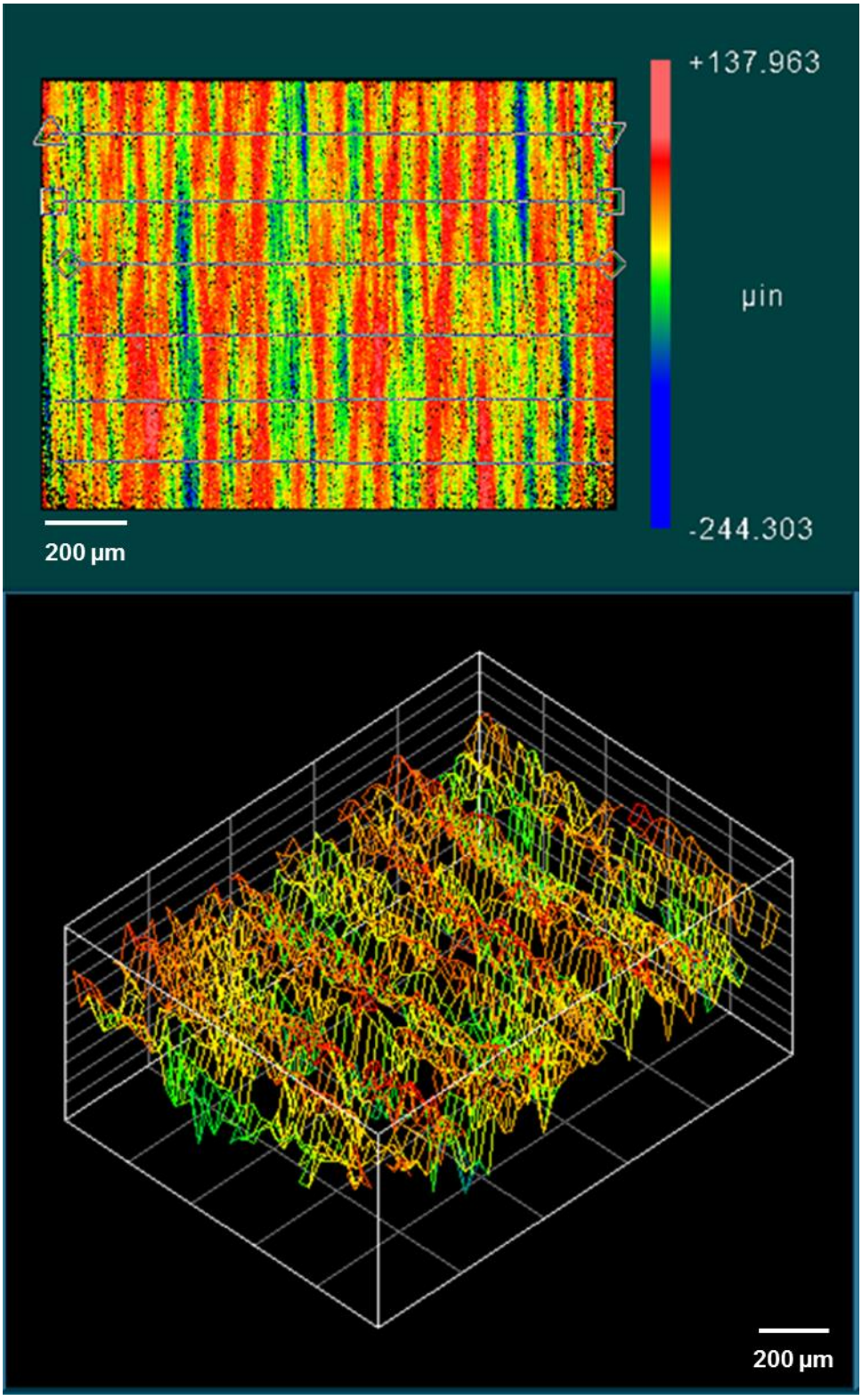

Figure 64 – Optical profilometry of the baseline carburized 8620 steel specimen used in the RCF test.

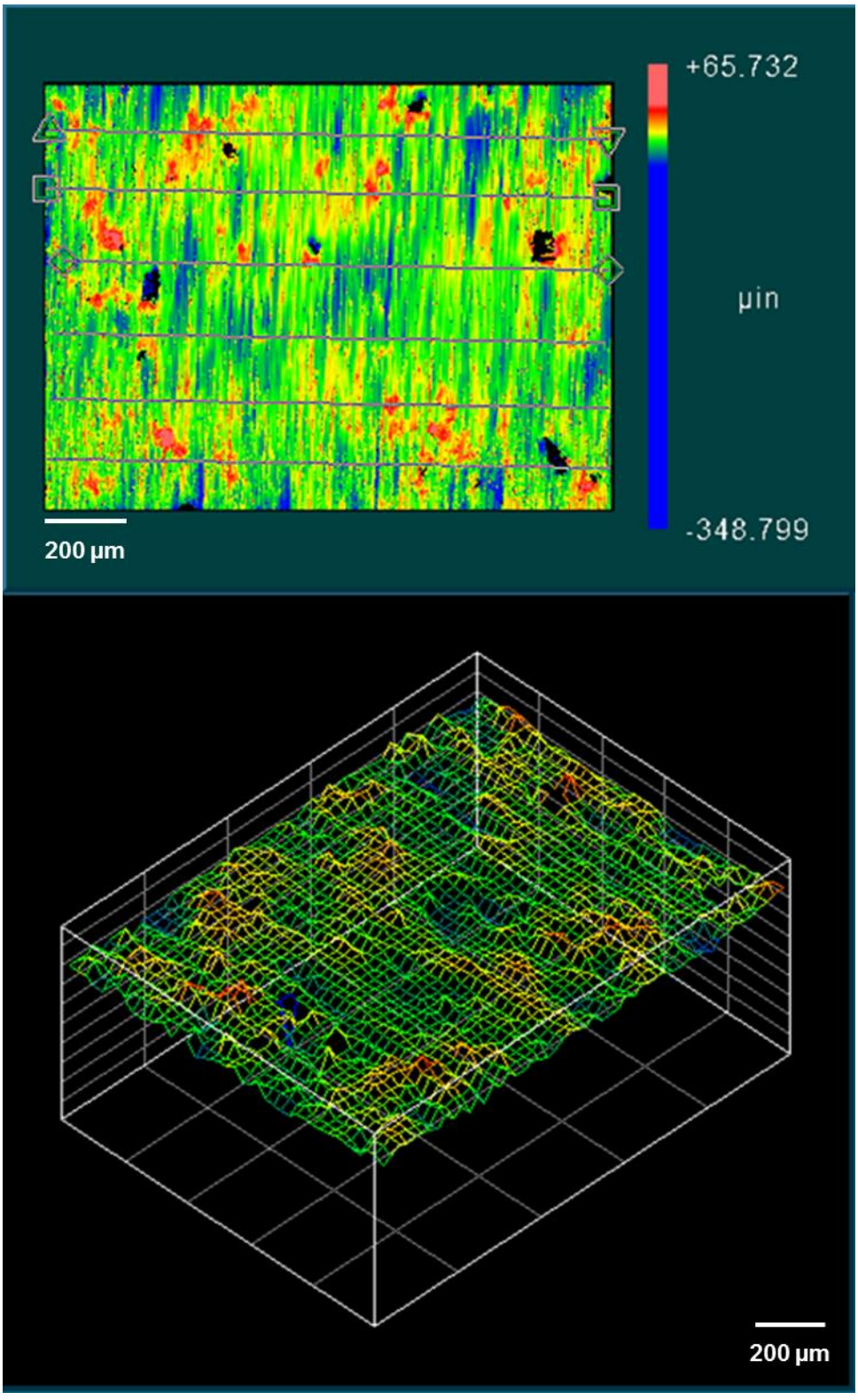

Figure 65 – Optical profilometry of the SS 431/20 TiC RCF test specimen, at the surface without defects.

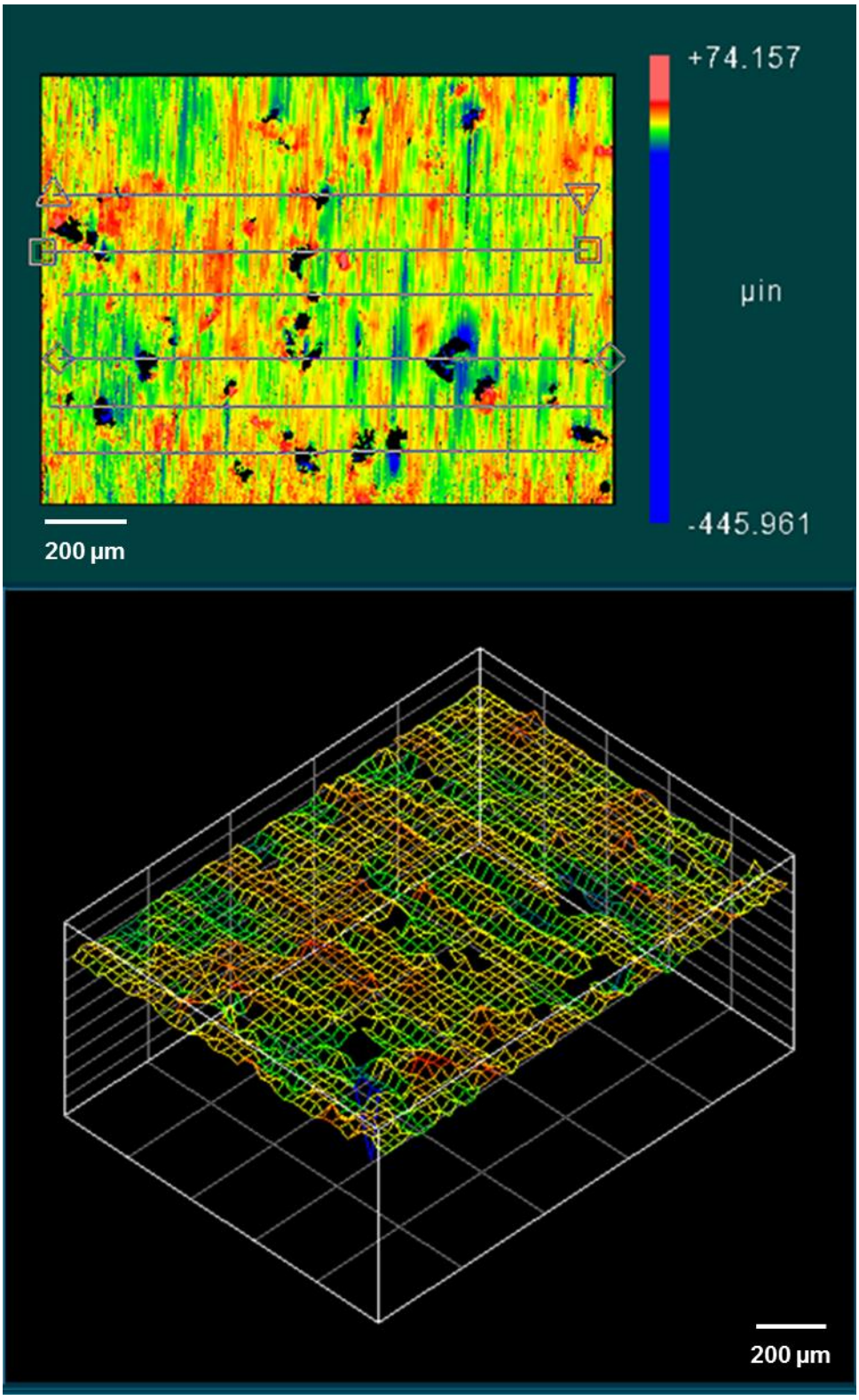

Figure 66 – Optical profilometry of the SS 431/20 TiC RCF test specimen, at the surface with defects.

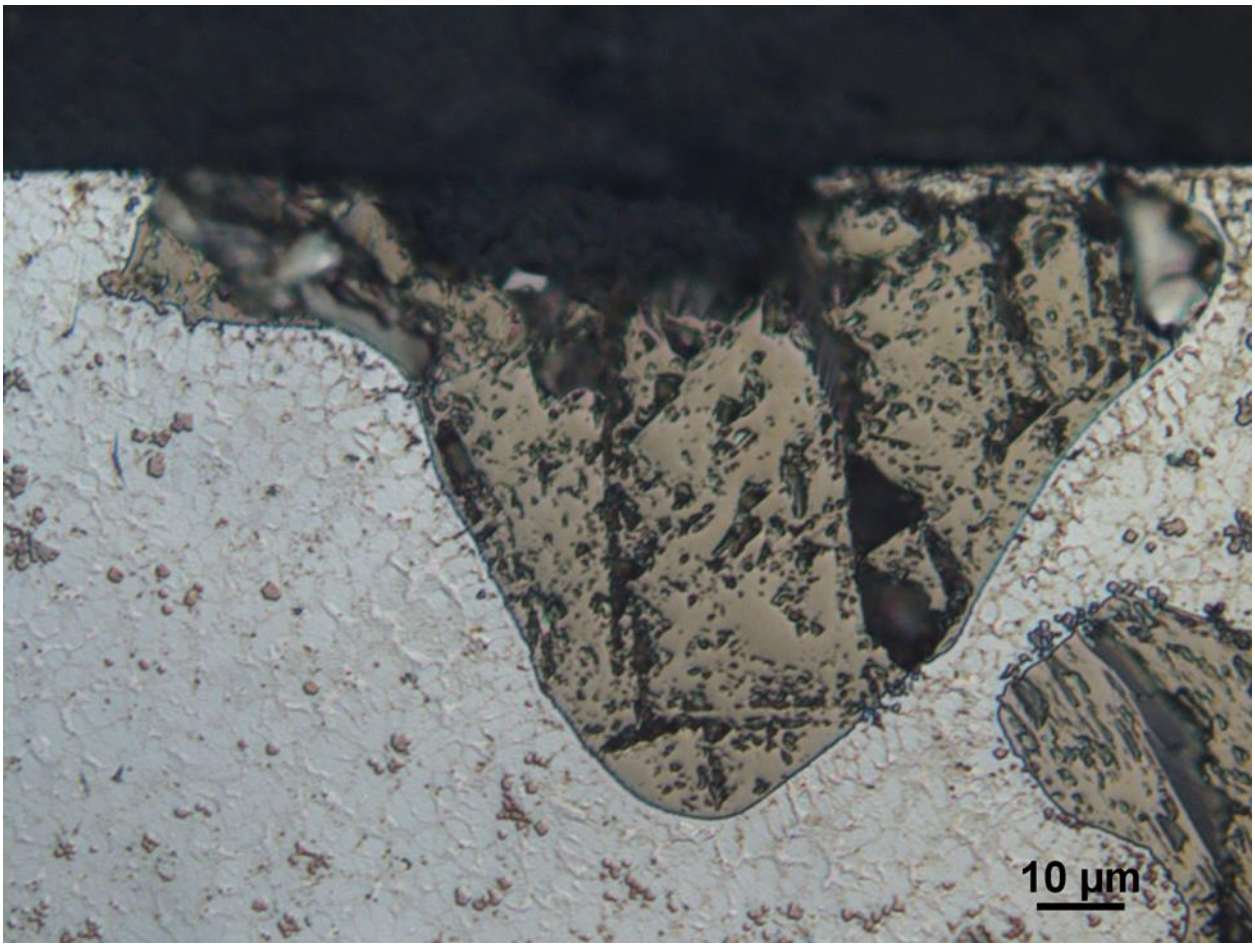

Figure 67 – Microstructural image showing the voids on the surface of RCF specimen.

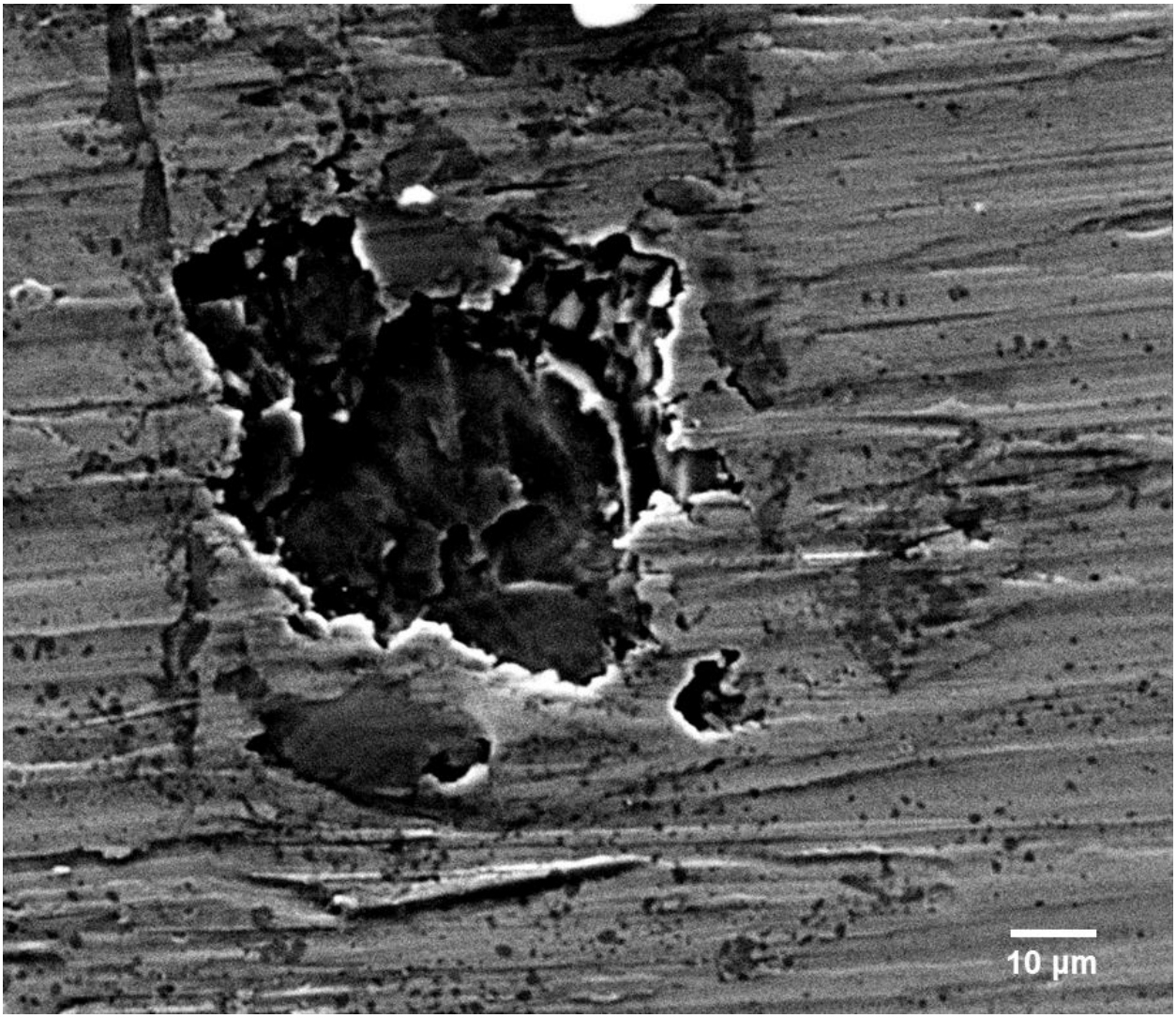

Figure 68 – SEM image shows the voids on the surface of RCF specimen.

Table 19 – Surface roughness of baseline material and laser deposited materials for power shaft.

	Baseline Inconel 718®	Inconel 718® on Inconel 718®	SS 431 on Inconel 718®	SS 431/20 TiC on Inconel 718®	SS 431/40 TiC on Inconel 718®
Avg. Ra (µm.)	0.833	0.889	1.46	1.12	0.843
Areal Ra (µm.)	0.965	0.912	1.46	1.12	0.841

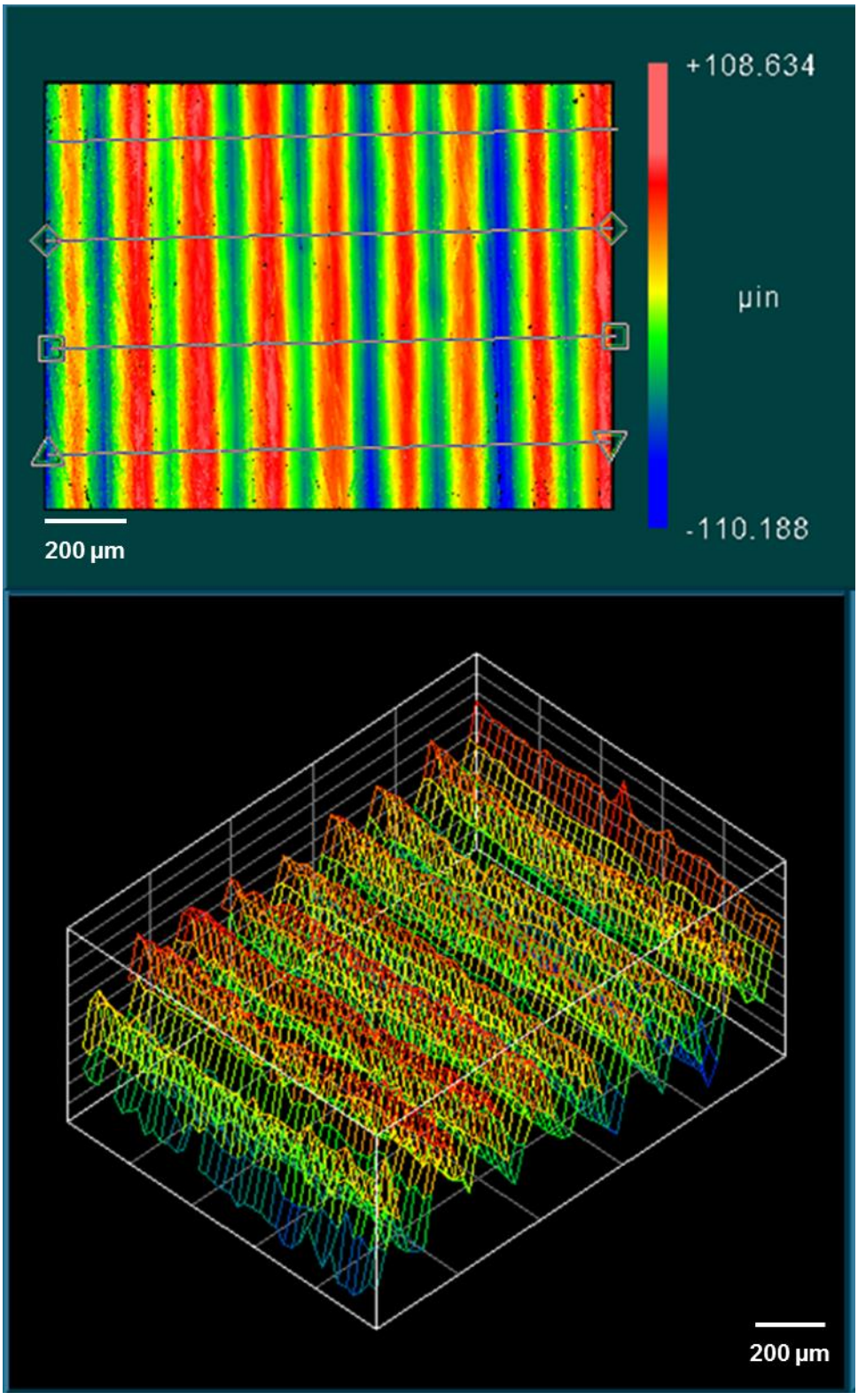

Figure 69 – Optical profilometry results of Inconel 718® shaft.

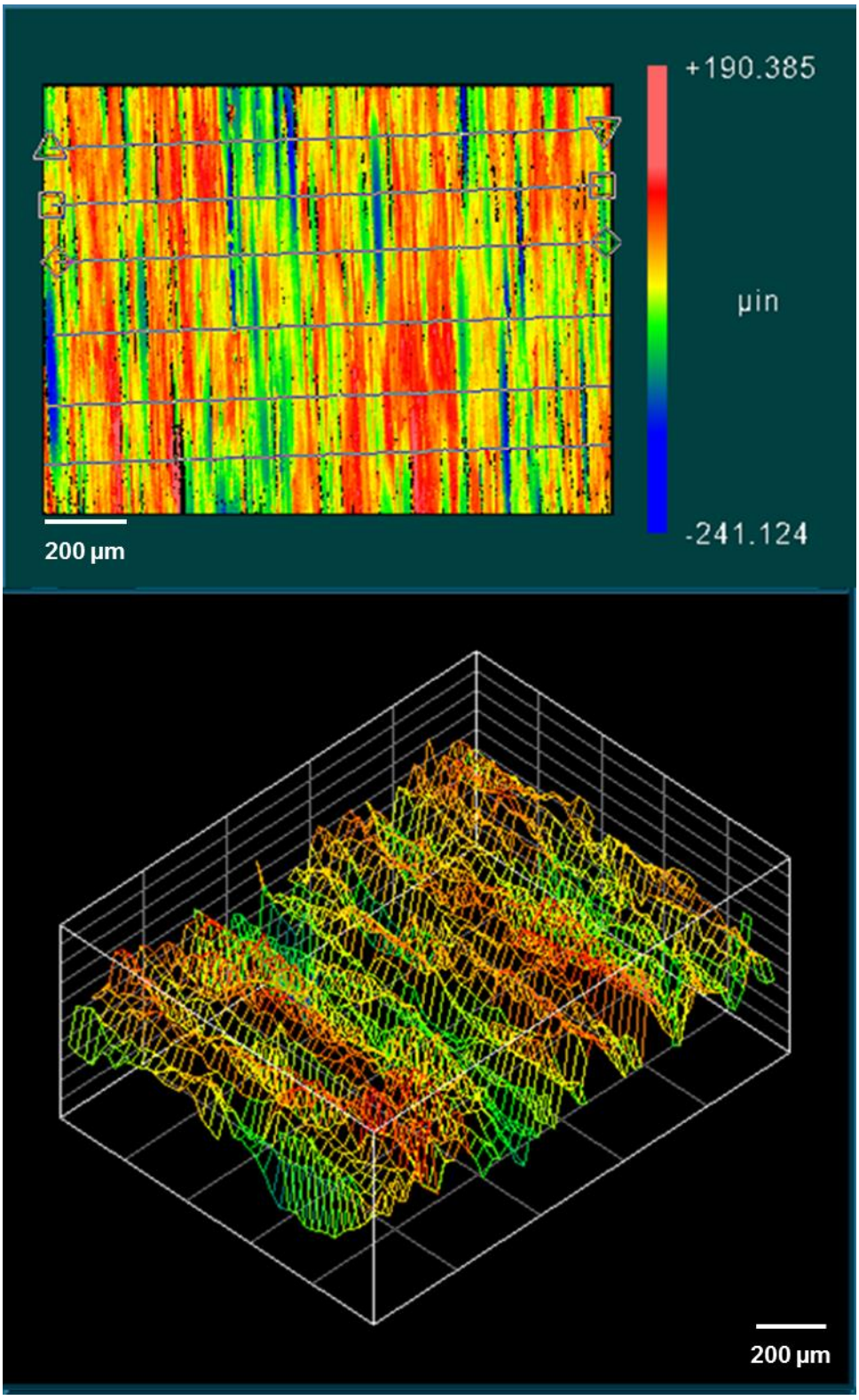

Figure 70 – Optical profilometry results of Inconel 718 deposited onto Inconel 718® shaft.

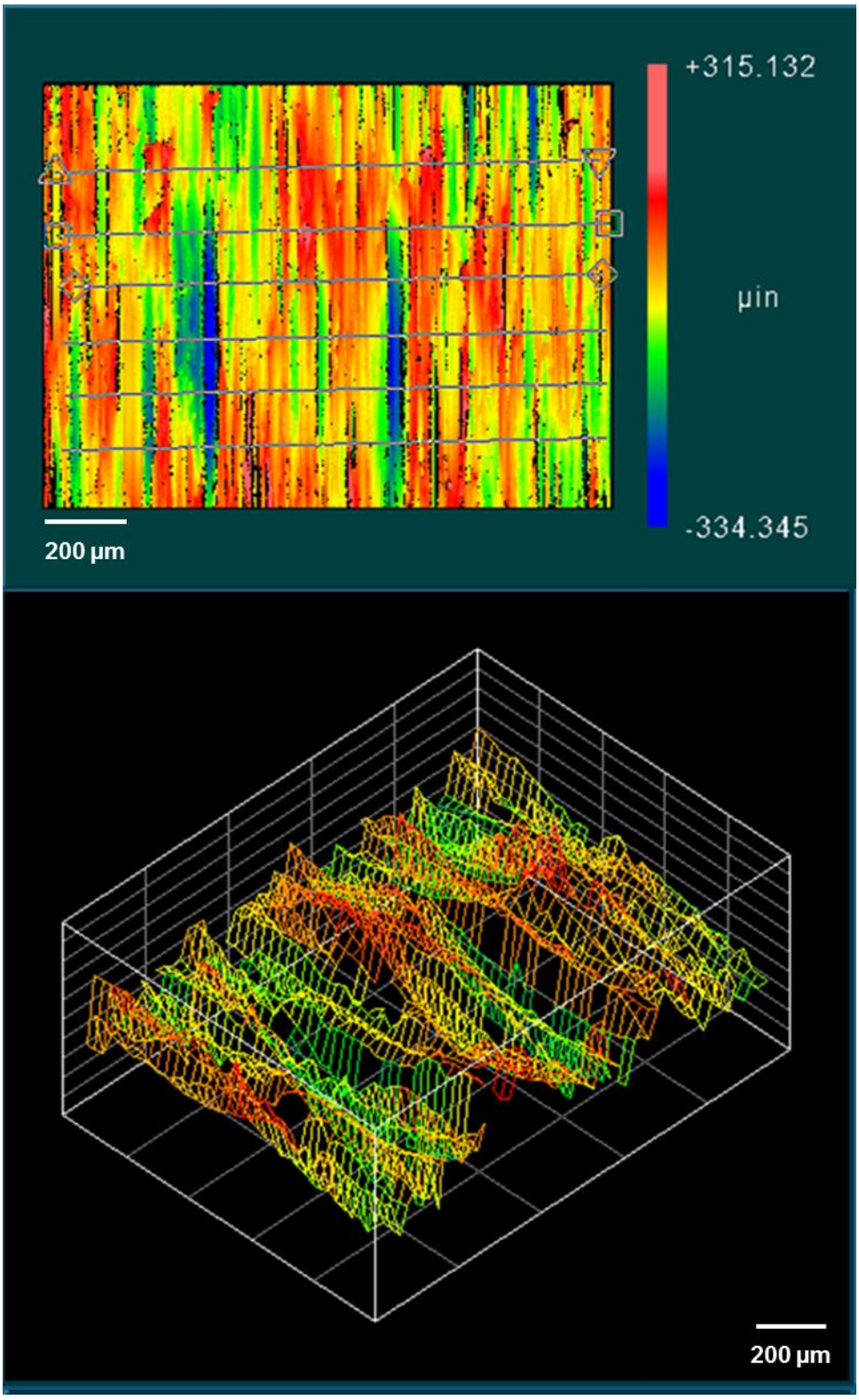

Figure 71 – Optical profilometry results of SS 431 deposited onto Inconel 718® shaft.

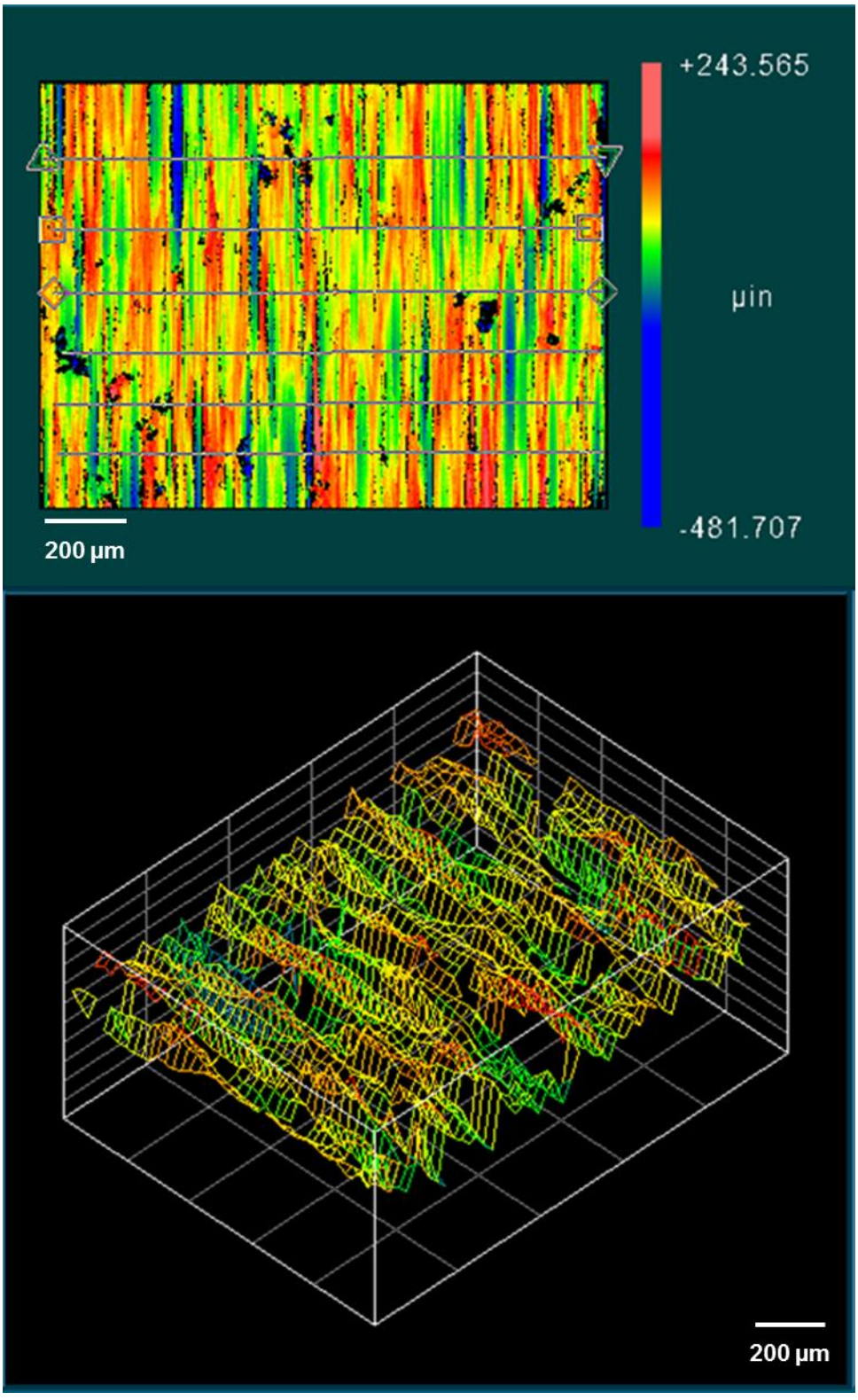

Figure 72 – Optical profilometry results of SS 431/20 TiC deposited onto Inconel 718® shaft.

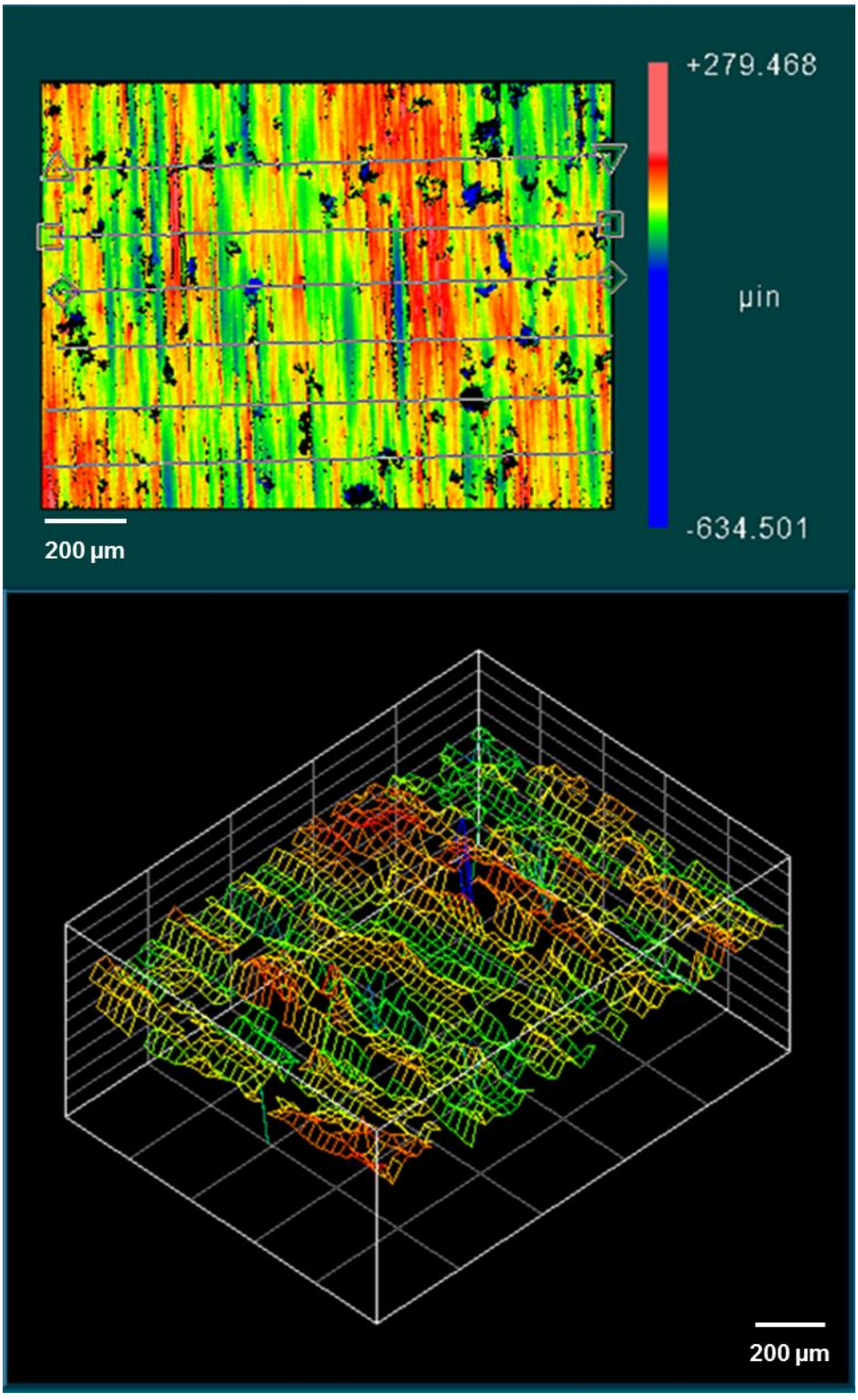

Figure 73 – Optical profilometry results of SS 431/40 TiC deposited onto Inconel 718® shaft.

Chapter 5. CONCLUSIONS

Laser deposition of a SS 431-TiC composite was successfully conducted as repair materials to deposit on a carburized surface on 8620 steel and chromium electroplating on Inconel 718®. Evaluations were conducted with deposition materials representing Inconel 718®, martensitic SS 431, and SS 431 with TiC to form a metal matrix composite system. All materials were used in powder form, and the evaluations included detailed characterization of the deposits produced from these materials on 8620 steel or Inconel 718®. The conclusions that may be drawn from this research are shown below.

- Microstructural analysis determined that the single layer deposition provided good deposition quality. However, multiple layer depositions with above 20 wt% of TiC concentration resulted in the generation of surface cracks. Microstructural analysis also indicated that the unmelted TiC particles tended to remain near the top of deposit surface due to buoyancy of the lower density of TiC particles when compared to the molten SS 431 melt pool.

- Micro hardness testing of the laser deposits indicated that the deposition material provided higher hardness with increased TiC content in the SS 431 matrix. Results also showed that multiple layer deposition had higher hardness than single layer deposition due to decrease substrate dilution in the upper layer.

- Micro hardness testing also indicated that the hardness of the SS 431/20 TiC deposited on the carburized 8620 steel matched the hardness of the carburized 8620 steel. Micro hardness of the deposited materials was found to be exhibit an area average Vickers hardness of 750 HV.

- Micro hardness testing also found the chromium electroplated surface exhibited an average Vickers hardness of 700 HV. None of the selected deposition materials deposited on the Inconel 718® matched the hardness of the chromium electroplated surface. The hardnesses measured for these specimens were: Inconel 718® deposit HV_{ave} = 300, SS 431 deposit HV_{ave} = 230, SS 431/20 TiC deposit HV_{ave} = 260, and SS 431/20 TiC deposit HV_{ave} = 350.

- Laser deposition of a SS 431-20 TiC powder blend was evaluated using the rolling contact fatigue test, and the results of these tests indicated that the laser deposit exhibited slightly greater wear than the carburized surface under the same conditions.
- Rolling contact fatigue testing of the composite SS 431/20 TiC deposit displayed significant surface scuffing. It is believed that this was due to the extremely high hardness of the unmelted TiC particles that were ejected from the surface of specimens, which began to wear the surface of the carburized steel roller.
- SEM images showed that some of the TiC particles dissolved and the Ti and C were reprecipitated in the SS 431 matrix. Chemical analysis by EDS further supported this conclusion.
- Surface roughness of specimens must have a Ra value less than 0.81 μm. Tribology analysis after roller grind machining indicated that surface roughness of the laser deposited SS 431/20 TiC composite can be achieved with Ra = 0.19 μm.
- Tribology analysis also found the laser deposited materials on the Inconel 718® shaft have higher Ra value than 0.81 μm: Inconel 718® deposit Ra = 0.89, SS 431 deposit Ra = 1.46, SS 431/20 TiC deposit Ra = 1.12, and SS 431/20 TiC deposit Ra = 0.84.

REFERENCES

[1] Z. Royer, R. P. Martukanitz. "Characterization of Specimens Representing Laser-Based Deposition of Inconel 718 on AISI 9310 Steel Substrate". A Thesis in Department of Material Science and Engineering at Pennsylvanian State University. (2011)

[2] I. Gibson, D. W. Rosen, B. Stucker, "Additive Manufacturing Technologies - Rapid Prototyping to Direct Digital Manufacturing", Springer Science + Business Media, LLC (2010)

[3] R. P. Martukanitz, and S. S. Babu, "Development of Advanced Wear and Corrosion Resistant Systems through Laser Surface Modification and Materials Simulation", Final Report on Research Conducted Through a Cooperative Agreement under Instrument Number DE-FC07-02ID14247, Department of Energy Report (2003)

[4] F. Lia, S. Kelly, R. P. Martukanitz. "Evaluation and Characterization of Materials and Processing Conditions for Establishing a Laser-Based Repair Process for Aerospace Gears". A Thesis in Department of Material Science and Engineering at Pennsylvanian State University. (2012)

[5] N. B. Dahotre, S. P. Harimkar, "Laser Fabrication and Machining of Materials", Springer Science + Business Media, LLC (2008)

[6] W. M. Steen, J. Mazumder, "Laser Material Processing 4th Edition", Springer-Verlag London Limited (2010)

[7] J.Y. Jeng, S.C. Peng, C.J. Chou, "Metal Rapid Prototype Fabrication Using Selective Laser Cladding Technology", Int J Adv Manuf Technol, vol. 16, p. 681–687 (2000)

[8] G.P. Dindaa, A.K. Dasgupta, J. Mazumder, "Laser aided direct metal deposition of Inconel 625 superalloy: Microstructural evolution and thermal stability", Materials Science and Engineering A, vol. 509, p. 98–104 (2009)

[9] C.P. Paula, P. Ganesha, S.K. Mishraa, P. Bhargavaa, J. Negib, A.K. Nath, "Investigating laser rapid manufacturing for Inconel-625 components", Optics & Laser Technology, vol. 39, p. 800–805 (2007)

[10] B. Zheng, T. Topping, J. E. Smugeresky, Y. Zhou, A. Biswas, D. Baker, E. J. Lavernia, "The Influence of Ni-Coated TiC on Laser-Deposited IN625 Metal Matrix Composites", Metallurgical and Materials Transactions A, 41(3), pp.568-573 (2010)

[11] F. H. Liu, Y. K. Shen, Y. S. Liao, "Selective laser gelation of ceramic–matrix composites", Composites: Part B 42 pp.57–61 (2011)

[12] V. K. Balla, S. Bose, and A. Bandyopadhyay, "Processing of Bulk Alumina Ceramics Using Laser Engineered Net Shaping", Int. J. Appl. Ceram. Technol., 5 [3] pp.234–242 (2008)

[13] Y. C. Hagedorn, J. Wilkes, W. Meiners, W. Konrada; R. Poprawe, "Net Shaped High Performance Oxide Ceramic Parts by Selective", Physics Procedia 5 pp.587–594 (2010)

[14] P. Bai , Y. Li, “Study on High Temperature Sintering Processes of Selective Laser Sintered Al_2O_3-ZrO_2-TiC Ceramics”, Science of Sintering, 41 pp.35-41 (2009)

[15] I. Shishkovsky, I. Yadroitsev, Ph. Bertrand, I. Smurov, “Alumina–Zirconium Ceramics Synthesis by Selective Laser Sintering/Melting”, Applied Surface Science 254 pp.966–970 (2007)

[16] A. Gahler, J. G. Heinrich, F. Schwertfeger, J. Gunster, “Three-Dimensional Laser Surface Sintering of SiO2 Green Bodies”, Int. J. Appl. Ceram. Technol., 3 [4] 331–335 (2006)

[17] W. Loschau, R. Lenk, S. Scharek, M. Teichgraber, S. Nowotny, C. Richter, “Prototyping of Complex-shaped Parts and Tools of Si/SiC-Ceramics by Selective Laser Sintering”, Industrial Ceramics v.20 n.2 pp.95-96 (2000)

[18] X. Tian, J. Günster, J. Melcher, D. Li, J. G. Heinrich, “Process parameters analysis of direct laser sintering and post treatment of porcelain components using Taguchi’s method”, Journal of the European Ceramic Society 29 pp.1903–1915 (2009)

[19] M. Hillert, “Phase Equilibria, Phase Diagrams and Phase Transformations – Their Thermodynamic Basis”, 2nd edition, Cambridge University Press (2008)

[20]”AISI 8620”, Alloy Digest, Engineering Alloys Digest, Inc. Upper Montclair, New Jersey, ASM International (2002)

[21] D. R. McPherson and S. B. Rao, “Mechanical Testing of Gears, Mechanical Testing and Evaluation”, Vol 8, ASM Handbook, ASM International (2000)

[22] D. R. McPherson, “The Effect of Lubricant Viscosity, Surface Roughness, and Rolling and Sliding Velocities on EHD Film Thickness and Pitting Fatigue”, Gear Research Institute at PSU-ARL (2002)

[23]”ASTM E384 – 11”, West Conshohocken, PA: ASM International (2012)

[24]”ASTM E140 – 12b”, West Conshohocken, PA: ASM International (2013)

[25] S. J. B. Reed, “Electron microprobe analysis and scanning electron microscopy in geology”, Cambridge University Press (2005)

[26] B. Hafner, “Energy Dispersive Spectroscopy on the SEM: A Primer”, Characterization Facility, University of Minnesota – Twin Cities

[27] D. Balasenthil, “ME-255: Principles of Tribology - Surface Properties - Measurement Techniques Profilometer”, Dept. of Mechanical Engineering, IISc

[28] M. Visscher, C. P. Hendriks, K. G. Struik, “Optical profilometry and its application to mechanically inaccessible surfaces Part II: Application to elastomer/glass contacts”, Precision Engineering, Vol 16 No 3 (1994)

[29]”ASM Handbook Volume 9 - Metallography and Microstructures”. Materials Park, Ohio: ASM International, p. 671 (2004).

[30] S. S. Kiparisov, V. K. Narva, S. Ya. Kolupaeva, “Dependence of the Properties of Titanium Carbide – Steel Materials Upon the Composition of the Titanium Carbide”, Moscow Institute of Steel and Alloys. Translated from Poroshkovaya Metallurgiya, No. 7 (151), pp.41-44, (1975)

[31] J. R. Davis, “Nickel, cobalt, and their alloys”, Materials Park, Ohio: ASM International, p. 33 (2000).

[32]”Allvac 718”, Alloy Digest, Engineering Alloys Digest, Inc. Upper Montclair, New Jersey, ASM International (2002)

[33]”Allvac 718-HS 718-DA”, Alloy Digest, Engineering Alloys Digest, Inc. Upper Montclair, New Jersey, ASM International (2006)

APPENDIX A – LASER DEPOSTION PROCESS PARAMETERS

	Laser Power (watts)	Travel Speed (IPM)	Powder Type	Powder Flow Rate (g/min)	Gas Type	Gas Flow Coaxial Rate (cfh)	Gas Flow Process Rate (cfh)	Gas Flow Trailing Rate (cfh)	Powder Nozzle Standoff (mm)	Spot Size (mm)	Comments
Material Selection	2000	25	431		Ar	20	20		10	4	1 rev on gullco, 2" DIA. PIPE
	2000	25	431/ 20% TiC		Ar	20	20		10	4	1 rev on gullco
	2000	25	431/ 40% TiC		Ar	20	20		10	4	1 rev on gullco
	2000	25	431		Ar	20	20	30	10	4	candy stripe,step over .075 "., 2nd layer over last .5 ", z up .035", cool down between layers, with trailing shield
	2000	25	431/ 20% TiC		Ar	20	20	30	10	4	candy stripe,step over .075 "., 2nd layer over last .5 ", z up .035", cool down between layers, with trailing shield
	2000	25	431/ 60% TiC		Ar	20	20	30	10	4	candy stripe,step over .075 "., 2nd layer over last .5 ", z up .035", cool down between layers, with trailing shield
	2000	25	431/ 40% TiC		Ar	20	20	30	10	4	candy stripe,step over .075 "., 2nd layer over last .5 ", z up .035", cool down between layers, with trailing shield
Process Development	1000	25	431/ 20% TiC		Ar	20	20	20	10	2.5	candy stripe, step .050", 1.35" length
	1000	25	431/ 40% TiC		Ar	20	20	20	10	2.5	candy stripe, step .050", 1.35" length
RCF Shaft-1	1000	25	431/ 20% TiC		Ar	20	20	20	10	2.5	candy stripe, step .050", 1.35" length
RCF Shaft-2	1000	25	431/ 20% TiC		Ar	20	20	20	10	2.5	candy stripe, step .050", 1.35" length
RCF Shaft-3	1000	25	431/ 20% TiC		Ar	20	20	20	10	2.5	candy stripe, step .050", 1.35" length
RCF Shaft-4	1000	25	431/ 20% TiC		Ar	20	20	20	10	2.5	candy stripe, step .050", 1.35" length

APPENDIX B – HARDNESS CONVERSION CHART

TABLE 1 Approximate Hardness Conversion Numbers for Non-Austenitic Steels (Rockwell C Hardness Range)[A, B]

Rockwell C Hardness Number 150 kgf (HRC)	Vickers Hardness Number (HV)	Brinell Hardness Number[C]		Knoop Hardness, Number 500-gf and Over (HK)	Rockwell Hardness Number		Rockwell Superficial Hardness Number			Scleroscope Hardness Number[D]	Rockwell C Hardness Number 150 kgf (HRC)
		10-mm Standard Ball, 3000-kgf (HBS)	10-mm Carbide Ball, 3000-kgf (HBW)		A Scale, 60-kgf (HRA)	D Scale, 100-kgf (HRD)	15-N Scale, 15-kgf (HR 15-N)	30-N Scale, 30-kgf (HR 30-N)	45-N Scale, 45-kgf (HR 45-N)		
68	940	...	...	920	85.6	76.9	93.2	84.4	75.4	97.3	68
67	900	...	...	895	85.0	76.1	92.9	83.6	74.2	95.0	67
66	865	...	...	870	84.5	75.4	92.5	82.8	73.3	92.7	66
65	832	...	(739)	846	83.9	74.5	92.2	81.9	72.0	90.6	65
64	800	...	(722)	822	83.4	73.8	91.8	81.1	71.0	88.5	64
63	772	...	(705)	799	82.8	73.0	91.4	80.1	69.9	86.5	63
62	746	...	(688)	776	82.3	72.2	91.1	79.3	68.8	84.5	62
61	720	...	(670)	754	81.8	71.5	90.7	78.4	67.7	82.6	61
60	697	...	(654)	732	81.2	70.7	90.2	77.5	66.6	80.8	60
59	674	...	634	710	80.7	69.9	89.8	76.6	65.5	79.0	59
58	653	...	615	690	80.1	69.2	89.3	75.7	64.3	77.3	58
57	633	...	595	670	79.6	68.5	88.9	74.8	63.2	75.6	57
56	613	...	577	650	79.0	67.7	88.3	73.9	62.0	74.0	56
55	595	...	560	630	78.5	66.9	87.9	73.0	60.9	72.4	55
54	577	...	543	612	78.0	66.1	87.4	72.0	59.8	70.9	54
53	560	...	525	594	77.4	65.4	86.9	71.2	58.6	69.4	53
52	544	(500)	512	576	76.8	64.6	86.4	70.2	57.4	67.9	52
51	528	(487)	496	558	76.3	63.8	85.9	69.4	56.1	66.5	51
50	513	(475)	481	542	75.9	63.1	85.5	68.5	55.0	65.1	50
49	498	(464)	469	526	75.2	62.1	85.0	67.6	53.8	63.7	49
48	484	451	455	510	74.7	61.4	84.5	66.7	52.5	62.4	48
47	471	442	443	495	74.1	60.8	83.9	65.8	51.4	61.1	47
46	458	432	432	480	73.6	60.0	83.5	64.8	50.3	59.8	46
45	446	421	421	466	73.1	59.2	83.0	64.0	49.0	58.5	45
44	434	409	409	452	72.5	58.5	82.5	63.1	47.8	57.3	44
43	423	400	400	438	72.0	57.7	82.0	62.2	46.7	56.1	43
42	412	390	390	426	71.5	56.9	81.5	61.3	45.5	54.9	42
41	402	381	381	414	70.9	56.2	80.9	60.4	44.3	53.7	41
40	392	371	371	402	70.4	55.4	80.4	59.5	43.1	52.6	40
39	382	362	362	391	69.9	54.6	79.9	58.6	41.9	51.5	39
38	372	353	353	380	69.4	53.8	79.4	57.7	40.8	50.4	38
37	363	344	344	370	68.9	53.1	78.8	56.8	39.6	49.3	37
36	354	336	336	360	68.4	52.3	78.3	55.9	38.4	48.2	36
35	345	327	327	351	67.9	51.5	77.7	55.0	37.2	47.1	35
34	336	319	319	342	67.4	50.8	77.2	54.2	36.1	46.1	34
33	327	311	311	334	66.8	50.0	76.6	53.3	34.9	45.1	33
32	318	301	301	326	66.3	49.2	76.1	52.1	33.7	44.1	32
31	310	294	294	318	65.8	48.4	75.6	51.3	32.5	43.1	31
30	302	286	286	311	65.3	47.7	75.0	50.4	31.3	42.2	30
29	294	279	279	304	64.8	47.0	74.5	49.5	30.1	41.3	29
28	286	271	271	297	64.3	46.1	73.9	48.6	28.9	40.4	28
27	279	264	264	290	63.8	45.2	73.3	47.7	27.8	39.5	27
26	272	258	258	284	63.3	44.6	72.8	46.8	26.7	38.7	26
25	266	253	253	278	62.8	43.8	72.2	45.9	25.5	37.8	25
24	260	247	247	272	62.4	43.1	71.6	45.0	24.3	37.0	24
23	254	243	243	266	62.0	42.1	71.0	44.0	23.1	36.3	23
22	248	237	237	261	61.5	41.6	70.5	43.2	22.0	35.5	22
21	243	231	231	256	61.0	40.9	69.9	42.3	20.7	34.8	21
20	238	226	226	251	60.5	40.1	69.4	41.5	19.6	34.2	20

[A] In the table headings, *force* refers to total test forces.
[B] Annex A1 contains equations converting determined hardness scale numbers to Rockwell C hardness numbers for non-austenitic steels. Refer to 1.12 before using conversion equations.
[C] The Brinell hardness numbers in parentheses are outside the range recommended for Brinell hardness testing in 8.1 of Test Method E10.
[D] These Scleroscope hardness conversions are based on Vickers—Scleroscope hardness relationships developed from Vickers hardness data provided by the National Bureau of Standards for 13 steel reference blocks, Scleroscope hardness values obtained on these blocks by the Shore Instrument and Mfg. Co., Inc., the Roll Manufacturers Institute, and members of this institute, and also on hardness conversions previously published by the American Society for Metals and the Roll Manufacturers Institute.

APPENDIX C – VICKERS HARDNESS RESULTS

Vickers Hardness for Material Selection

Materials	**SS 431**		**SS 431/20 TiC**		**SS 431/40 TiC**		**SS 431/60 TiC**	
Layer	Single	Multi	Single	Multi	Single	Multi	Single	Multi
Hardness Measurement (HV)	421	424	520	541	586	752	699	859
	401	438	545	530	608	697	832	755
	444	433	470	555	550	816	852	820
	413	454	514	461	626	789	862	741
	402	448	550	548	687	777	685	876
Average (HV)	416.2	439.4	519.8	527	611.4	766.2	786	810.2
Standard Deviation	15.74	10.65	28.50	34.02	45.51	40.27	77.48	54.12

Vickers Hardness for Process Development

Carburized 8620		.50 mm from top	.25 mm from top	.50 mm from top	.25 mm from top	Avg.	STDEV
	0.25		783		622	702.50	80.50
	0.5	633		535		584.00	49.00
	0.75		462		512	487.00	25.00
	1	420		491		455.50	35.50
	1.25		325		397	361.00	36.00
	1.5	278		412		345.00	67.00
	1.75		319		393	356.00	37.00
	2	326		369		347.50	21.50
431/20 TiC		.50 mm from top	.25 mm from top	.50 mm from top	.25 mm from top	Avg.	STDEV
	0.25		772		720	746.00	26.00
	0.5	733		763		748.00	15.00
	0.75		590		678	634.00	44.00
	1	405		372		388.50	16.50
	1.25		323		321	322.00	1.00
	1.5	295		298		296.50	1.50
	1.75		213		264	238.50	25.50
	2	285		312		298.50	13.50
431/40 TiC		.50 mm from top	.25 mm from top	.50 mm from top	.25 mm from top	Avg.	STDEV
	0.25		862		798	830.00	32.00
	0.5	826		504		665.00	161.00
	0.75		461		774	617.50	156.50
	1	316		369		342.50	26.50
	1.25		344		369	356.50	12.50
	1.5	325		326		325.50	0.50
	1.75		267		267	267.00	0
	2	299		297		298.00	1.00

Vickers Hardness for Transverse RCF Test Specimen

Transverse		.125 mm from top	.25 mm from top	.125 mm from top	.25 mm from top	.125 mm from top	.25 mm from top	.125 mm from top	.25 mm from top	Avg.	STDEV
	0.125	717		699		699		704		704.75	7.36
	0.25		639		692		661		720	678.00	30.70
	0.375	725		655		680		661		680.25	27.44
	0.5		655		694		655		657	665.25	16.62
	0.625	735		666		664		671		684.00	29.56
	0.75		697		356		351		322	431.50	153.84
	0.875	325		341		305		309		320.00	14.25
	1		303		318		306		285	303.00	11.81
	1.125	281		321		257		319		294.50	26.88
	1.25		310		285		262		310	291.75	19.98
	1.375	304		325		287		294		302.50	14.33
	1.5		278		288		301		272	284.75	10.99
	1.625	303		283		282		283		287.75	8.81
	1.75		270		288		277		269	276.00	7.58
	1.875	279		272		266		269		271.50	4.82
	2		271		307		274		278	282.50	14.36
	2.125	259		281		269		287		274.00	10.82
	2.25		312		320		313		324	317.25	4.97
	2.375	314		302		306		297		304.75	6.22
	2.5		358		341		317		325	335.25	15.72
	2.625	339		341		335		347		340.50	4.33

Vickers Hardness for Longitudinal RCF Test Specimen

Longitudinal		.125 mm from top	.25 mm from top	.125 mm from top	.25 mm from top	.125 mm from top	.25 mm from top	.125 mm from top	.25 mm from top	Avg.	STDEV
	0.125	594		633		680		650		639.25	31.08
	0.25		602		620		687		648	639.25	32.07
	0.375	616		614		661		631		630.50	18.79
	0.5		590		575		655		628	612.00	31.46
	0.625	581		561		462		641		561.25	64.42
	0.75		302		308		342		322	318.50	15.39
	0.875	293		311		296		325		306.25	12.79
	1		278		283		277		312	287.50	14.33
	1.125	293		293		268		318		293.00	17.68
	1.25		299		302		280		293	293.50	8.44
	1.375	283		293		292		282		287.50	5.02
	1.5		288		285		287		286	286.50	1.12
	1.625	272		263		275		275		271.25	4.92
	1.75		249		257		266		260	258.00	6.12
	1.875	263		252		275		263		263.25	8.14
	2		272		265		275		273	271.25	3.77
	2.125	295		290		305		301		297.75	5.72
	2.25		306		290		300		324	305.00	12.37
	2.375	312		312		320		322		316.50	4.56
	2.5		328		345		319		319	327.75	10.62
	2.625	313		304		323		328		317.00	9.25

Surface Hardness on SS 431/20 TiC RCF Specimen

	HRC	Vickers Hardness (HV)
Surface Hardness	60	697
	61	720
	59	674
Average	60	697
Standard Deviation	0.82	18.78

Vickers Hardness for Inconel 718® Shaft and Deposited Materials

Inconel 718 Base		.25 mm from top	.50 mm from top	.25 mm from top	.50 mm from top		Avg.	STDEV
	0.25	416		483			449.50	33.50
	0.5		457		430		443.50	13.50
	0.75	445		436			440.50	4.50
	1		432		449		440.50	8.50
	1.25	450		449			449.50	0.50
	1.5		440		423		431.50	8.50
	1.75	455		440			447.50	7.50
	2		434		438		436.00	2.00
Inconel 718		.25 mm from top	.50 mm from top	.25 mm from top	.50 mm from top		Avg.	STD
	0.25	308		341			324.50	16.50
	0.5		307		277		292.00	15.00
	0.75	304		292			298.00	6.00
	1		291		313		302.00	11.00
	1.25	301		293			297.00	4.00
	1.5		304		291		297.50	6.50
	1.75	270		278			274.00	4.00
	2		280		302		291.00	11.00
	2.25	261		250			255.50	5.50
	2.5		259		294		276.50	17.50
	2.75	276		267			271.50	4.50
	3		289		290		289.50	0.50
	3.25	274		282			278.00	4.00
SS 431		.25 mm from top	.50 mm from top	.25 mm from top	.50 mm from top		Avg.	STD
	0.25	254		239			246.50	7.50
	0.5		230		226		228.00	2.00
	0.75	224		225			224.50	0.50
	1		219		232		225.50	6.50
	1.25	241		280			260.50	19.50
	1.5		276		263		269.50	6.50
	1.75	287		266			276.50	10.50
	2		287		283		285.00	2.00
	2.25	267		262			264.50	2.50
	2.5		266		281		273.50	7.50
	2.75	270		274			272.00	2.00
	3		251		270		260.50	9.50
	3.25	242		214			228.00	14.00
431/20 TiC		.25 mm from top	.50 mm from top	.25 mm from top	.50 mm from top		Avg.	STD
	0.25	238		257			247.50	9.50
	0.5		257		317		287.00	30.00
	0.75	236		242			239.00	3.00
	1		234		277		255.50	21.50
	1.25	245		258			251.50	6.50
	1.5		243		248		245.50	2.50
	1.75	259		254			256.50	2.50
	2		243		257		250.00	7.00
	2.25	274		249			261.50	12.50
	2.5		269		266		267.50	1.50
	2.75	277		283			280.00	3.00
	3		299		291		295.00	4.00
	3.25	336		295			315.50	20.50
431/40 TiC		.25 mm from top	.50 mm from top	.25 mm from top	.50 mm from top		Avg.	STD
	0.25	374		324			349.00	25.00
	0.5		368		352		360.00	8.00
	0.75	325		348			336.50	11.50
	1		336		331		333.50	2.50
	1.25	302		270			286.00	16.00
	1.5		254		286		270.00	16.00
	1.75	282		273			277.50	4.50
	2		287		304		295.50	8.50
	2.25	298		311			304.50	6.50
	2.5		296		307		301.50	5.50
	2.75	317		320			318.50	1.50
	3		325		317		321.00	4.00

Vickers Hardness for Chrome Electroplated Surface on Inconel 718® Shaft

Chrome Electroplated	Vickers Hardness (HV)
	692
	690
	725
	746
	702
Average	711
Standard Deviation	21.47

APPENDIX D – OPTICAL PROFILOMETRY DATA

Carburized 8620 Steel

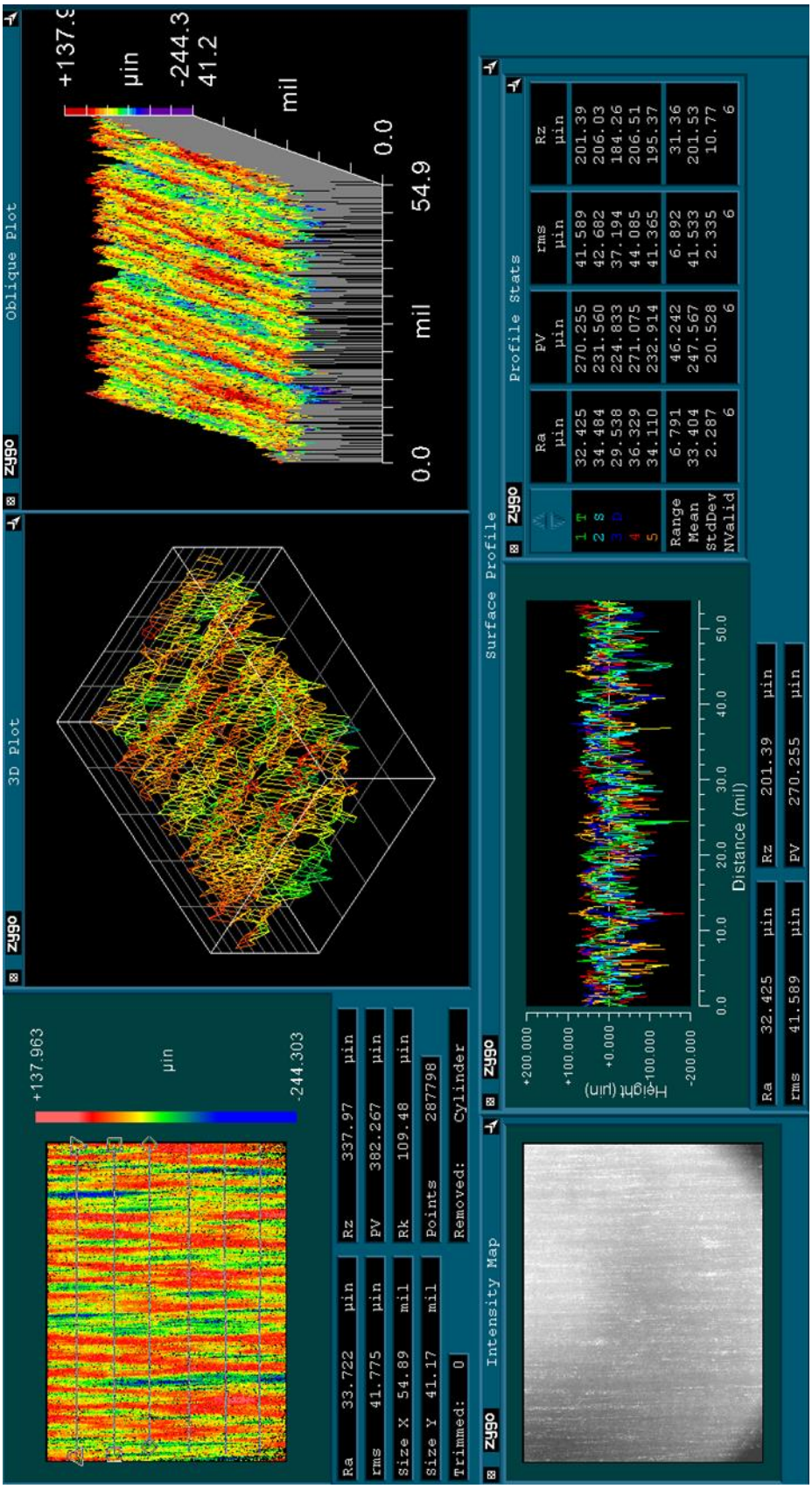

SS 431/20 TiC Laser Deposited on Carburized 8620 Steel

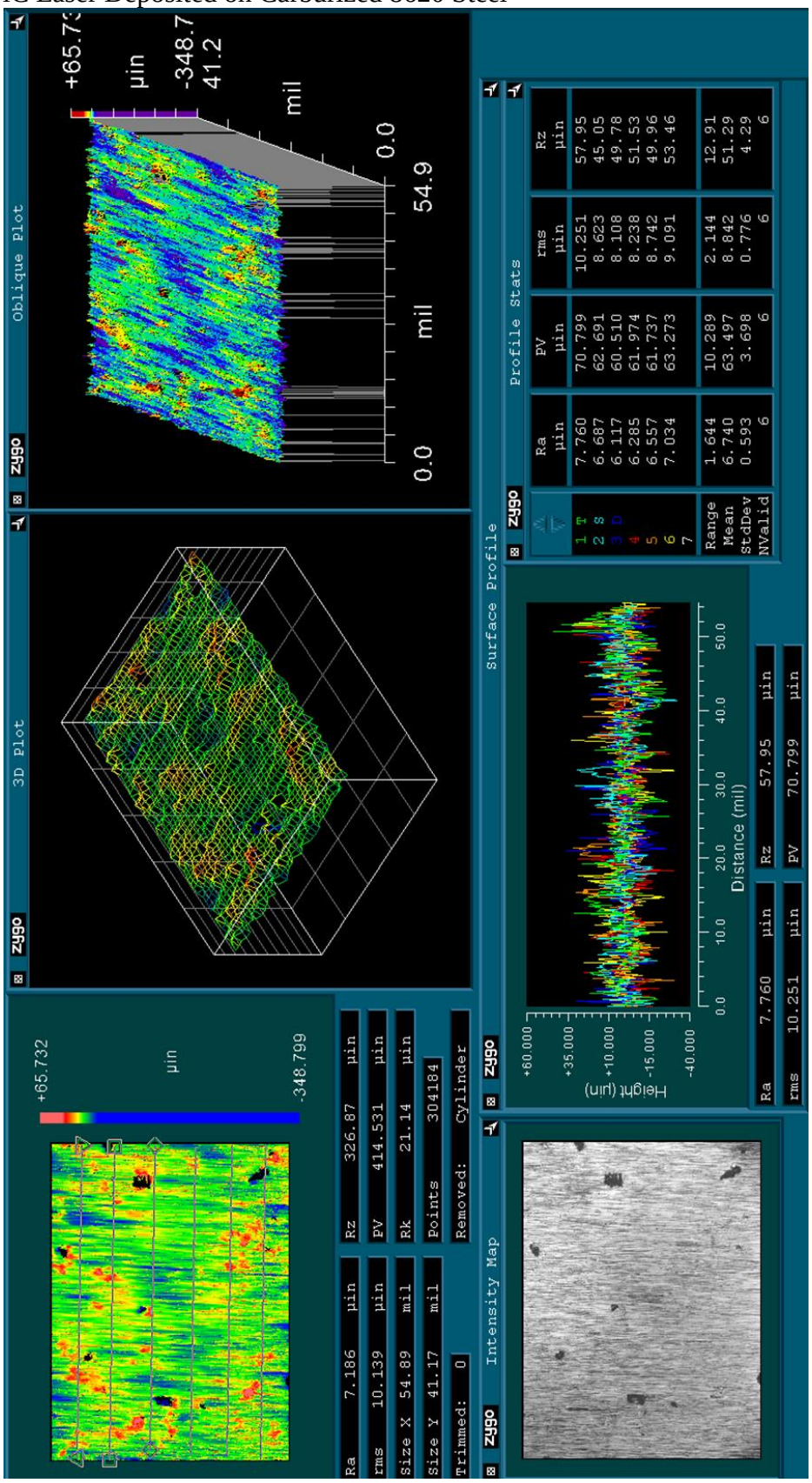

SS 431/20 TiC Laser Deposited on Carburized 8620 Steel, Pores

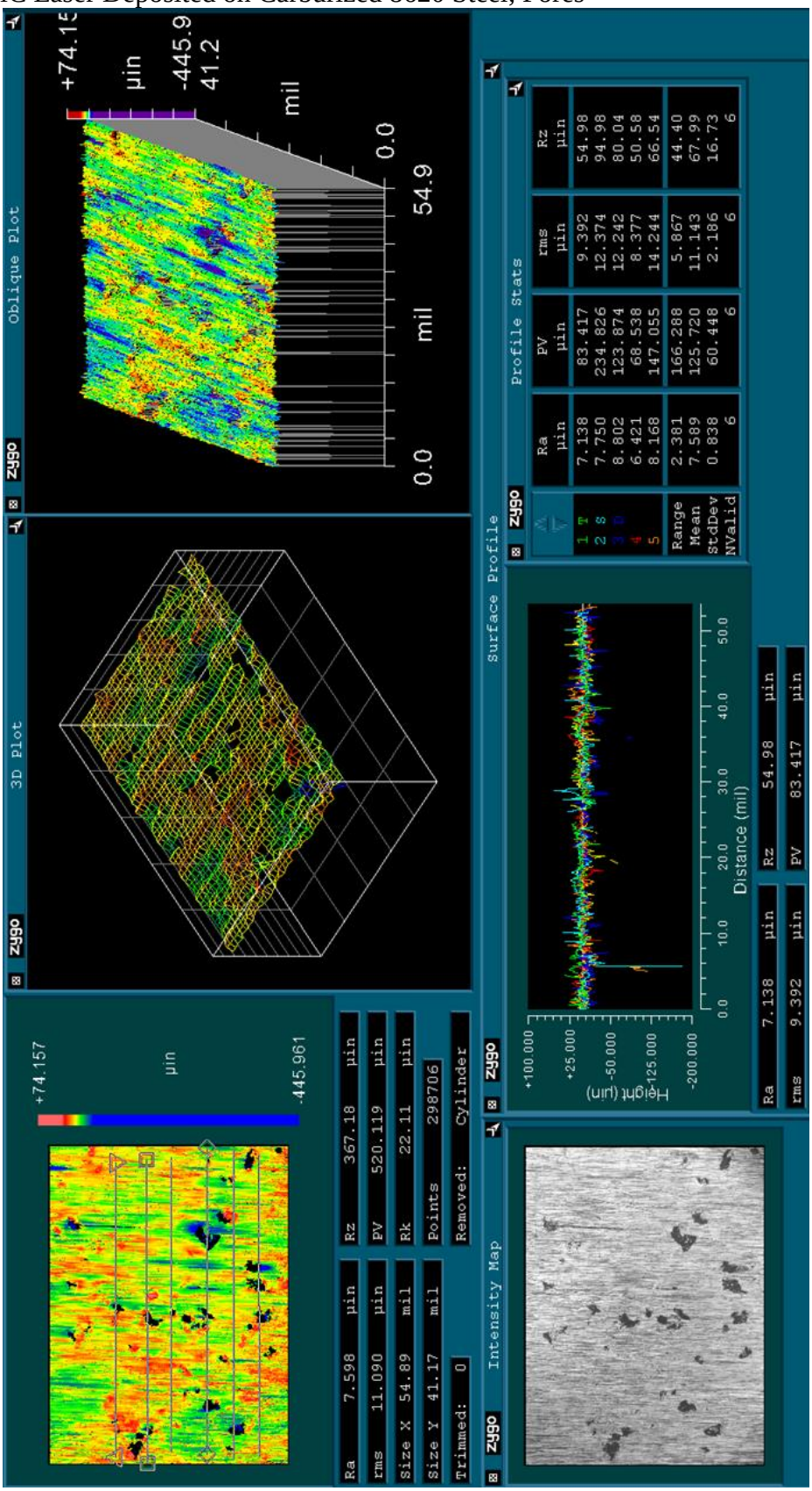

Inconel 718® Shaft

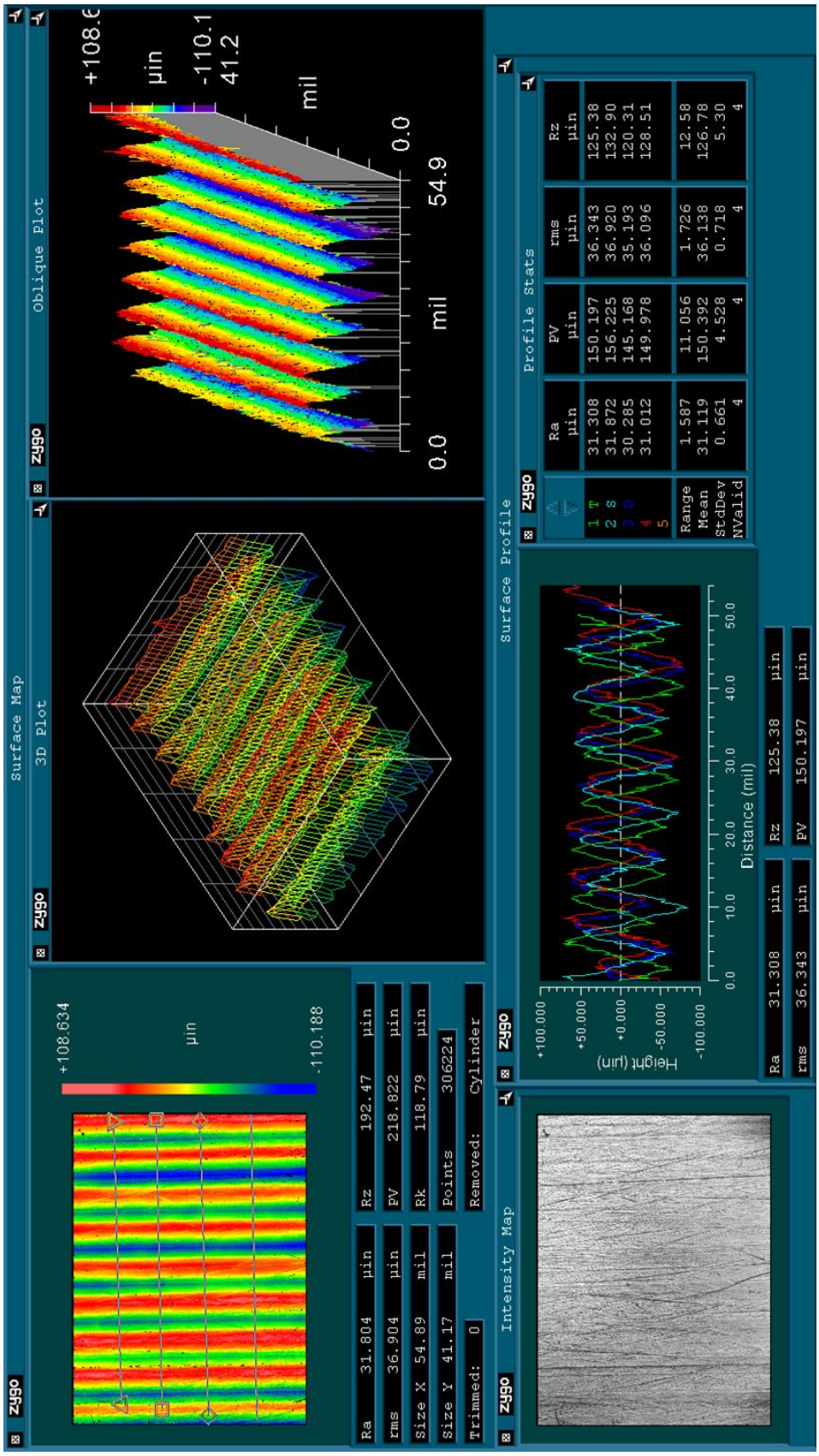

Inconel 718 laser Deposited on Inconel 718® Shaft

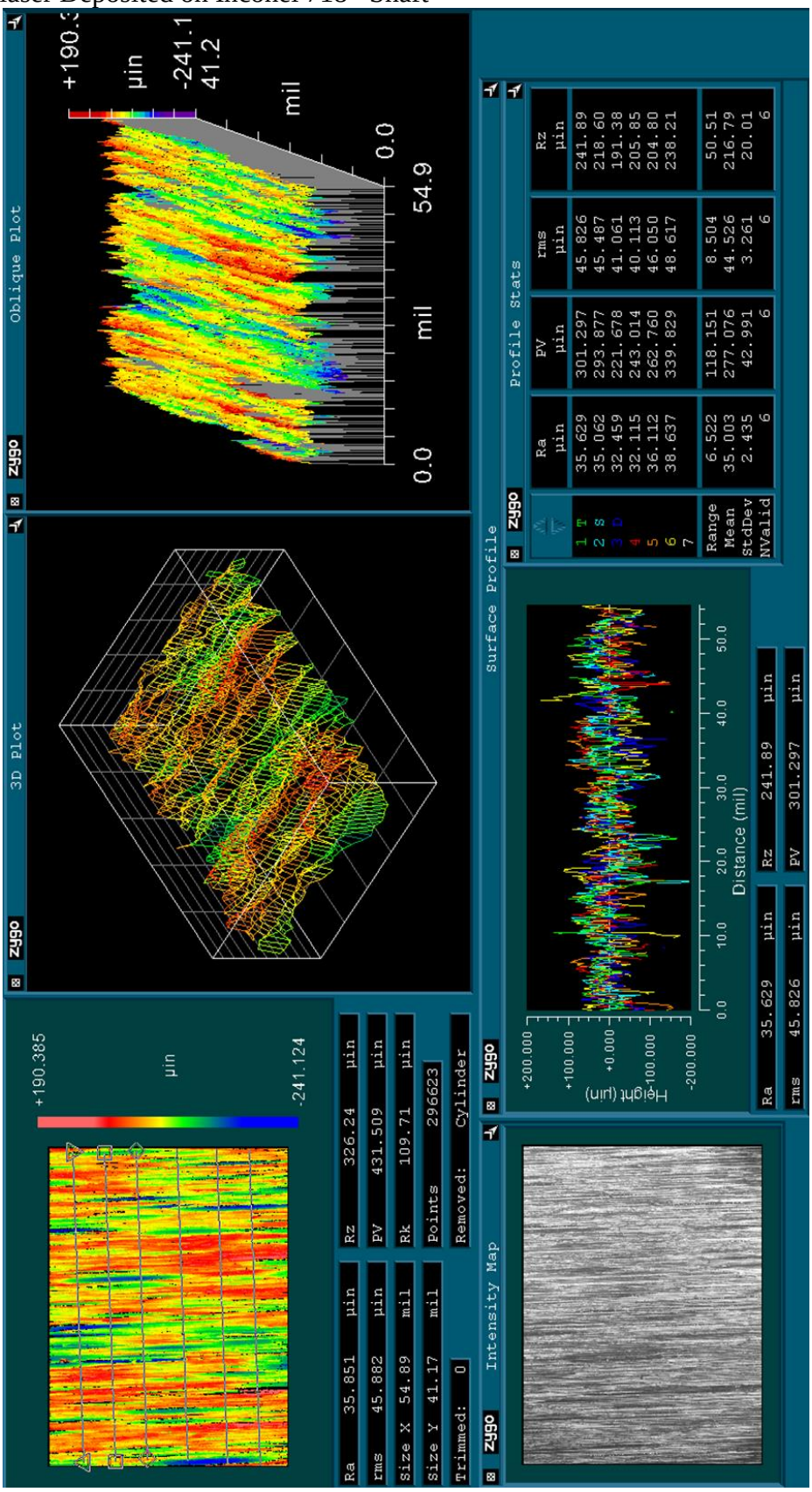

SS 431 laser Deposited on Inconel 718® Shaft

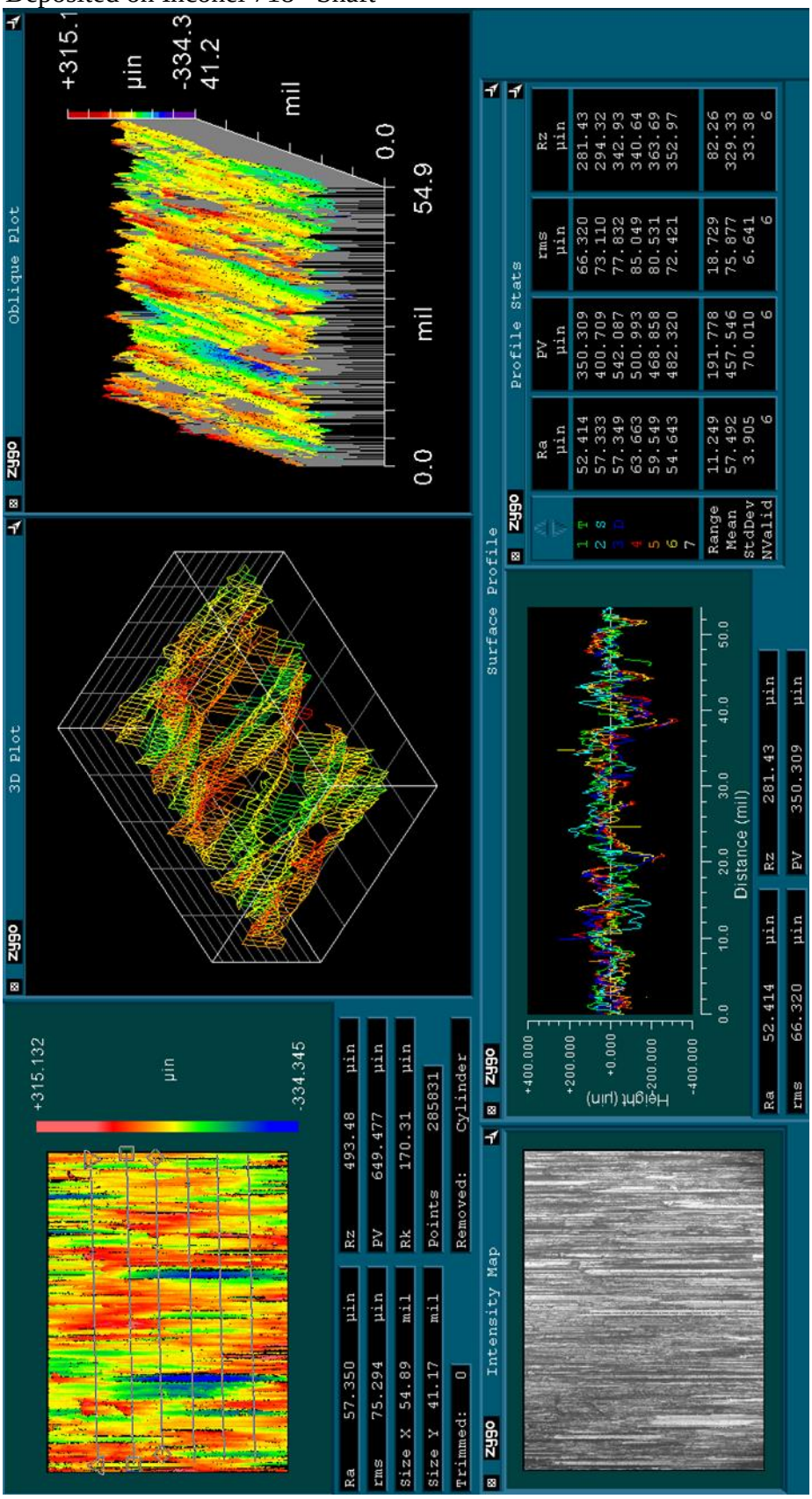

SS 431/20 TiC laser Deposited on Inconel 718® Shaft

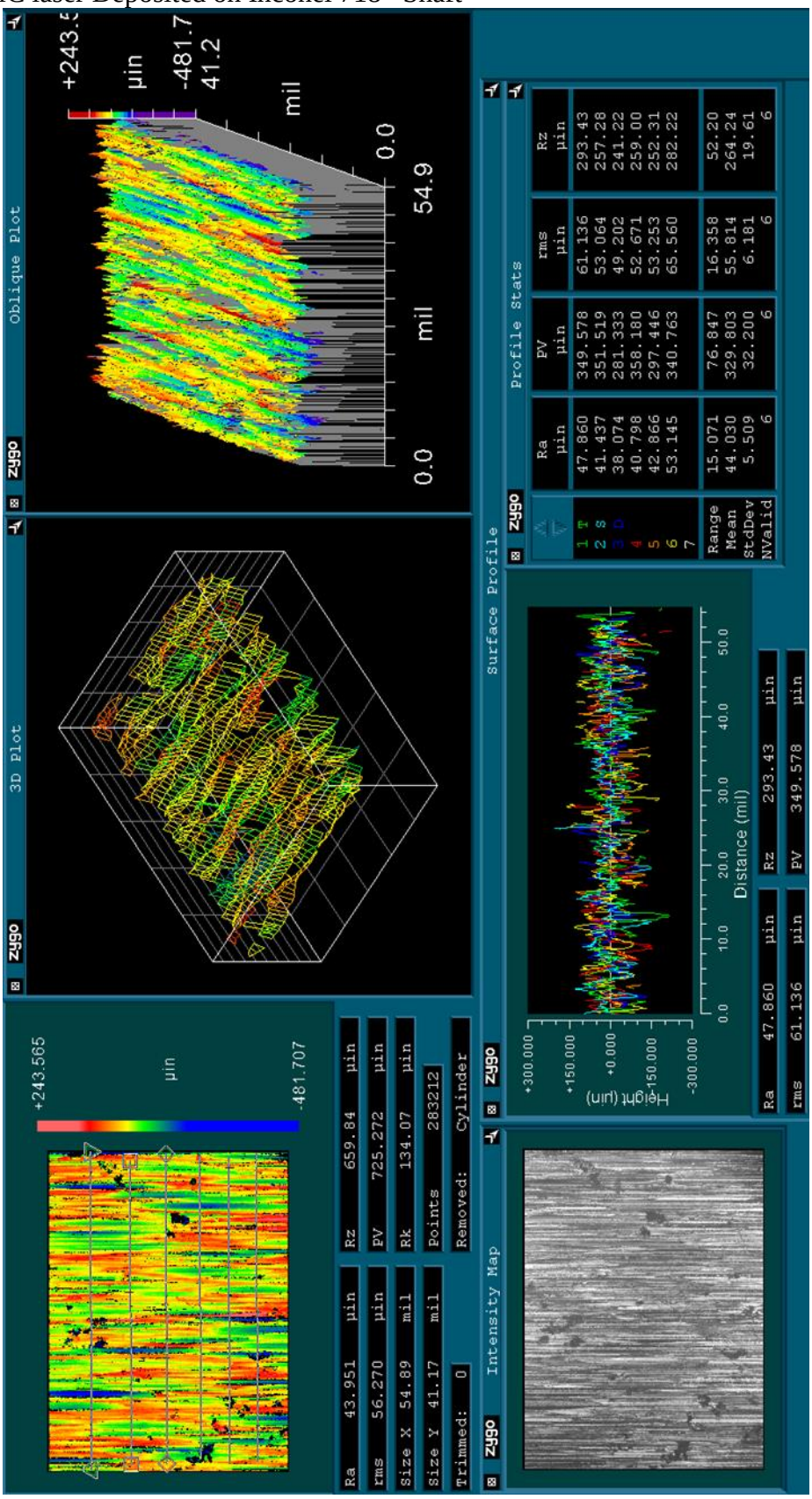
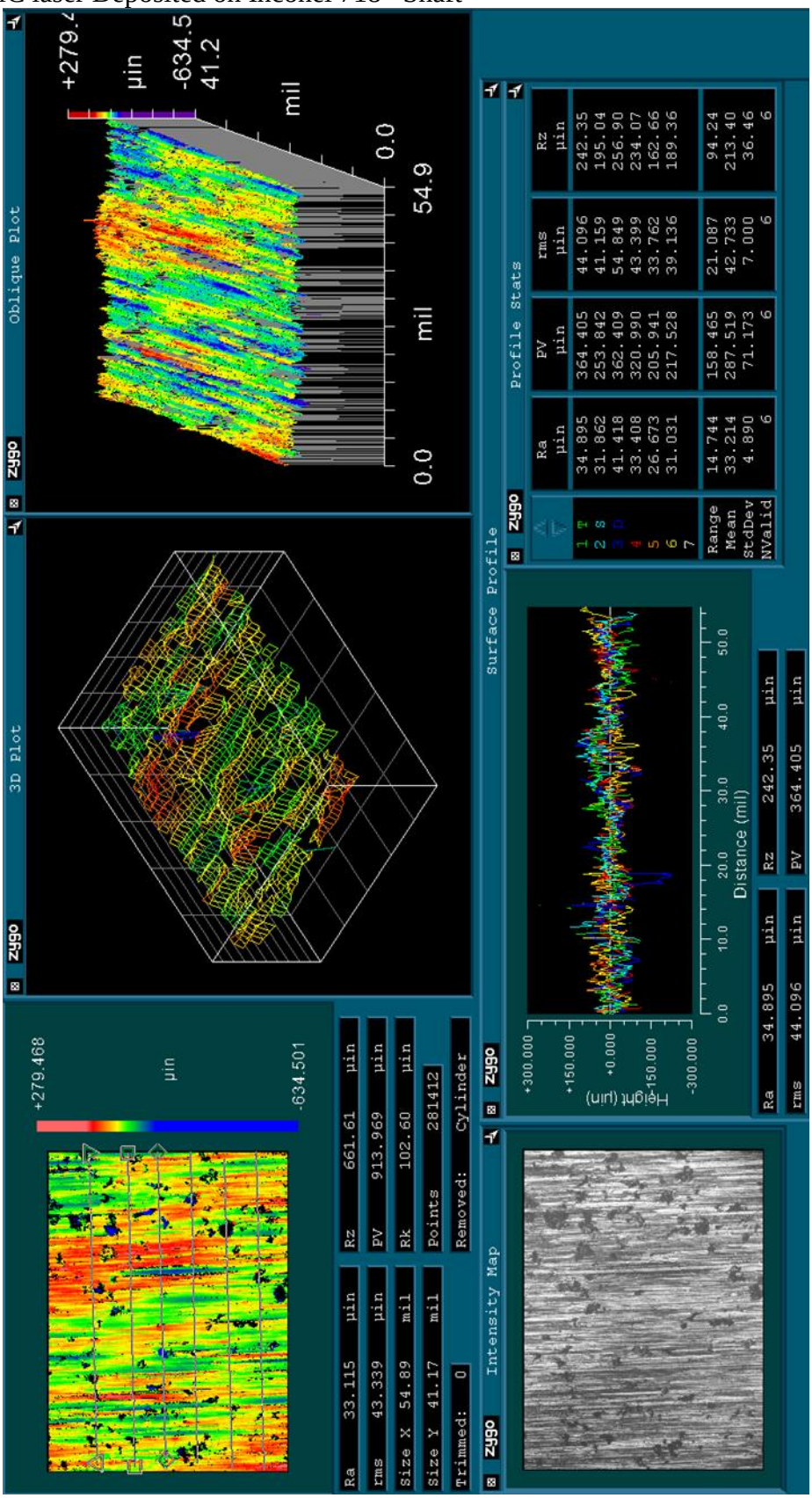
SS 431/40 TiC laser Deposited on Inconel 718® Shaft